

**Flexible Silicon Photonic Integrated Circuits for Optical Interconnects
and WDM Networks**

by

Yang Ren

A thesis submitted in partial fulfillment of the requirements for the degree of

Doctor of Philosophy

in

Photonics and Plasmas

Department of Electrical and Computer Engineering
University of Alberta

© Yang Ren, 2020

Abstract

In response to the continuous growth in the demand for higher speed and volume of data transmission, optical networks are evolving to become more elastic to maximize spectrum utility. This in turn is driving the development of flexible optical devices and circuits that can be reconfigured to adapt to fast changes in network conditions. Over the past decade, silicon photonics has gained widespread industry acceptance as a platform for photonic integrated circuits for optical communication, due to its low cost, potential for dense integration and compatibility with the CMOS fabrication process. In spite of its promising benefits, several important challenges remain in the development of flexible silicon photonic circuits, namely, broadband wavelength tunability, fast reconfigurability, and scalability.

This thesis addresses these issues through the development of flexible and scalable silicon photonic components for elastic optical networks, including a widely tunable reconfigurable optical add-drop multiplexing (ROADM) circuit, a universal variable bandwidth optical filter, and a fast wavelength selection circuit. The ROADM circuit can provide wavelength reconfigurability over more than 4 Tb/s data transmission bandwidth. The variable bandwidth filter is based on a novel microring-loaded Mach-Zehnder interferometer that can provide insertion loss-free bandwidth tuning by only tuning the microring resonant frequencies. The wavelength selection circuit combines the wide band tunability of thermo-optic microring filters with fast switching by free carrier injection to achieve best-case wavelength selection time of a few nanoseconds over a 32 nm wavelength range.

As silicon photonic circuits grow in functionality and complexity, it also becomes

necessary to monitor their performance and optical signal quality throughout the system. To address this issue, we proposed and investigated two novel methods for on-chip optical monitoring. The first method is the use of on-chip thermistors for tracking the center wavelength and bandwidth of microring add/drop filters. The second method is the use of silicon photodetectors based on two-photon absorption for on-chip signal detection. These devices and methods can be seamlessly integrated into silicon photonic circuits for real-time monitoring of their performance.

Acknowledgements

I would like to express the sincere gratitude to my mentor Prof. Vien Van. Without his patient guidance and day-and-night revision, I would not have seen the light of day on any of my research papers. Looking back my research life over the past five years, being able to join in this Nano Photonics Research Lab (NPRL) would be one of the most fortunate thing that I have ever experienced. I am very grateful for the chance that Prof. Vien Van gave me to be his student, all his knowledge and inspiration will benefit me for the rest of my life.

I am grateful to Guangcan Mi in particular, for all her constructive advice, and countless valuable discussion and argument.

My would like to give thanks to staff in CMC microsystems, for all their technical supporting throughout my graduate studies. In particular, many thanks to Susan Xu, none of the fabrication runs would have been possible without her technical support and careful inspection to my mask layouts.

I thank my colleagues: Huynh Ngo, Shirin Afzal, Hanfa Song, Christopher Soong, Tyler James Zimmerling, and Timothy Lee for their help, friendship, and all fun we have had.

I deeply thank my fiancée. She made me strong, as whenever I need support, she needs more support from me.

Finally, I sincerely thank my parents. Without their love and quiet encouragement, I won't come to Canada to spend the most significant decade of my life, with all these wonderful people.

Table of Contents

1	Introduction	1
1.1	State of the Art in Optical Interconnection Technology	1
1.2	Wavelength Division Multiplexing Technology in Optical Interconnection	3
1.3	Research Objectives	7
1.4	Organization of the Thesis	8
2	Microring Resonator Circuit Architectures for Flexible WDM Systems	9
2.1	Microring Resonator: Device Structure and Model	9
2.2	High-Order Microring Filter Architectures	14
2.2.1	Serially-Coupled Microring Filters	14
2.2.2	Cascaded MR Filters	17
2.3	Wavelength Tuning and Reconfigurability	19
2.3.1	Thermal-Optic Tuning	19
2.3.2	Free Carrier Dispersion	21
2.4	Summary	22
3	Broadband Tunable Multiplexer/Demultiplexer with Precise Temperature Tracking	24
3.1	Design and Performance of A Double-Microring Filter	26
3.1.1	DMR Filter Design and Fabrication	26
3.1.2	Thermal Analysis of DMR Filter	28

3.1.3	Tuning Performance of the DMR Filter	31
3.1.4	Performance of Thermistors for Temperature Tracking	37
3.2	A Vernier Cascaded Microring Filter	40
3.2.1	Design and Implementation of VCMR Filter	40
3.2.2	Calibration and Tuning of DMR Filter Stages	42
3.2.3	Performance of VCMR filter	44
3.3	Summary	47
4	Fast Wavelength Selector for High-Speed Optical Networks	49
4.1	Fast Wavelength Selector Circuit Architecture	51
4.2	Performance of 4 th -order DC-VMR Filter	56
4.3	Performance of <i>pin</i> MZS	59
4.4	Performance of WS Circuit	63
4.5	Summary	68
5	Variable Bandwidth Tunable Filters for Elastic Optical Networks	69
5.1	Ideal Pole and Zero Movements of a Bandwidth Tunable Filter	72
5.2	The MZI-MRR Bandwidth Tunable Filter Architecture	73
5.2.1	Insertion Loss-Free Bandwidth Tuning Range in MZI-MRR Filters	76
5.2.2	Bandwidth Tuning Performance of a 4 th -order MZI-MRR Filter	79
5.3	Demonstration of a 4 th -Order MZI-MRR VBW Filter	83
5.3.1	Design and Implementation of the MZI-MRR Filter	83
5.3.2	Performance of the MZI-MRR Filter	86
5.4	Summary	90
6	Enhanced Responsivity in All-Silicon Photodetection for Optical Monitoring	91
6.1	Silicon Microring <i>pin</i> Photodetectors	93

6.1.1	Response of <i>pin</i> MR PD to Single-Wavelength Input	94
6.1.2	Response of <i>pin</i> MR PD to Two-Wavelength Inputs	106
6.2	Silicon Microring p^+pn^+ Avalanche Photodetectors	110
6.2.1	Design of Silicon Microring Avalanche Photodetector	111
6.2.2	Responsivity of the MR APD	113
6.2.3	Bistability Behaviour of p^+pn^+ MR APD	118
6.3	Summary	121
7	Conclusion and Future Research Directions	123
7.1	Summary of Research Contributions	123
7.2	Recommendation for Future Research	126
7.2.1	Fast WS Circuit	126
7.2.2	MDM-WDM Hybrid Systems	128
	Appendix A: Appendix	142

List of Tables

6.1	Extracted nonlinear model parameters of MR PD. (*) C_α and η_α for -15 V bias voltages are valid for input power greater than 1 mW. . .	98
6.2	Extracted nonlinear model parameters of MR APD. (*) C_α and η_α are not valid for -15 V bias voltage.	116

List of Figures

1.1	A road map of optical interconnection technology, reproduced from [2]	2
1.2	Examples of silicon photonic devices for signal processing and optical interconnect applications. (a) and (b): chip-fibre coupling with grating-coupling and butt-coupling configurations, reproduced from [7]; (c) and (d): a high baud all-silicon photonic modulator, reproduced from [8]; (e): a broadband silicon thermal-optic 2×2 switch for optical mode switching, reproduced from [11]; (f): a broadband silicon polarization beam splitter, reproduced from [16]; (g) a thermally tunable silicon photonic filter based on microring (MR) waveguide, reproduced from [13]; (h): a 40 Gb/s all-silicon photodetector, reproduced from [14].	4
1.3	Schematic diagram of a WDM system.	5
2.1	Schematics of (a) an APMR configuration with radius R , bus-to-ring coupling κ , and (b) an ADMR configuration with radius R , input coupling coefficient κ_1 and output coupling coefficient κ_2	10

2.2	(a) Spectral response and field enhancement of an APMR, and (b) spectral responses at the drop port and through port of an ADMR. In both configurations, a single MR with radius of $20 \mu\text{m}$ is assumed, with effective index $n_{eff} = 2.5$, group index $n_g = 4.3$, and 5% round-trip propagation loss ($\alpha_{rt} = 0.95$). The transmission coefficient τ is varied from 0.91 to 0.99 and the coupling is lossless ($\alpha_c = 1$). For the ADMR configuration, symmetrical coupling is assumed with $\kappa_1 = \kappa_2 = \kappa = \sqrt{1 - \tau^2}$. IL: insertion loss, ER: extinction ratio.	12
2.3	Schematic of a serially coupled microring filter consisting of N microring resonators.	15
2.4	Theoretical spectral responses of Butterworth microring filters of orders $N=1$ to 8. The drop port spectra and through port spectra are plotted in solid and dash lines, respectively.	17
2.5	(a) Schematic diagram of a 2^{nd} -order VCMR filter consisting of two single MR filters. (b) Spectral response of each MR stage. (c) Cascaded spectral response of the VCMR filter. Inset plot shows a zoomed-in view of a passband.	18
2.6	Examples of heater implementation for thermal tuning: (a) top metal heaters [50], and (b) transverse junction heaters [51] that directly inject current across the silicon waveguide core.	21
2.7	Examples of pn junctions embedded in silicon waveguide for free carrier injection: (a) the vertical pn junction configuration, (b) the transverse pn junction configuration [54]	22

3.1	(a) Schematic of a double-microring filter with bus-to-ring coupling coefficient κ_1 (coupling gap g_1) and ring-to-ring coupling coefficient κ_2 (coupling gap g_2). (b) Optical microscope image of the fabricated device (with $g_1 = 150$ nm and $g_2 = 300$ nm). (c) Simulated spectral responses of the DMR filter. (d) Cross-sectional view of the microring waveguide showing the Al thermistor, Si waveguide and the TiW heater	27
3.2	(a) Temperature distribution over a cross-section of the heater and microring waveguide. (b) Temperature distribution in the plane of the silicon waveguide when 80-mW heater power is applied to microring 1.	29
3.3	(a) Plot of the bus-to-ring and ring-to-ring coupling coefficients and the temperature changes of the corresponding coupling junctions vs. the heater power. (b) Simulated spectral responses of the filter at different heater powers over one FSR of tuning range.	31
3.4	Plots of the resonant wavelength shifts due to same-ring heating and thermal crosstalk vs. the power in (a) heater 1 and (b) heater 2. The R^2 values are the correlations of the linear fits.	33
3.5	a) Calculated (dashed lines) and optimized (solid lines) tuning curves of the DMR filter showing linear relationships between the center wavelength of the filter passband and the heater powers. The R^2 values are the correlations of the best fit curves for optimized tuning. (b) Optimized spectral responses at the drop port and through port for center wavelength $\lambda_1 = 1531.296$ nm. (c) Optimized filter spectra at the wavelength setpoints over one FSR.	34
3.6	Tuned filter spectra at six arbitrarily chosen center wavelengths, with minimum and maximum ripples of 0.58 dB and 0.74 dB, respectively, and standard deviations in the center wavelength detuning of ± 22 pm.	36

3.7	Changes in the thermistor resistances due to same-ring heating and thermal crosstalk as functions of the power in (a) heater 1 and (b) heater 2.	38
3.8	Change in the thermistor resistance as a function of the thermistor temperature.	39
3.9	Changes in the thermistor resistances and the corresponding thermistor temperatures as functions of the filter center wavelength.	39
3.10	(a) Schematic of a 4 th -order Vernier cascaded microring filter. Optical microscope images of (b) the first DMR filter stage and (c) the entire cascaded filter.	40
3.11	(a) Spectral responses of individual DMR filter stages and cascaded filter with overlapping passbands centered at zero wavelength detune. (b) Close-up view of passbands of DMR stages and cascaded filter. . .	41
3.12	(a) Unoptimized spectrum (yellow) of the first DMR filter stage and optimized spectra obtained using the dual-wavelength (blue) and single-wavelength (red) optimization methods. The dashed lines indicate the center wavelength of the respective spectrum. (b) Tuning curves for Heaters 1 & 2 in Stage 1 and Heaters 3 & 4 in Stage 2 of the VCMR filter.	43
3.13	Passband characteristics of individual DMR filter stages and of the 4 th -order VCMR filter at 1577.5 nm center wavelength.	44
3.14	Measured spectra of (a) individual DMR stages and (b) cascaded filter. Plots in (b) show the filter spectrum tuned to various wavelengths across the 32.1 nm effective FSR of the VCMR filter.	45

3.15	(a) Plot of VCMR filter spectra tuned to various different center wavelengths across its FSR. The dotted vertical lines near the center indicate the center wavelengths of the tuned spectra. (b) Plots of variations in the center wavelength detune (red dots) and 3 dB bandwidth (blue dots) of VCMR filter spectra tuned to different center wavelengths.	46
4.1	(a) Schematic diagram of the wavelength selector circuit and (b) microscope image of fabricated circuit. (c) Schematic of the DC-VMR filter and (d) image of a fabricated device. (e) Cross-sectional view of a waveguide arm of the Mach-Zehnder switch showing the embedded <i>pin</i> junction. (f) and (g) Close-up images of the <i>pin</i> junction waveguide of the MZS and the taper transition between the slab <i>pin</i> waveguide and passive strip waveguide.	52
4.2	Comparison of simulated spectral responses of 4 th -order VCMR filter and DC-VMR filter with the same bandwidth: (a) passband response, and (b) response over full FSR.	53
4.3	Output spectra of the WS circuit showing wavelength switching between $\lambda_1 = 1553nm$ from input port 1 and $\lambda_2 = 1550nm$ from input port 2: (a) when MZS is set in the “cross” state, and (b) when MZS is set in the ”bar” state. In each figure, solid lines are the output port spectra of the WS circuit, the dash lines are the spectral responses of the MZS. Inset plots show the 1 dB bandwidth of the MZS spectra centered over the selected wavelength.	55
4.4	(a) Spectral optimization of the DC-VMR filter using the single-wavelength method (red trace) and the dual-wavelength method (blue trace).	57
4.5	(a) Spectra of the DC-VMR filter tuned over the full 32.7 nm effective FSR (tuning range). (b) Thermal tuning curves of the 4 metal heaters over the tuning range in (a).	58

4.6	(a) DC voltage response of the MZS at 1558nm wavelength. (b) Measured spectra of the cross and bar states of MZS when bias current is 0 mA (c) Measured spectra of the cross and bar states of MZS when bias current is 4.22 mA	60
4.7	(a) Transmission spectra at the cross port of the MZS in the bar state when various bias current is applied to the top MZI arm (red lines) and to the bottom MZI arm (blue lines). (b) Transmission spectra at the bar port in the cross state with various bias current applied to the top MZI arm (red lines) and bottom MZI arm (blue lines).	61
4.8	(a) Plot of the wavelength of maximum rejection as function of the applied bias current for the bar state (solid line) and cross state (dashed line). (b) Insertion losses of the MZS as functions of the bias current applied to the top and bottom arms. (c) I-V plot of the <i>pin</i> junction in each MZI arm.	62
4.9	Measure spectral response at the output port 1 of the WS circuit for wavelength selection between two wavelengths $\lambda_1 = 1570.3nm$ and $\lambda_2 = 1572.2nm$	64
4.10	Experimental setup for measuring the time response of the WS circuit.	65
4.11	Time responses of (a) the 4 th -order DC-VMR filter with thermal tuning, (b) the MZS with free carrier injection, (c) the WS circuit at port 1 when the filter 1 is tuned on-and-off resonance wavelength of 1560 nm periodically at 1kHz frequency, and filter 2 is tuned off resonance. MZS is switched on-and-off to pick the optical power between filter 1 filter 2 periodically at 100 kHz frequency. (d) Frequency response of the WS circuit when the MZS is modulated by the signal generator at various frequencies, showing a 3dB-bandwidth of 300MHz.	66

4.12	Comparison of the dead time in the operation of the WS circuit: (a) "worst case" when thermal tuning of the filter is needed, (b) "best case" when only the fast MZS switching is required.	67
5.1	Simulated output spectral responses of a cascade of two 4^{th} -order filters, each with 25 GHz 3-dB bandwidth, for various frequency detunings between the two stages.	70
5.2	(a) Spectral responses of a 2^{nd} -order Butterworth filter with different bandwidths. (b) Pole locations corresponding to the spectra in (a).	73
5.3	Schematic diagram of the MZI-MRR filter of order $2N$	74
5.4	Plot of the IL-free region of a 4^{th} -order MZI-MRR filter as functions of the phase detunes ϕ_1 and ϕ_2 of the 2 MRRs on the top MZI arm.	78
5.5	Comparison of the ideal spectral responses of (a) a 4^{th} -order serially-coupled microring (CMR) filter and (b) a 4^{th} -order MZI-MRR filter. Both filter spectra have 25 GHz ripple bandwidth and no insertion loss. (c) and (d) The corresponding pole-zero diagrams of the transmission spectra (blue curves) in (a) and (b).	80
5.6	(a) Spectral responses of an ideal 4^{th} -order filter with normalized bandwidth varied from 0.02 to 0.12. Inset plots show the details of inband ripples. (b) Spectral responses of a 4^{th} -order MZI-MRR filter with bandwidth tuned from 0.02 to 0.12 by varying the MRR resonant frequencies. Comparison of the pole movements of the ideal CMR filter (black crosses) and MZI-MRR filter (red crosses) in (c) the s -plane and (d) the z -plane, the dash-line represents the unit circle in the z plane.	82

5.7	Contour plots of (a) the normalized ripple bandwidth and (b) the ripple variations for $\epsilon_m = 1$ dB, as functions of the normalized frequency detunes ϕ_1 and ϕ_2 . (c) and (d) are the ripple bandwidth and ripple variations contour plots for $\epsilon_m = 2$ dB. Both bandwidth plots are in the unit of $1/\text{FSR}$, both ripple variation plots are in the unit of dB.	84
5.8	(a) Schematic of the 4 th -order MZI-MRR filter design. (b) Microscope image of a fabricated device. (c) Schematic of the racetrack waveguide showing the embedded <i>pin</i> junction for resonance tracking. (d) Close-up view of an APMR on top arm.	85
5.9	(a) Photocurrent spectra of RT 1 at different heater powers (similar spectra are obtained for the other RTs). (b) Wavelength tuning curves for RTs as determined from the wavelengths of the peak photocurrents in (a).	86
5.10	Measured spectrum (black dash trace) of the MZI-MRR filter optimized for 50 GHz bandwidth centered at 1551 nm. Red dash trace is the fitting curve performed to extract the coupling parameters and phase detunes of the device.	87
5.11	(a) Tuning map for the 3-dB bandwidth as functions of the phase detunes of RTs 1 and 2 for maximum 3 dB ripple, based on the coupling coefficients calculated from the measured spectrum in Fig. 5.10. Plots are in the unit of $1/\text{FSR}$. (b) Measured filter spectra tuned to different bandwidths from 0.15 nm to 0.6 nm, each spectrum is normalized to the maximum power collected from all spectra.	88
6.1	(a) Schematic of the Si microring photodetector. (b) Cross-section of the <i>pin</i> junction rib waveguide on a Silicon-on-Insulator substrate. (c) Microscope image of a fabricated device.	94

6.2	(a) Measured transmission spectrum of the MR PD around the 1545.3 nm resonance wavelength at 0 V bias. (b) Dark I-V curve of the PD.	95
6.3	Power transmission spectra of the MR PD for different input powers P_{in} at (a) -15 V reverse bias and (b) 0 V bias. Insets show the measured (solid curves) and computed spectra (dashed curves) at $P_{in} = 900 \mu\text{W}$ for (a) and $P_{in} = 893 \mu\text{W}$ for (b).	96
6.4	Plots of (a) nonlinear loss coefficient in the microring and (b) shift in the resonant wavelength of the microring transmission spectra as functions of the maximum power in the microring at 0 V and -15 V reverse bias voltage.	99
6.5	Photocurrent spectra of the MR PD for different input powers P_{in} at (a) -15 V reverse bias and (b) 0 V bias. Insets show the measured (solid curves) and computed spectra (dashed curves) at $P_{in} = 900 \mu\text{W}$ for (a) and $P_{in} = 893 \mu\text{W}$ for (b).	101
6.6	(a) Plots of the peak photocurrents of the MR PD as functions of the peak optical power in the microring at -15 V reverse bias voltage and 0 V bias voltage. (b) Plots of the peak photocurrent and responsivity of the MR PD as functions of the input optical power at -15 V and 0 V bias voltage.	103
6.7	(a) Plots of the photocurrent vs. the input optical power at different wavelength detunings $\Delta\lambda$ from the linear resonance and -15 V reverse bias voltage. (b) Photocurrent (solid curve) and differential responsivity (dashed curve) at 0.1 nm wavelength detuning and -15 V reverse bias voltage.	105
6.8	Plots of the total photocurrent spectra at different signal powers for (a) -15 V bias and 1 mW optical bias, (b) 0 V bias and 1 mW optical bias, (c) 0 V bias and 0 mW optical bias. Dashed lines indicate the center wavelengths of the spectra at 10 μW signal power.	108

6.9	Plots of the small-signal photocurrent vs. the signal power for different optical bias powers and electrical bias voltages. The filled circles represent the peak values of the photocurrent spectra whereas the unfilled circles represent the photocurrent at a fixed wavelength indicated by the dashed lines in Fig. 6.8(a) and (b).	109
6.10	(a) Measured transmission spectrum of the MR APD around the 1522.35 nm resonance wavelength at 0 V bias. (b) Dark current of p^+pn^+ junction in MR APD as function of the reverse bias voltage.	112
6.11	Optical transmission spectra of the p^+pn^+ MR APD for various input optical powers at (a) -15 V bias voltage, and (b) 0 V bias voltage. Inset plots show the measured (red dash curves) and computed spectra (black solid curves) at $P_{in} = 1.38$ mW input power.	113
6.12	Plots of (a) the nonlinear loss coefficient in the MR APD for -15 V and 0 V bias voltages, and (b) nonlinear resonance shift for -15 V and 0 V bias voltages, as functions of the maximum power in the microring.	114
6.13	Photocurrent spectra for various input optical powers for (a) -15 V bias voltage and (b) 0 V bias voltage. Inset plot shows the measured (red dash curve) and computed (black solid curve) photocurrent spectra at $P_{in} = 1.38$ mW input power.	116
6.14	Plots of (a) the peak photocurrent of the MR APD as functions of the peak optical power in the microring for -15 V and 0 V bias voltages, (b) responsivities as functions of the input optical power at resonance for -15 V and 0 V bias voltages.	119
6.15	Bistable curves of the photocurrent vs. input optical power for different wavelength detunings $\Delta\lambda$ from the linear resonance. All photocurrents are measured at -15 V bias voltage.	120

6.16	(a) Time trace of the photocurrent (converted to voltage) of the p^+pn^+ MR APD for an input optical pulse train. (b) and (c) plot the rise edge and fall edge measured in (a).	120
7.1	(a) Schematic diagram of an ADMR with in-line heater design. The heater is shown in red as the silicon slab on two sides of silicon waveguide. (b) Mask layout of the 4 th -order VMR filter with in-line heater designs. The heating part of silicon slab is doped by phosphorus with an average concentration of $n = 5 \times 10^{20} cm^{-3}$. Air trench is implemented to mitigate the thermal crosstalk.	127
7.2	Thermal simulations of the in-line heaters: (a) temperature distribution along the length of the slab waveguide, (b) temperature distribution over the waveguide cross section. (c) Plot of the temperature in the silicon waveguide vs. heater power. (d) Rise time response of the in-line heater.	127
A.1	(a) Schematic diagram of the filter optimization and tuning measurement setup.(b) The close look of the wire-bonded chip. (c) The image of the settled chip and lensed fibers.	142
A.2	A Arduino based current control until for optimization and tuning in filters and wavelength selectors.	143
A.3	The current sweep of each heater in the spectral optimization process to search the peak optical power output, in optimization iteration #1.	144
A.4	The current sweep of each heater in the spectral optimization process to search the peak optical power output, in optimization iteration #2.	144
A.5	The current sweep of each heater in the spectral optimization process to search the peak optical power output, in optimization iteration #3.	145
A.6	The current sweep of each heater in the spectral optimization process to search the peak optical power output, in optimization iteration #4.	145

- A.7 The current sweep of each heater in the spectral optimization process to search the peak optical power output, in optimization iteration #5. 146
- A.8 The summary of a 5-iteration optimization. The optical power at output port gradually increases and gets to the peak at the 5th iteration. 146

List of Symbols

Constants

α	Absorption coefficient
α_L	Linear propagation loss
α_T	Thermal coefficient of a material
α_{NL}	Nonlinear propagation loss
α_{rt}	The round-trip field attenuation
β	Propagation constant of the waveguide
β_{TPA}	TPA coefficient
$\Delta\phi_{NL}$	Nonlinear phase shift
Δn	Effective index difference between two fundamental evanescent modes
ΔN_e	The change in free electron concentration
ΔN_h	The change in free hole concentration
ΔR	The change in resistance
ΔT	The change in temperature
$\Delta\lambda_{BW}$	The bandwidth of a microring filter
$\Delta\lambda_{fSR}$	The Free spectral range of a microring filter
$\Delta\omega$	Frequency detuning respect to center frequency
$\Delta\omega_{BW}$	Frequency bandwidth

$\Delta\phi$	Phase change in a waveguide
ϵ	Ripple coefficient in decibel
η	Nonlinear exponent coefficient for nonlinear phase shift and nonlinear loss
γ	Decay rate
γ_{ph}	Nonlinear coefficient for photocurrent
\hbar	Reduced Planck's constant
κ	Field coupling coefficient
κ_c	Field coupling strength
λ	The resonate wavelength of a microring resonator
λ_0	Operation wavelength
λ_m	Resonance waveguide of mode m.
μ	Energy coupling coefficient between two waveguides
μ_{ph}	Exponent coefficient for photocurrent
ν_g	Group Velocity
ω	Frequency in rad/s
ω_0	Center frequency
ϕ	Phase detune of a microring resonator
ϕ_{rt}	The round-trip phase in microring resonator
τ	Field transmission coefficient
a	The array of energy amplitudes
K	Energy transfer matrix between microrings
s	The array of input excitation
A_{eff}	Effective overlap area

C	Nonlinear coefficient for nonlinear phase shift and nonlinear loss
c	Speed of light in a vacuum inertial system.
c_k	Ripple factor in filter passband
g	Coupling gap between two waveguides
g_{opt}	Optical intensity enhancement factor
H	Transfer function
H_d	The transfer function at the drop port of microring resonator filter
H_t	The transfer function at the through port of microring resonator filter
I	Photocurrent
L	The coupling length between two waveguides
M	Avalanche multiplication
m	The resonance mode number of a microring resonator
n	Refractive index
n_g	Group index of a waveguide
n_{eff}	Effective index of a waveguide
P	Thermal power
p	Pole of a transfer function
P_b	Optical power of biasing laser beam
P_s	Optical power of signal laser beam
P_{in}	Input optical power
P_r	Optical in microring a resonator
Q	Q factor of a resonator
R	Radius of microring a resonator

r	Resistance change coefficient to temperature
R_{ss}	Small signal responsivity
s	Complex frequency
T	Power transmission
t	Thermal tuning rate
W_d	Depletion width
z	Zero of a transfer function
z^{-1}	Round trip phase delay variable

Abbreviations

ADMR Add-Drop Microring.

Al Aluminum.

APD Avalanche Photodetector.

APMR All-pass Microring.

AWG Arrayed Waveguide Grating.

CDM Code Division Multiplexing.

CMOS Complementary metal–oxide–semiconductor.

CMR Coupled Microring Resonator.

CW Continuous-wave.

CWDM Coarse Wavelength Division Multiplexing.

DBR Distributed Bragg Reflector.

DC Data Center.

DCN Data Center Network.

DC-VMR Directly Coupled Vernier Microring.

DMR Double Microring.

DSA Defect-State Absorption.

DUV Deep Ultraviolet.

DWDM Dense Wavelength Division Multiplexing.

EDFA Erbium-doped Fiber Amplifier.

FC Free Carrier.

FCA Free Carrier Absorption.

FCD Free Carrier Dispersion.

FE Field Enhancement.

FP Fabry Perot.

FSR Free Spectral Range.

InP Indium Phosphide.

IoT Internet of Things.

ITU International Telecommunication Union.

MEMS Micro-Electromechanical Systems.

MPW Multi-Project Wafer.

MRR Microring Resonator.

MZI Mach-Zehnder Interferometer.

MZS Mach-Zehnder Switch.

PD Photodetector.

PIC Photonic Integrated Circuit.

PON Passive Optical Network.

ROADM Reconfigurable Optical Add-Drop Multiplexing.

RT Race Track.

Si Silicon.

SNR Signal-to-Noise Ratio.

SOA Semiconductor Optical Amplifier.

SOI Silicon on Insulator.

SSR Small Signal Responsivity.

TDM Time Division Multiplexing.

TE Transverse Electric.

TiN Titanium Nitride.

TiW Titanium Tungsten Alloy.

TM Transverse Magnetic.

TPA Two-Photon Absorption.

VBW Variable Bandwidth.

VCMR Cascaded Vernier Microring.

WDM Wavelength Division Multiplexing.

WS Wavelength selector.

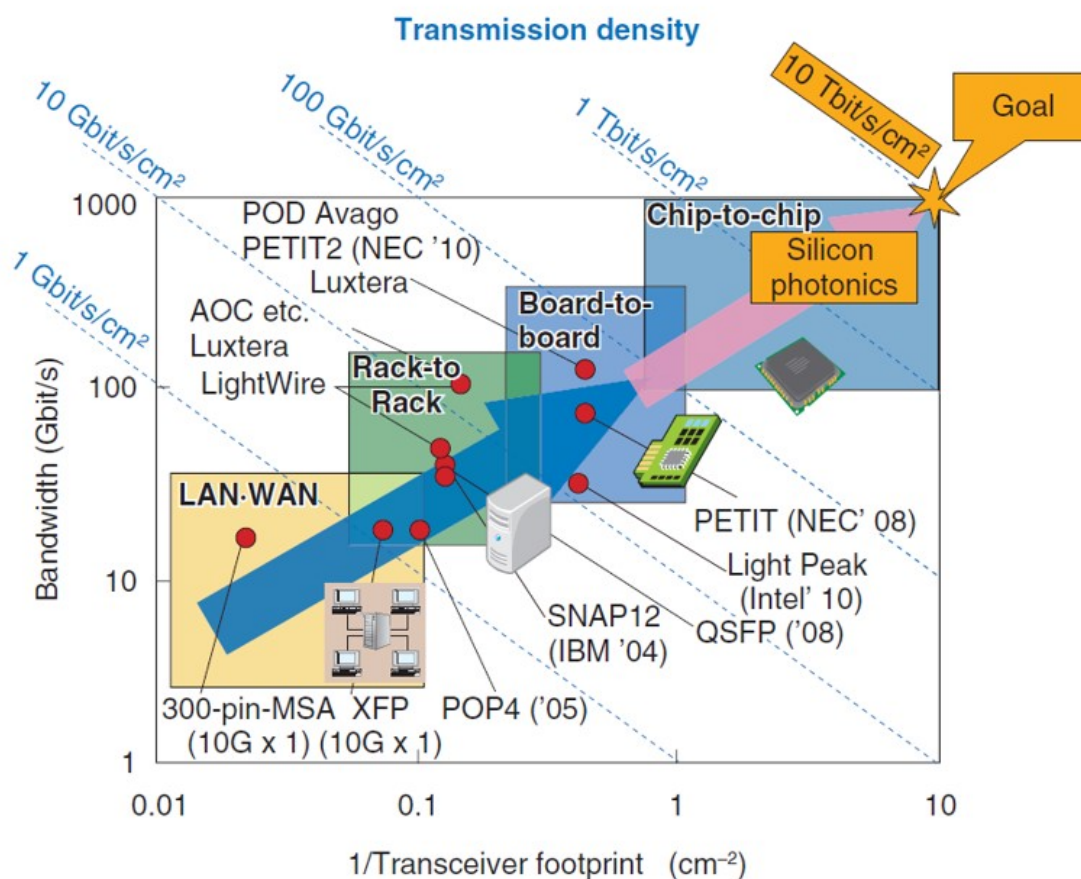
Chapter 1

Introduction

1.1 State of the Art in Optical Interconnection Technology

Over the past decade, data communication networks have experienced explosive growth in bandwidth demand, driven by emerging technologies such as 5G networks, cloud computing, artificial intelligence, autonomous vehicles, Internet of things (IoT), etc. [1]. Optical communication is playing an increasingly dominant role in delivering the technological solutions to these bandwidth requirements, via the development of flexible Wavelength Division Multiplexing (WDM) networks and optical interconnect technologies. In particular, fully reconfigurable optical networks can maximize network speed and efficiency by dynamically allocating resources (channels and bandwidths) on demand. In data link applications, for example, between servers, optical interconnects can provide orders of magnitude higher data transmission capacity than electrical cables. Fig. 1.1 briefly illustrates the road map of the optical interconnect technology, indicating a vast demand for dense integration, footprint miniaturization and channel scalability in optical networks to reduce cost and increase bandwidth capability.

Thus, traditional fibre-based optical devices are being supplemented by photonic integrated circuits (PICs) on a chip where optical signals are processed and transported in tiny optical waveguides. Although there is a wide range of materials that



AOC: active optical cable POP4: Post Office Protocol version 4
 MSA: multi-source agreement QSFP: quad small form-factor pluggable

Figure 1.1: A road map of optical interconnection technology, reproduced from [2]

can be used to build PICs such as doped glasses, III-V semiconductors, silicon nitrides, polymers and Lithium Niobate [3], silicon has emerged as the most promising candidate owing to its compatibility with existing CMOS process that is widely used in the electronics industry. Silicon also has low optical absorption and relatively high refractive index ($n = 3.45$ at telecommunication wavelengths), which allows low-loss waveguides with strong light confinement to be realized. Such strong confinement allows compact photonic devices with tight bending radii to be fabricated, resulting in a high degree of miniaturization and integration density [4]. Because of these advantages, silicon-on-insulator (SOI), which was first studied in the mid-1980s, quickly

became commercially available in the 1990s [5] and has now gained wide industry acceptance as a cost-effective material platform for building PICs for passive optical networks (PONs) in optical communication and interconnect applications. We show in Figs. 1.2 various silicon photonic devices used in optical signal processing and interconnect applications. For example, Khandokar et al. [6] and Vermeulen et al. [7] reported solution to chip-fibre coupling based on butt-coupling and grating-coupling techniques. Zhou et al. [8] experimentally demonstrated an all-silicon modulator that is working at 85 Gbaud, showing the potential in Tb/s applications [9]. In terms of optical interconnects, Zhou et al. [10][11] experimentally demonstrated a fast optical switch based on free-carrier injection technology and a 16×16 switch network based on thermal-optic effect for large-scale optical interconnect applications. Furthermore, Gehl et al. [12] and Ong et al. [13] investigated silicon photonic filters based on arrayed-waveguide-grating (AWG) and microring resonator (MRR) configurations used for multiplexing/demultiplexing optical signals. For signal detection, Li et al. [14] and Goykhman et al. [15] have realized all-silicon based photodetection with 40 GHz bandwidth. Besides, Lu [16] reported a broadband silicon photonic directional coupler for applications that are polarization sensitive.

1.2 Wavelength Division Multiplexing Technology in Optical Interconnection

In order to maximize the utility of the optical bandwidth, there exists a variety of different multiplexing mechanisms such as space (SDM), time (TDM), code (CDM), and Wavelength (WDM). Among these multiplexing techniques, WDM has huge advantages in cooperating with the tunable wavelength light source, which allows WDM technology to work with bandwidths of more than 25THz. Furthermore, WDM can transmit multiple signal streams with different wavelengths onto the same optical fiber or waveguide, which dramatically simplifies the complexity of the physical circuit layout, thus reduce the cost of deployment. In addition, since fewer optical components

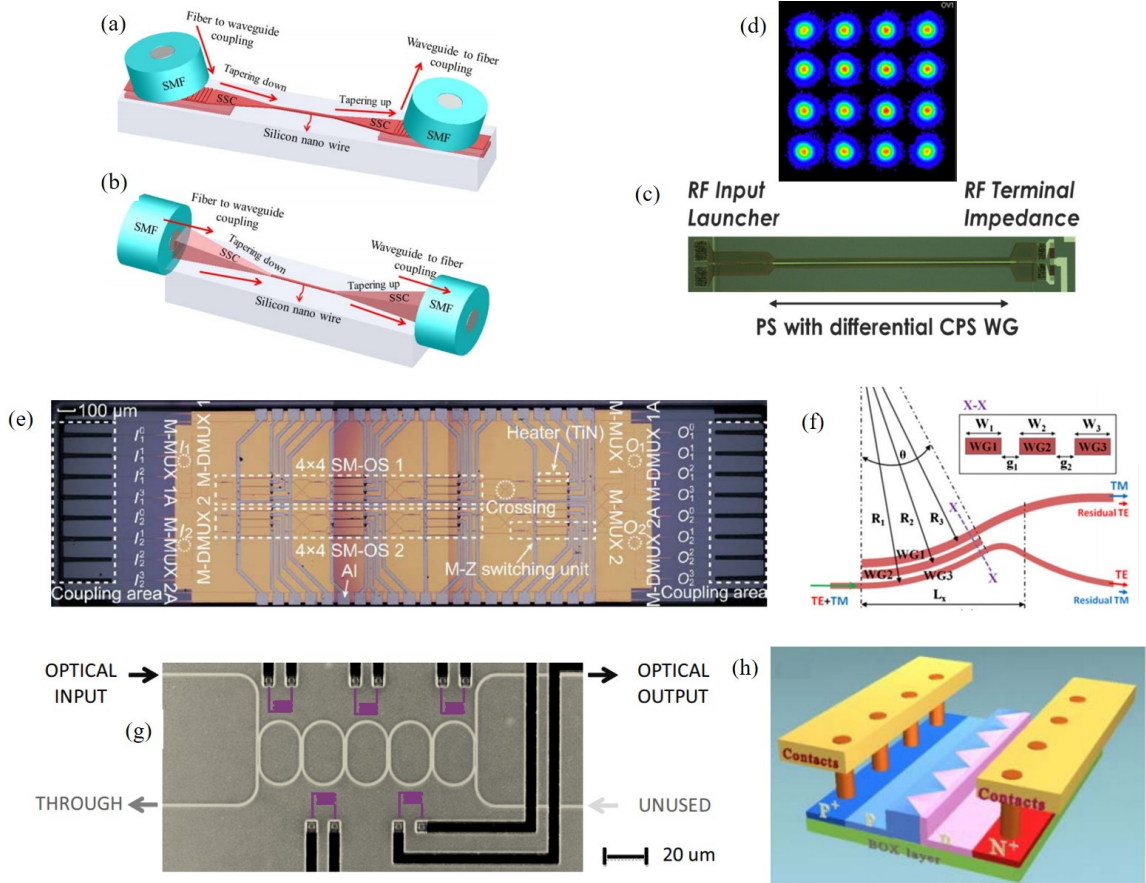


Figure 1.2: Examples of silicon photonic devices for signal processing and optical interconnect applications. (a) and (b): chip-fiber coupling with grating-coupling and butt-coupling configurations, reproduced from [7]; (c) and (d): a high baud all-silicon photonic modulator, reproduced from [8]; (e): a broadband silicon thermal-optic 2×2 switch for optical mode switching, reproduced from [11]; (f): a broadband silicon polarization beam splitter, reproduced from [16]; (g) a thermally tunable silicon photonic filter based on microring (MR) waveguide, reproduced from [13]; (h): a 40 Gb/s all-silicon photodetector, reproduced from [14].

are used, the cost of debugging, recovering, and repairing is also significantly reduced.

Wavelength division multiplexing is the technology of transmitting multiple wavelengths on a single medium path (optical fibers, waveguides etc.). Each wavelength transmitted through the medium is modulated by the data stream within its bandwidth. Such technology could dramatically expand the current capacity of the interconnect infrastructure for supporting higher data rates. In recent years, silicon photonic WDM has gained increasing popularity for optical interconnects due to its

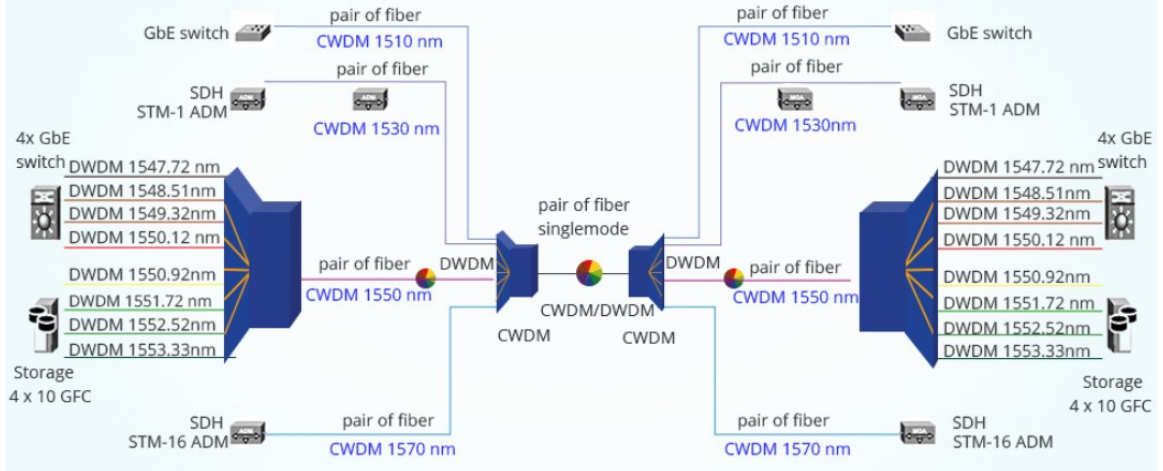


Figure 1.3: Schematic diagram of a WDM system.

low insertion loss, good compatibility to complementary metal-oxide-semiconductor (CMOS) fabrication process. The first WDM system was demonstrated in 1980s, where only two standard operational wavelengths of 1310nm and 1550nm were implemented. As the wavelength division multiplexing devices developed to have higher wavelength resolutions, coarse WDM (CWDM) technology was standardized in 2002 with its channel grid using the wavelength range from 1270nm to 1610nm. However, because wavelength output from the laser source is susceptible to temperature where $\sim 0.1 \text{ nm}/C^\circ$ fluctuation is estimated at room temperature, the channel grid for the CWDM is still as large as 20 nm, which causes serious waste in channel space. For long-distance transmission, in addition, the commonly used erbium-doped fiber amplifiers (EDFA) in WDM systems don't have enough optical gain outside of the gain bandwidth around 1550nm. Therefore, a dense WDM (DWDM) system was developed with the operation bandwidth in optical C-band and L-band (1525nm to 1610nm) for much tighter channel spacing (e.g., 50GHz). In general, the main objective of DWDM is to increase the network capacity by minimizing the wavelength spacing; whereas CWDM aims to reduce the cost where the wavelength spacing is sufficiently high to permit the transmitters to be more accurately controlled. [17].

A typical WDM system is shown in Fig. 1.3, the data streams from each ter-

minal (e.g., storage, synchronous Digital Hierarchy) are multiplexed at a different wavelength and combined to the single optical fiber, and then demultiplexed and assigned to the destination terminals. In order to adapt the WDM system into different wavelength grid standards (e.g., ITU grids), reconfigurable optical add-drop filters, tunable modulators and photodetectors are needed, which are also known as “wavelength-tunable” devices that enable wavelength reconfigurability of the device in WDM, thus maximizing the utilization of the network capacity [18]. However, due to the temperature-sensitive nature of the silicon material, relatively big bandgap energy, and fabrication constraints, challenges remain in many aspects. In particular, we summarize some of the challenges of Si-based WDM systems which will be addressed in this thesis:

- Requirement of sharp frequency transitions between adjacent channels and low channel crosstalk, which are necessary for guaranteeing signals are correctly (de)multiplexed with no distortion and loss.
- Requirement of precise wavelength reconfiguration to achieve flexibility without sacrificing system performance.
- Requirement of fast wavelength selection for data transmission with no observable latency (e.g., a few nanoseconds), which is necessary to avoid the massive usage of memory cache in optical networks.
- Requirement of flexible filter bandwidth to accommodate dynamic data transmission rates for elastic optical networks.
- Requirement of all-silicon photodetection with high responsivity, for monitoring wavelength/ optical power performance in large-scale Si PICs.

1.3 Research Objectives

This research aims to develop silicon photonic components for flexible WDM systems to address the above challenges. Specifically, the thesis consists of 4 main parts: (I) development of a high-order continuously reconfigurable optical add-drop multiplexer (ROADM) with precise temperature tracking, (II) development of a fast wavelength selection (WS) circuit for low-latency data transmission, (III) development of variable bandwidth (VBW) ROADM for elastic optical networks, (IV) investigation of responsivity enhancement in all-silicon photodetectors. The specific goals for each of these parts are as follows:

Development of high-order continuously tunable photonic filter with precise temperature tracking

- Design and implement a 4th-order photonic filter with wide tunability and high out-of-band rejection.
- Investigate the feasibility of tracking filter center wavelength using on-chip thermistors
- Develop filter optimization algorithm to automatically tune filter center wavelength and maximize the transmission.

Development of a fast wavelength selector circuit for optical transceivers

- Design and implement a scalable silicon photonic circuit architecture for fast wavelength selection from a comb of input wavelengths
- Investigate the feasibility of achieving nanosecond wavelength selection time over a broad wavelength range.

Development of VBW photonic filter for elastic optical network applications

- Develop a universal architecture for high-order bandwidth-tunable filters

- Investigate the feasibility of bandwidth tuning by resonance frequency detunings without degrading filter spectral performance
- Design and experimentally demonstrate a 4th-order VBW filter

Investigation of responsivity enhancement in all-silicon photodetectors for on-chip optical monitoring

- Design and implement *pin* junction silicon microring PDs based on two-photon absorption with resonance-enhanced responsivity
- Investigate methods for enhancing small signal responsivity of silicon microring PDs based on two-photon absorption
- Explore avalanche mechanism in silicon microring PDs to achieve high responsivity.

1.4 Organization of the Thesis

The rest of the thesis is organized as follows. In Chapter 2, the theory of high-order microring filters and mechanisms for tuning silicon photonic devices will be reviewed. In Chapter 3, we report the design, implementation and experimental performance of a 4th-order continuous tunable optical filters based on coupled microring resonators. In Chapter 4, we will demonstrate a fast wavelength selection circuit with best-case wavelength selection time of a few nanoseconds. In Chapter 5, we develop a universal VB filter configuration based on a Mach-Zehnder interferometer loaded with microring resonators. We theoretically prove that the filter bandwidth can be varied without sacrificing insertion loss. We also experimentally demonstrate a 4th-order VB filter based on this configuration in silicon photonics. In Chapter 6, we will develop all-silicon MR PDs embedded with pn junctions and explore ways to enhance their responsivities. Chapter 7 will provide a summary of the research and main achievements, as well as future research directions.

Chapter 2

Microring Resonator Circuit Architectures for Flexible WDM Systems

Due to its versatility, MRRs have become an increasingly important element in flexible and reconfigurable photonic integrated circuits, especially in silicon photonics technology. This chapter will describe the mathematical model used to design and analyze MR circuits and review important MR circuit architectures that will be used to construct flexible WDM transceivers. We will also discuss two common mechanisms used to change the refractive index in a silicon waveguide, namely, the thermo-optic effect and free-carrier dispersion. These two mechanisms will be used to achieve the reconfiguration of our WDM circuits throughout this thesis.

2.1 Microring Resonator: Device Structure and Model

Among many wavelength-selective integrated optics devices such as Arrayed Waveguide Gratings (AWGs), Mach-Zehnder interferometers (MZIs), Distributed Bragg gratings (DBRs), and Fabry-Perot (FPs) cavities, MRRs have seen widespread usage in many applications due to their compact structure, ease of fabrication, low loss. They can also be tuned over a wide range of wavelengths and form high-order transfer

functions to meet target specifications by coupling multiple MRs together.

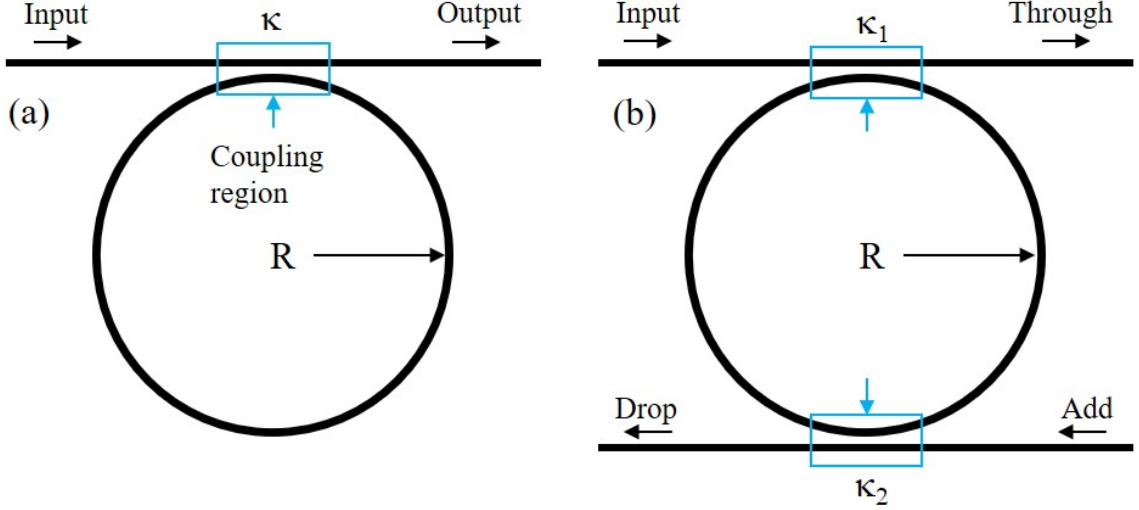


Figure 2.1: Schematics of (a) an APMR configuration with radius R , bus-to-ring coupling κ , and (b) an ADMR configuration with radius R , input coupling coefficient κ_1 and output coupling coefficient κ_2 .

Figs. 2.1(a) and (b) show basic MR structures coupled to one and two bus waveguides. An MR coupled to a single bus waveguide (Fig. 2.1(a)) is commonly known as the all-pass microring resonator (APMR) configuration, which is often used to make transmitters/receivers [19][20][21][22], notch filters [23][24][25], and optical switches [26][27][28][29]. On the other hand, an MR coupled to two bus waveguides is referred to as the add-drop microring resonator (ADMR) configuration, which is useful for wavelength multiplexing and demultiplexing applications[30][31]. In both configurations, optical power from a bus waveguide is transferred to and from the MR by evanescent wave coupling through a coupling gap between the bus waveguide and the MR waveguide. The coupling strength per unit length depends on the separation distance between the two waveguides and can be computed from

$$k_c = \frac{\pi \Delta n}{\lambda_0}, \quad (2.1)$$

where Δn is the effective index difference between the first and second-order modes of the coupler and λ_0 is the operating wavelength. The total field coupling between the

two waveguides is then given by $\kappa = \sin(k_c L)$, where L is the interaction (coupling) length between the two waveguides.

Light coupled from the bus waveguide into the microring circulates around the microring and interferes with itself after every round-trip. Resonance occurs when light accumulates a round-trip phase equal to an integer multiple of 2π , which results in constructive self-interference and strong buildup of light intensity in the microring. The condition for resonance can also be expressed as

$$m\lambda/n_{eff} = 2\pi R \quad (2.2)$$

where λ is the resonant wavelength, n_{eff} is the effective index of the microring waveguide, R is the microring radius, and m is an integer representing the resonance mode number.

In an ADMR, light from the input waveguide is partially coupled into the MR via field coupling coefficient κ_1 and is partially transmitted to the through port. The fraction of light coupled into the microring circulates around the resonator and partially couples out to the output waveguide via the coupling coefficient κ_2 . The output light is transmitted to the drop port of the ADMR. The transfer function at the drop port is given by

$$H_d(\phi_{rt}) = -\frac{\kappa_1 \kappa_2 \sqrt{\alpha_{rt}} e^{-j\phi_{rt}/2}}{1 - \tau_1 \tau_2 \alpha_{rt} e^{-j\phi_{rt}}}, \quad (2.3)$$

and the transfer function at the through port is

$$H_t(\phi_{rt}) = \frac{\tau_1 - \tau_2 \alpha_{rt} e^{-j\phi_{rt}}}{1 - \tau_1 \tau_2 \alpha_{rt} e^{-j\phi_{rt}}}. \quad (2.4)$$

In the above expressions, $\phi_{rt} = e^{-j2\pi\beta R}$ is the round-trip phase where β is the propagation constant of the microring waveguide, $\alpha_{rt} = e^{-\alpha\pi R}$ is the round-trip field attenuation in the microring where the loss constant α represents the total loss caused by absorption, bending and roughness scattering. The field coupling and transmission coefficients of the input and output coupling junctions satisfy the relation $\tau_{(1,2)}^2 +$

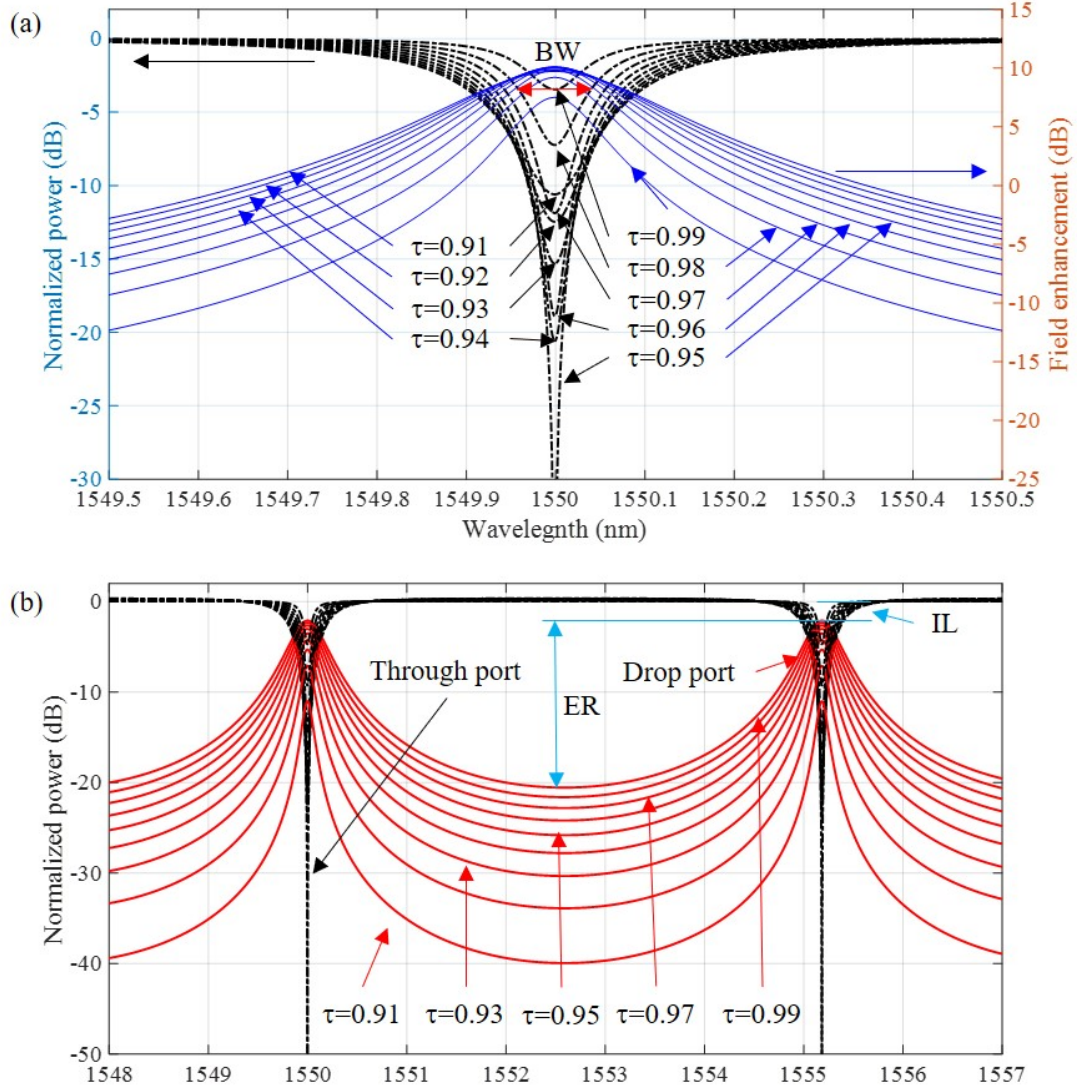


Figure 2.2: (a) Spectral response and field enhancement of an APMR, and (b) spectral responses at the drop port and through port of an ADMR. In both configurations, a single MR with radius of $20 \mu\text{m}$ is assumed, with effective index $n_{eff} = 2.5$, group index $n_g = 4.3$, and 5% round-trip propagation loss ($\alpha_{rt} = 0.95$). The transmission coefficient τ is varied from 0.91 to 0.99 and the coupling is lossless ($\alpha_c = 1$). For the ADMR configuration, symmetrical coupling is assumed with $\kappa_1 = \kappa_2 = \kappa = \sqrt{1 - \tau^2}$. IL: insertion loss, ER: extinction ratio.

$\kappa_{(1,2)}^2 = 1$. For the APMR configuration, there is no drop port ($\kappa_2 = 0$ and $\tau_2 = 1$), thus the transfer function at the through port is given by Eq. (2.4) with $\tau_2 = 1$.

Fig. 2.2(a) shows the spectral responses of an APMR for different values of the transmission coefficient τ from 0.91 to 0.99 (black traces). The MR is assumed to

have a radius R of 20 μm , effective index $n_{eff} = 2.5$, and round-trip attenuation factor $\alpha_{rt} = 0.95$. It can be seen that the spectral responses exhibit transmission dips at the resonant wavelength $\lambda = 1550$ nm. In particular, when $\tau = \alpha_{rt}$ in Eq. (2.4) the MR is said to be critically coupled as all input light is destructively interfered by the light coupled out from the microring, resulting in zero power being transmitted at the output port. For other values of τ , the MR is said to be under coupled if $\tau > \alpha_{rt}$ and over coupled if $\tau < \alpha_{rt}$. The field enhancement in an APMR is defined as the ratio between field amplitude in microring and input field amplitude:

$$FE = \frac{-j\kappa}{1 - \tau\alpha_{rt}e^{-j\phi_{rt}}}. \quad (2.5)$$

The blue traces in Fig. 2.2(a) show the spectral responses of the APMR for the different values of τ . It can be seen that the maximum field enhancement FE_{max} occurs at the resonant wavelength, and it has the highest value for critical coupling case. The resonance field enhancement is significant for many nonlinear applications that require high power, such as all-optical switch/tuning and bistable devices, which will be discussed in Chapter 6.

For an ADMR configuration, the spectral responses at the drop port (red traces) and through port (black traces) are plotted in Fig. 2.2(b). We assume the input and output coupling coefficients to be the same so that $\tau_1 = \tau_2 = \tau$. We observe that at the resonant wavelengths, power transmission is maximum at the drop port and minimum at the through port. The ADMR can thus be used to filter out a wavelength from an input WDM spectrum and "drop" it at the drop port, while allowing the rest of the spectrum to bypass to the through port. The 3dB bandwidth (in terms of wavelength) of the resonance spectrum of the ADMR is given by

$$\Delta\lambda_{BW} = \frac{2\pi^2 n_g R \sqrt{\tau_1 \tau_2 \alpha_{rt}}}{\lambda(1 - \tau_1 \tau_2 \alpha_{rt})}, \quad (2.6)$$

where n_g is the group index of the optical mode in the MR waveguide. In general, the bandwidth is inversely proportional to the coupling coefficient. The quality factor

(Q-factor) of the resonator is given by

$$Q = \frac{\lambda_m}{\Delta\lambda_{BW}}, \quad (2.7)$$

where λ_m is the wavelength of resonance mode m . The wavelength range between two adjacent resonance peaks is called the free spectral range (FSR) of the MR and can be computed from:

$$\Delta\lambda_{FSR} = \frac{\lambda^2}{2\pi n_g R} \quad (2.8)$$

The above expression shows that the FSR is inversely proportional to the microring radius.

2.2 High-Order Microring Filter Architectures

High-order filters are required in practice, especially for applications where the channel spacing is tight, spectral responses with high extinction ratio and sharp roll-off (i.e., "box-like" response) are preferred to maximize the spectral utilization. High-order filter transfer functions can be achieved by coupling multiple microring resonators together to form a microring network, such as parallel cascaded ADMRs [32][33], 2D network of coupled microring resonators [34], and APMRs assisted MZI structures [35]. In the following, we will review two important microring filter architectures that will be used in this thesis: the serially-coupled microring (CMRs) filter and cascaded microring filters.

2.2.1 Serially-Coupled Microring Filters

The serial microring coupling configuration is the most widely used architecture to construct high order filters [36]. Fig. 2.3 shows a schematic diagram of an N^{th} -order filter consisting of N serially-coupled microring resonators. We denote the energy coupling coefficient between adjacent resonators as μ_i , $i = 1 \dots N - 1$ and the energy coupling coefficient to the input and output bus waveguides μ_0 and μ_N , respectively.

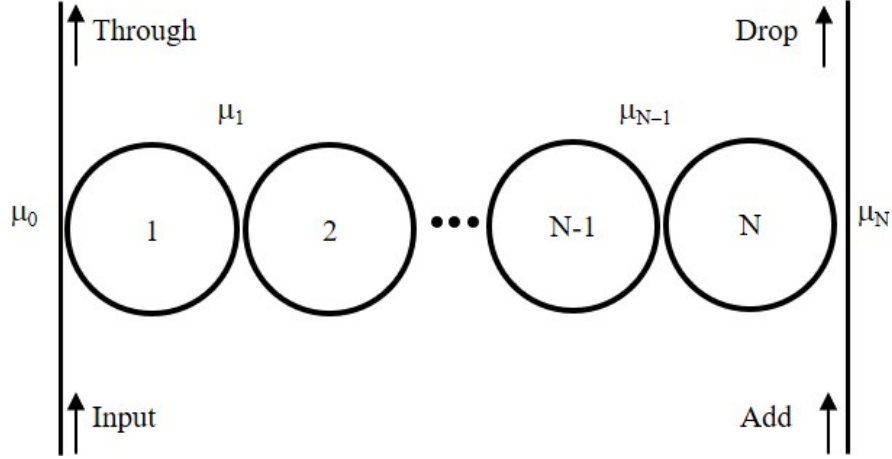


Figure 2.3: Schematic of a serially coupled microring filter consisting of N microring resonators.

The energy coupling coefficients can be related to the field coupling coefficients κ_i by

$$\mu_i = \frac{\kappa_i \nu_g}{2\pi R}, \quad 1 < i < N, \quad (2.9)$$

and

$$\mu_i = \kappa_i \sqrt{\frac{\nu_g}{2\pi R}}, \quad i = 0, N, \quad (2.10)$$

where ν_g is the group velocity in the microrings and R is their radius. For an input signal s_{in} at frequency ω applied to the input waveguide, the energy amplitude a_i in the i^{th} microring can be obtained by solving the matrix equation

$$\mathbf{K}\mathbf{a} = \mathbf{s}, \quad (2.11)$$

where $\mathbf{a} = [a_1, a_2, \dots, a_N]^T$ is the array of energy amplitudes, $\mathbf{s} = [-j\mu_0 s_{in}, 0, \dots, 0]^T$ is the input excitation vector, and \mathbf{K} is a symmetric coupling matrix [36][37]:

$$\begin{bmatrix} s + \gamma_0 & j\mu_1 & & & & \\ j\mu_1 & s & j\mu_2 & & & \\ & & \cdot & \cdot & \cdot & \\ & & & j\mu_{N-2} & s & j\mu_{N-1} \\ & & & & j\mu_{N-1} & s + \gamma_N \end{bmatrix} \quad (2.12)$$

In the above matrix, $\gamma_0 = \mu_0^2/2$ and $\gamma_N = \mu_N^2/2$ are amplitude decay rates due to coupling from microrings 1 and N to the input and output bus waveguides, respectively, and $s = j(\Delta\omega - \delta\omega_i) + \gamma_i$ is the complex frequency, where $\Delta\omega = \omega - \omega_0$ is the frequency detune from the center frequency ω_0 of the filter, $\delta\omega_i = \omega_i - \omega_0$ is the deviation in the resonant frequency of microring i from ω_0 , and $\gamma_i = \alpha\nu_g/2$ is the amplitude decay rate due to intrinsic loss. By solving for the energy amplitude a_N in microring N , we obtain an expression for the transfer function at the drop port, $H_d = -j\mu_N a_N/s_{in}$, which can be expressed in closed-form as

$$H_d(s) = \frac{(-j)^{N+1}(\mu_1\mu_2\cdots\mu_N)}{C_N(s)}, \quad (2.13)$$

where C_N is the N^{th} -continuant of the matrix \mathbf{K} given by the recursive formula:

$$C_k = \mathbf{K}_{N-k+1, N-k+1}C_{k-1} + \mu_{N-k+1}^2 C_{k-2}, \quad (2.14)$$

with $C_0 = 1$ and $C_1 = \mathbf{K}_{N,N}$. The transfer function at the through port is given by $H_t = 1 - j\mu_0 a_1/s_{in}$, which can be expressed as:

$$H_t(s) = 1 - \frac{\mu_0^2}{s + \gamma_0 + \frac{\mu_1^2}{s + \frac{\mu_2^2}{s + \cdots + \frac{\mu_{N-1}^2}{s + \gamma_N}}}}. \quad (2.15)$$

Given a desired filter bandwidth, the coupling coefficients for the Butterworth and Chebyshev filter designs[38] can be computed from

$$\mu_0^2 = \mu_N^2 = \frac{c_0 \Delta\omega_{BW}/2}{\sin(\pi/(2N))}, \quad (2.16)$$

$$\mu_k^2 = \frac{(c_k \Delta\omega_{BW}/4)^2}{\sin[(2k-1)\pi/(2N)]\sin[(2k+1)\pi/(2N)]}, \quad (2.17)$$

where $\Delta\omega_{BW}$ is the filter bandwidth. For Butterworth filters, it is the 3 dB bandwidth. For Chebyshev filters, it is the ripple bandwidth where the ripple is defined as the oscillation of the transfer function $|H_d(j\omega)|^2$ between 1 and $1/(1+\epsilon^2)$ in the passband. In the above expressions, $c_k = 1$ for Butterworth filters and

$$c_k^2 = \sin^2 \frac{k\pi}{N} + \sinh^2 \left[\frac{1}{2N} \ln \left(\frac{\sqrt{1+\epsilon^2} + 1}{\sqrt{1+\epsilon^2} - 1} \right) \right] \quad (2.18)$$

for Chebyshev filters with a ripple parameter ϵ . Fig. 2.4 shows the drop port and through port spectral responses of Butterworth microring filters of order $N = 1$ to 8 for a fixed 30 GHz bandwidth. It can be seen that a "box-like" filter response is approached as the filter order increases.

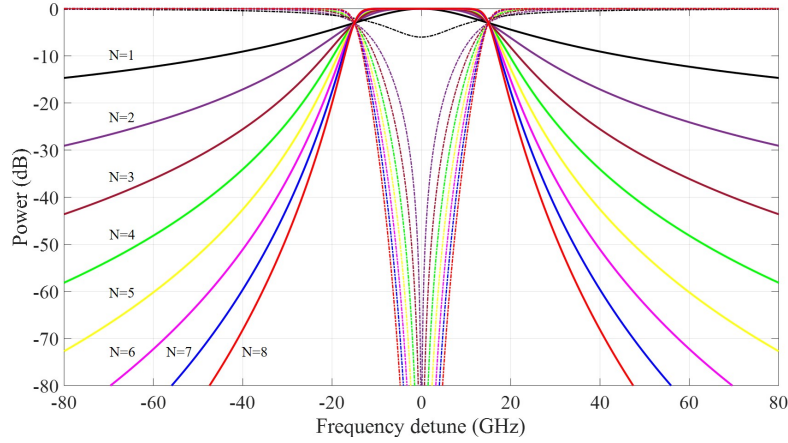


Figure 2.4: Theoretical spectral responses of Butterworth microring filters of orders $N=1$ to 8. The drop port spectra and through port spectra are plotted in solid and dash lines, respectively.

2.2.2 Cascaded MR Filters

Another way to increase the order of a MR filter response is by cascading multiple filter stages together. The transfer function of the composite response is simply the product of the transfer functions of the N cascading stages: $H_{total}(s) = H_1(s) * H_2(s) * \dots * H_N(s) = \prod_{i=1}^N H_i(s)$. Besides, it is possible to design the stages to have different FSRs so that the Vernier effect expands the effective FSR of the composite filter response. Such expansion significantly extends the tuning range of a microring filter without reducing the microring radius and incurring excessive bending loss. As an example, Fig. 2.5 (a) shows a schematic diagram of a 2^{nd} -order Vernier cascaded microring (VCMR) filter in which the FSRs of the two microrings, FSR_1 and FSR_2 , satisfy the relation

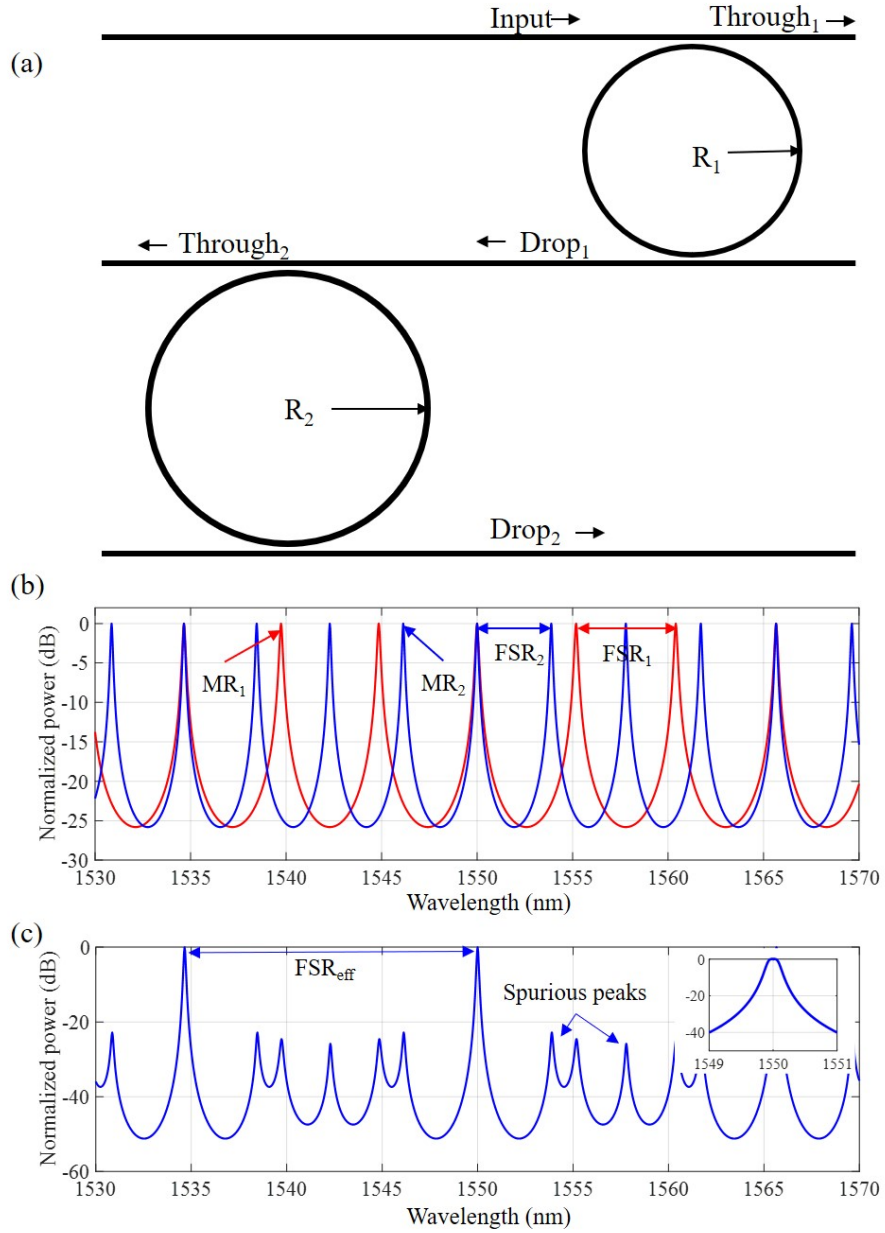


Figure 2.5: (a) Schematic diagram of a 2^{nd} -order VCMR filter consisting of two single MR filters. (b) Spectral response of each MR stage. (c) Cascaded spectral response of the VCMR filter. Inset plot shows a zoomed-in view of a passband.

$$FSR_1 \times m = FSR_2 \times n = FSR_{eff}, \quad (2.19)$$

where m and n are integers and FSR_{eff} is the effective FSR. Fig. 2.5(b) shows the spectral responses of MR 1 with radius $R_1 = 20 \mu\text{m}$ and $FSR_1 = 5.15 \text{ nm}$ and MR 2

with radius $R_2 = 26.7 \mu\text{m}$ and $FSR_2 = 3.95 \text{ nm}$. The ratio $FSR_1/FSR_2 = m/n = 3/4$. Fig. 2.5(c) shows the spectral response of the two cascaded microrings, which has an expanded effective FSR of $FSR_{eff} = 15.35 \text{ nm}$. The overlapping of the two MR spectra also produces spurious peaks in the stop band, which are kept below 23 dB in this example. A close-up plot of the passband of the VCMR filter is shown in the inset of Fig. 2.5(c), which shows a 2nd-order flat-top filter response.

2.3 Wavelength Tuning and Reconfigurability

In an integrated optical circuit, reconfigurability is typically achieved by tuning the phase of a certain component, e.g., to tune the resonant wavelength of a microring resonator or to tune the power transmission of an MZI switch on and off. Typically, phase tuning is achieved by changing the effective refractive index n_{eff} of a waveguide section of length L via the relation $\Delta\phi = \Delta n_{eff}(2\pi/\lambda)L$. There are three main mechanisms that are widely used to vary the effective index of a waveguide: (i) the thermal-optic effect [39][40][41], (ii) free-carrier dispersion effect [42][27][43][44], and (iii) the electro-optic effect [45][46]. Our work will focus on the thermal-optic effect and free-carrier dispersion effect since these two mechanisms are available for silicon material.

2.3.1 Thermal-Optic Tuning

The thermal-optic effect describes the change in the refractive index of a material as a function of the temperature. The temperature dependence of the refractive index can be expressed in the general form:

$$n(T) = n(T_0) + \alpha_T(T - T_0), \quad (2.20)$$

where $\alpha_T = dn/dT$ is the thermo-optic coefficient and T_0 is a reference temperature. For silicon, $\alpha_{si} = 1.86 \times 10^{-4} \text{ K}^{-1}$ [47] at room temperature. Since the resonance

wavelength of a microring resonator is given by $\lambda = n_{eff}(2\pi R/m)$ (m being an integer), the change in the resonance wavelength due to a change in the effective index is thus:

$$\Delta\lambda = (\Delta n_{eff}/n_{eff})\lambda. \quad (2.21)$$

For a microring resonator with circumference $L = 60\mu m$ and effective index $n_{eff} = 2.5$, the FSR is 15 nm. In order to tune a resonant wavelength (around $\lambda = 1.5\mu m$) of the microring across one FSR, we need to change the effective index by $\Delta n_{eff} = (FSR/\lambda)n_{eff} = (15nm/1500nm)2.5 = 0.025$, which requires a temperature rise in the waveguide core of about 134 °C.

Thermal tuning of silicon photonic devices is usually achieved by fabricating microheater made of a thin layer of resistive metal on top of the silicon waveguide [48], as shown in Fig. 2.6(a). Usually, the heater is at least 2 μm above the waveguide to prevent light absorption in the metal. Air trenches can be etched into the top cladding material (e.g., SiO_2) to minimize thermal crosstalk. A major disadvantage of this heater arrangement is the low tuning efficiency (~ 100 mW for 1 FSR tuning range) since the heat spreads out and only a small portion is used to raise the temperature of the silicon waveguide. In addition, the thermal time constant is long (a few tens of microseconds) which limits the tuning speed.

The heater response time can be improved by using a transverse junction heater, as shown in Fig. 2.6(b) [49], in which the silicon waveguide itself serves as the heating element. In this design, the silicon ridge waveguide is lightly doped in the core region and heavily doped in two side slabs, thus acting as a resistive element. Metal wires with low resistance are directly connected to the heavily doped silicon slab regions to form ohmic contacts. As the voltage is applied across the waveguide core, the waveguide itself heats up, resulting in high tuning efficiency (a few mW for 1 FSR tuning range) and relatively short thermal time constant (sub-microseconds to a few microseconds). However, a disadvantage of this heater design is that doping significantly increases the insertion loss of the silicon waveguide. Such loss is especially

detrimental to the performance of silicon microring resonators in terms of reduced Q factors. Also, it is challenging to minimize thermal crosstalk if adjacent devices are close to each other on the same silicon slab (as is the case in coupled microring resonators).

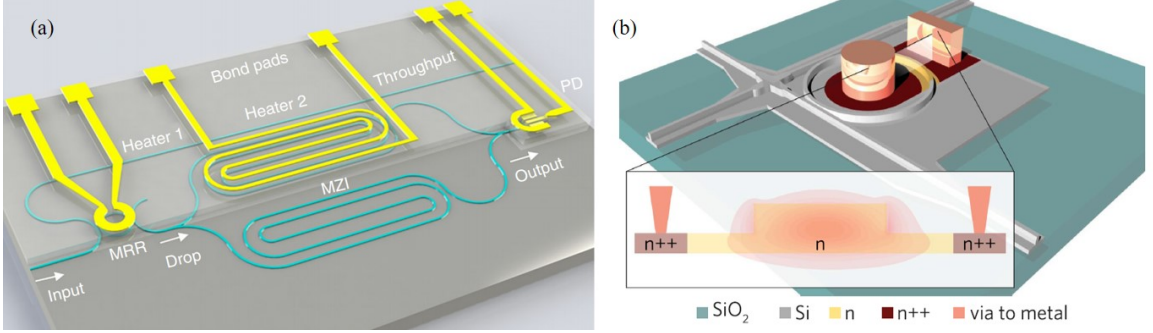


Figure 2.6: Examples of heater implementation for thermal tuning: (a) top metal heaters [50], and (b) transverse junction heaters [51] that directly inject current across the silicon waveguide core.

2.3.2 Free Carrier Dispersion

Another way to change the effective index of a silicon waveguide is by changing the free carrier density in the silicon waveguide. For light around $1.55 \mu\text{m}$ wavelength, changes in the free electron density ΔN_e and hole density ΔN_h will induce changes in the refractive index Δn and absorption (or loss) $\Delta\alpha$ in the material given by the empirical formulas [52][53]:

$$\Delta n = \Delta n_e + \Delta n_h = -[8.8 \times 10^{-22} \Delta N_e + 8.5 \times 10^{-18} \Delta N_h^{0.8}], \quad (2.22)$$

$$\Delta\alpha = \Delta\alpha_e + \Delta\alpha_h = 8.5 \times 10^{-18} \Delta N_e + 6.0 \times 10^{-18} \Delta N_h, \quad (2.23)$$

where Δn_e and Δn_h are the index changes resulting from changes in the electron and hole density, respectively. Likewise, $\Delta\alpha_e$ and $\Delta\alpha_h$ are the changes in absorption resulting from changes in the electron and hole density. In the above formulas ΔN_e and ΔN_h are in units of cm^{-3} . In practice, the free electron and hole density are varied by injecting carriers into pn junctions, such as shown in Figs. 2.7, under forward bias

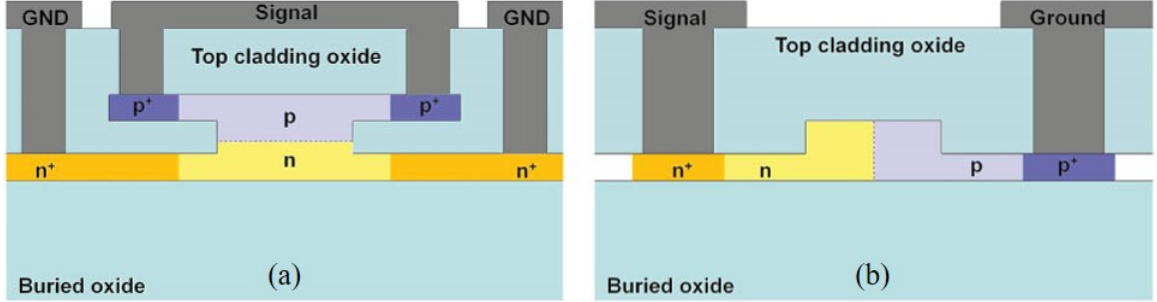


Figure 2.7: Examples of pn junctions embedded in silicon waveguide for free carrier injection: (a) the vertical pn junction configuration, (b) the transverse pn junction configuration [54]

voltages. It is relatively easy to produce changes in ΔN_e and ΔN_h at a level of $\sim 10^{17} \text{cm}^{-3}$. The corresponding changes in the index Δn and absorption $\Delta \alpha$ are calculated to be 1.12×10^{-3} and 7.25 cm^{-1} , respectively. Compared to the thermo-optic effect (which is almost lossless), free carriers provide an order of magnitude smaller index change with non-negligible excess loss in the waveguide. The main advantage of the free carrier dispersion effect is the short response time, which is determined by the free-carrier lifetime in the junction. Reported works [27][43][44] showed average response time in the tens of picoseconds to nanoseconds, which is at least 3 - 4 orders of magnitude faster than thermal tuning. Free carrier dispersion is typically employed to realize fast switches and high-speed modulators. An MZI switch based on free carrier injection in a pn junction will be demonstrated as part of a fast wavelength selection circuit in Chapter 4[55].

2.4 Summary

In this chapter, we reviewed the basic properties of microring resonators and how they are used to construct high-order optical filters. We also discussed two widely used mechanisms for tuning the refractive index of silicon, namely the thermo-optic effect and free-carrier dispersion. The microring resonators are used as the main building blocks for realizing reconfigurable silicon photonic WDM circuits in the rest of the

thesis.

Chapter 3

Broadband Tunable Multiplexer/Demultiplexer with Precise Temperature Tracking

Although Silicon-on-Insulator has gained widespread industry acceptance as a cost-effective and CMOS compatible material platform for photonic integrated circuits (PICs), the technology does possess several challenges that still need to be addressed. One long-standing issue is the fairly limited refractive index tuning range that can be achieved in the silicon material for applications such as broadband-tunable filters. Tunable silicon photonic filters typically rely on the thermo-optic effect, which provides the largest index tuning range among the various tuning mechanisms available [47][56][57]. For example, tunable silicon microring filter of various orders have been reported with tuning range over the full free spectral range (FSR) of the microring resonators [58][59][60][61]. However, since the FSR of a microring resonator scales inversely with the microring radius, bending loss typically limits the FSR of these filters to less than about 20 nm. Recently, a 3rd-order filter was reported with a tuning range of 32 nm using compact Si microrings with 2.5 μm radius [62]; however, both the insertion loss and heating power required to tune the device over one FSR were quite high, which could be partially due to the small microring size employed.

One well-know scheme to overcome the FSR limitation and achieve wider tuning range is to employ the Vernier effect, which was discussed in Chapter 2. However, to

date very few high-order Vernier microring filters have been demonstrated in SOI and all have relied on the serial microring coupling configuration [63][64]. For example, Jayatilaka *et.al.*[63] reported a 2nd-order Vernier microring filter with an effective FSR of 36 nm and 15 dB stopband rejection. The same group later reported a 4th-order Vernier microring filter with an effective FSR of 37.2 nm and 3-dB bandwidth of 32 GHz, with a variation of 7 GHz (or 20% of the bandwidth) due to tuning [64], and the variation in the center wavelength due to tuning was not reported. Due to the close proximity of the heaters in the serial coupling configuration, severe thermal crosstalk occurs when one set of microrings need to be tuned over a large wavelength range. The problem is exacerbated in high-order Vernier filter devices since the two sets of microrings with different FSRs are tuned by very different amounts, and thus can have vastly different temperatures depending on the target filter wavelength. This thermal crosstalk can lead to resonance misalignment and variations in the coupling coefficients, which cause distortion in the filter shapes, high spurious peaks, and variations in bandwidth and insertion loss.

In this chapter, we propose and demonstrate an alternative high-order Vernier microring filter design based on a cascade of two separate microring stages with different FSRs. The Vernier scheme was briefly described in Chapter 2. Here, we aim to realize a 4th-order VCMR filter in which each stage is a 2nd-order double-microring (DMR) flat-top filter consisting of two coupled microring resonators. The spectra of the two stages are overlapped to yield a 4th-order flattop filter response. By keeping the two stages sufficiently far apart, thermal crosstalk between the stages can be minimized which simplifies the tuning process and improves wavelength tuning accuracy. In addition, by taking into account the thermal crosstalk between the two microrings in each stage, each DMR filter stage can be tuned across its FSR with a high degree of tuning accuracy and repeatability [62]. This allows us to separately calibrate and optimize each DMR filter stage and tune the VCMR filter to any specified center wavelength without further optimization of the overall spectral response.

Measurements showed that our VCMR filter has a tuning range of 32.1 nm, with a wavelength tuning accuracy of ± 14.9 pm and 3-dB bandwidth variation of ± 6.5 %. The wavelength tuning accuracy of our filter is the highest to date among previous demonstration in silicon MR based filters [65][66][67]. In addition, using integrated on-chip thermistors placed near the microrings, we could monitor the local temperatures of the microring resonators and show that a temperature tracking accuracy of $\pm 0.1^\circ\text{C}$ can be achieved over the full tuning range. The ability to track the local temperatures of the microrings provides a mechanism for monitoring the center wavelength of the filter. It also provides an indirect mechanism for monitoring the spectral performance of the device in applications where optical spectral scanning of the filter is not available during the device operation.

The rest of this chapter is organized as follows. In Section 3.1, we report the design, implementation and tuning performance of a 2nd-order DMR filter. This DMR filter stage is used to construct a VCMR filter with wide tuning range in Section 3.2. The chapter is summarized in Section 3.3.

3.1 Design and Performance of A Double-Microring Filter

3.1.1 DMR Filter Design and Fabrication

Fig. 3.1(a) shows a schematic diagram of a DMR filter consisting of two coupled microring resonators. We chose the double microring design rather than a higher-order filter design since it is easier to tune the device and quantify the thermal crosstalks. We realized the DMR filter on an SOI platform consisting of a 220 nm thick Si layer lying on a 2 μm thick SiO_2 buffer layer. The silicon waveguides were designed for TE polarization and had a nominal width of 500 nm with a 2 μm thick SiO_2 overlapping layer. We designed the DMR filter to be the first stage of a VCMR filter (to be described in Section 3.3), with an FSR of 7.8 nm, 3-dB bandwidth of 25 GHz, in-

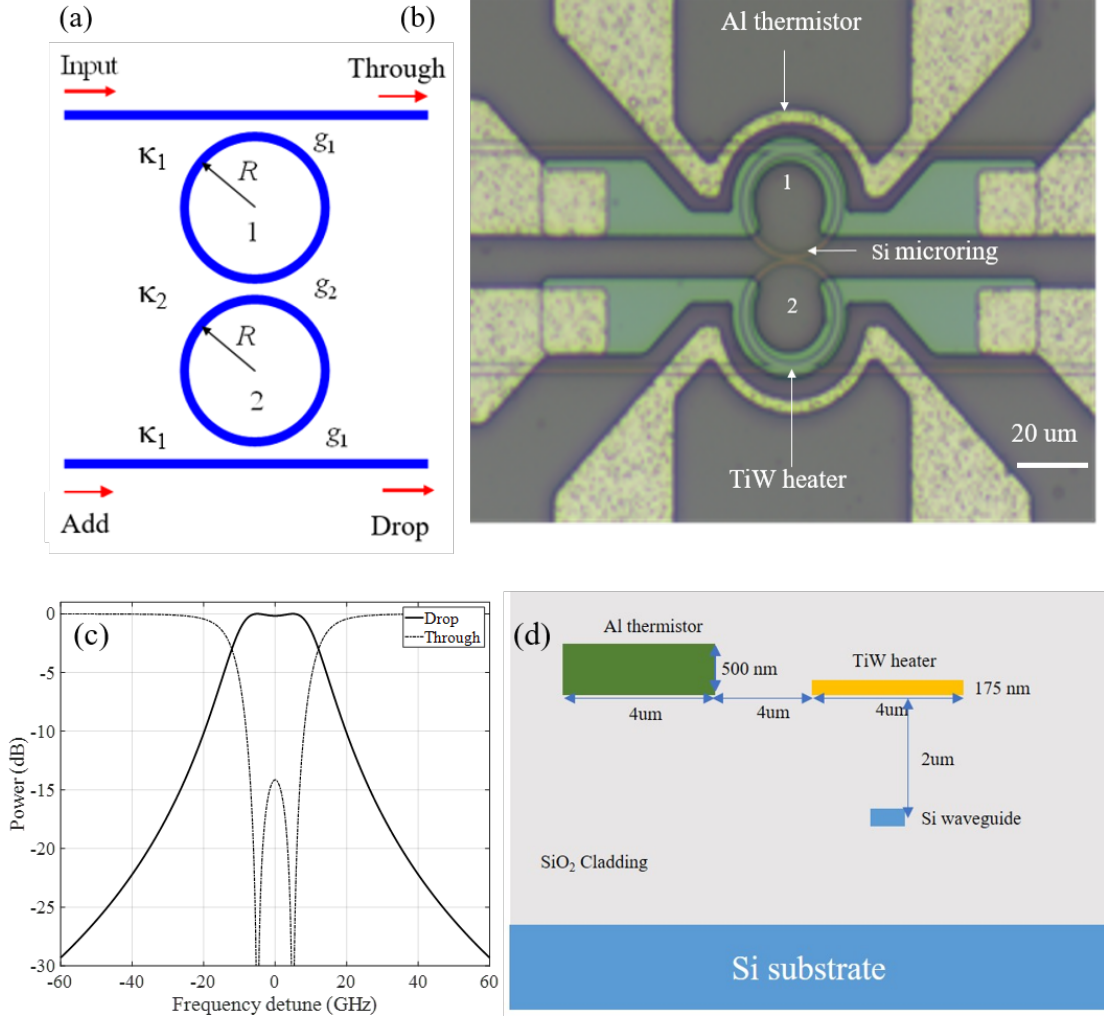


Figure 3.1: (a) Schematic of a double-microring filter with bus-to-ring coupling coefficient κ_1 (coupling gap g_1) and ring-to-ring coupling coefficient κ_2 (coupling gap g_2). (b) Optical microscope image of the fabricated device (with $g_1 = 150$ nm and $g_2 = 300$ nm). (c) Simulated spectral responses of the DMR filter. (d) Cross-sectional view of the microring waveguide showing the Al thermistor, Si waveguide and the TiW heater

band ripple of less than 1 dB and maximized skirt roll-off. To obtain an FSR of 7.8 nm for the TE mode, we set the radius of the two microring resonators to be 11.27 μm . The transfer functions of the DMR filter at the through port (H_t) and drop port (H_d) are given by:

$$H_t(z) = \frac{\tau_1 - \tau_2(1 + \tau_1^2)z^{-1} + \tau_1 z^{-2}}{1 - 2\tau_1\tau_2 z^{-1} + \tau_1^2 z^{-2}} \quad (3.1)$$

$$H_d(z) = \frac{j\kappa_1^2 \kappa_2 z^{-1}}{1 - 2\tau_1\tau_2 z^{-1} + \tau_1^2 z^{-2}} \quad (3.2)$$

where κ_1 is the bus-to-ring coupling coefficient, κ_2 is the ring-to-ring coupling coefficient, $\tau_{1,2} = \sqrt{1 - \kappa_{1,2}^2}$ and $z^{-1} = e^{-j\phi_{rt}}$ is the roundtrip phase delay variable, with ϕ_{rt} being the roundtrip phase of the microrings. To achieve the specified filter passband characteristics, we used a 2nd-order Chebyshev filter design [38], with field coupling values $\kappa_1 = 0.3$ and $\kappa_2 = 0.06$. These coupling values correspond to bus-to-ring coupling gap $g_1 = 150$ nm and ring-to-ring coupling gap $g_2 = 300$ nm. Fig. 3.1(c) shows the computed spectral responses of the designed filter.

To tune the resonance wavelengths of the microring resonators, symmetric microheaters were fabricated over the microrings, as shown by the optical microscope image in Fig. 3.1(b). The heaters were made of a TiW alloy. The heaters were made of a TiW alloy (10 % Ti and 90 % W) with 175 nm thickness and 4 μm width, covering an arc length of 240° around each microring. Fabrication constraints [68] required a minimum separation of 10 μm between the two heaters, so that the ring-to-ring coupling region was not covered by the heaters. The contact leads of the heaters were made of Al, with a thickness of 500 nm and a width of 15 μm . To monitor the temperatures of the microring waveguides, we also fabricated symmetric thermistors out of the same Al metal traces next to the heaters. The thermistor covers a 180° arc around each heater, with its width narrowed down to 4 μm to increase the thermistor resistance. Due to fabrication constraints, the separation between the thermistor and the heater had to be kept at least 4 μm . A side view of the locations of heater and thermistor are shown in Figs. 3.1 and (d). The DMR filter was fabricated through the Applied Nanotools Nano-SOI fabrication service [68], which employed electron beam lithography to define the waveguide and microring structures. An image of a fabricated device is shown in Fig. 3.1(b).

3.1.2 Thermal Analysis of DMR Filter

In the operation of the VCMR filter, each filter stage needs to be tuned over its full FSR. For our microring and heater design, we found experimentally that it took

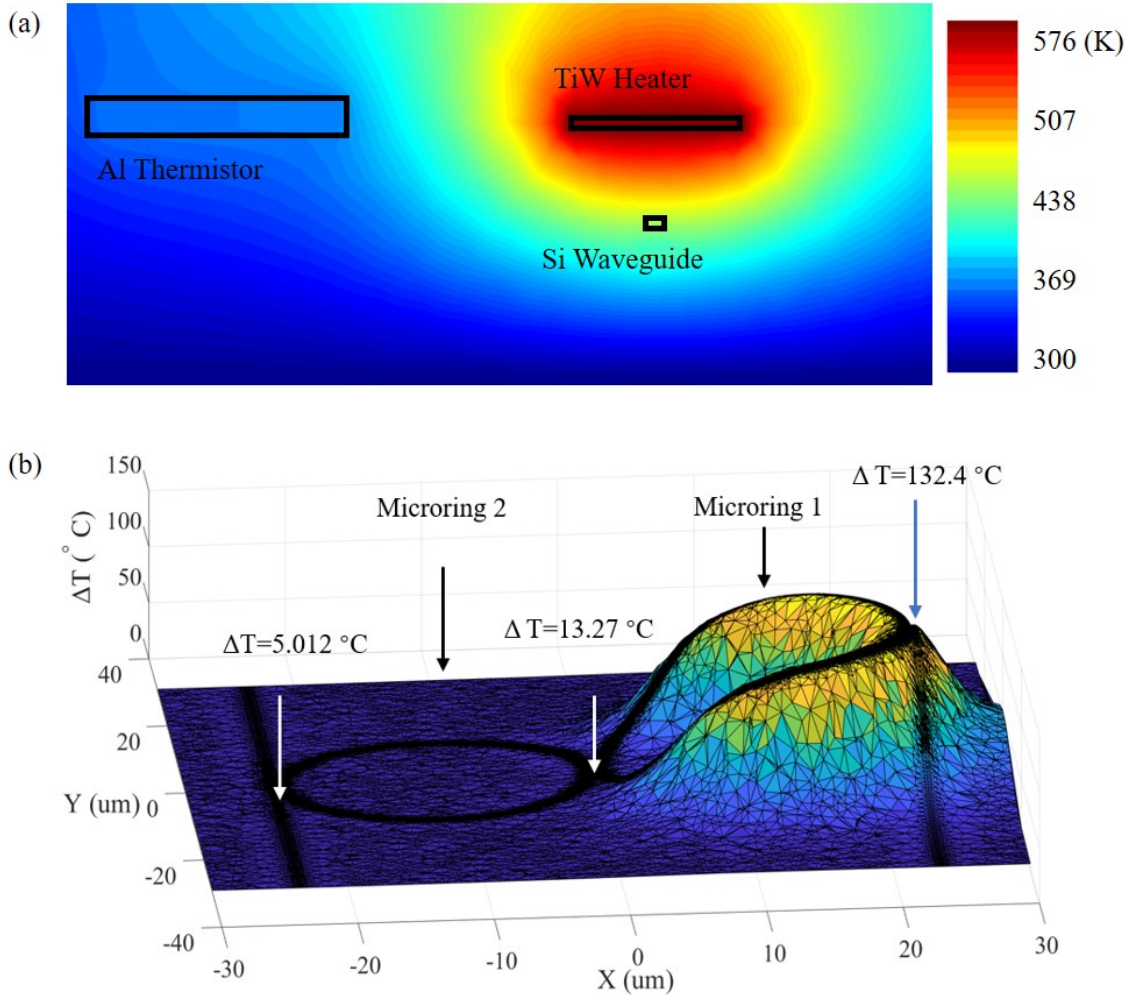


Figure 3.2: (a) Temperature distribution over a cross-section of the heater and microring waveguide. (b) Temperature distribution in the plane of the silicon waveguide when 80-mW heater power is applied to microring 1.

about 80 mW of power to tune each microring over its FSR, which corresponds to a maximum temperature rise of about 135° C. To evaluate the effect of such large temperature change on the filter performance, we performed thermal simulations of the DMR device to determine how much the coupling coefficients and hence, the spectral characteristics of the filter, change due to heating. We applied power to one heater and performed 3D simulation of the temperature distribution over the device structure. The thermal simulation was performed by solving the steady-state heat diffusion equation using the Lumerical software, which is based on the Finite Element

method. The simulated structure included the Si substrate, with the bottom Si surface held at 300 K, and the metal strips for the heater (TiW) and the thermistor (Al). The chip was capped with a 300 nm-thick SiO₂ protection layer, with convective boundary condition applied to the top SiO₂ surface to account for heat transfer from the chip to air. Thermal insulating boundary condition was applied to the four sidewalls of the simulation domain, which were placed sufficiently far from the microring device so that they did not affect the simulated temperature profile of the device.

Fig. 3.2(a) shows the cross-sectional temperature distribution when 20mW is applied to the TiW heater. 80mW heating power is the power to tune the microring filter over 1 FSR. We find that the heater temperature is 570K, the average temperature in the silicon waveguide is 430 K, while the average temperature of the thermistor is 345 K. Fig. 3.2(b) shows a sample temperature distribution in the plane of the silicon waveguide obtained for 80 mW of power applied to heater 1. We observe that while the bus-to-ring coupling junction directly below the heater experiences a large temperature rise, the temperature change over the ring-to-ring coupling junction is much less. From the changes in the waveguide temperatures, we computed the new waveguide modes and effective indices, which were then used to calculate the coupling coefficients of the bus-to-ring and ring-to-ring coupling junctions. Fig. 3.3(a) plots these coupling coefficients and the corresponding temperature changes as functions of the applied heater power. Over the range of heater power required to tune the microrings by one FSR (0 - 80 mW), we find that the bus-to-ring and ring-to-ring coupling coefficients change by 5.6 % and 0.59 %, respectively. The much smaller variation in the ring-to-ring coupling is due to the fact that the heater does not cover the coupling junction between the two microrings. To evaluate the impact of these coupling variations on the filter performance, we plotted in Fig. 3.3(b) the spectral response of the DMR filter over this heater power range. We observe that the device maintains its filter shape across the tuning range, with the 3-dB bandwidth remaining relatively unchanged while the in-band ripple increases slightly from 0.45 dB to 0.75

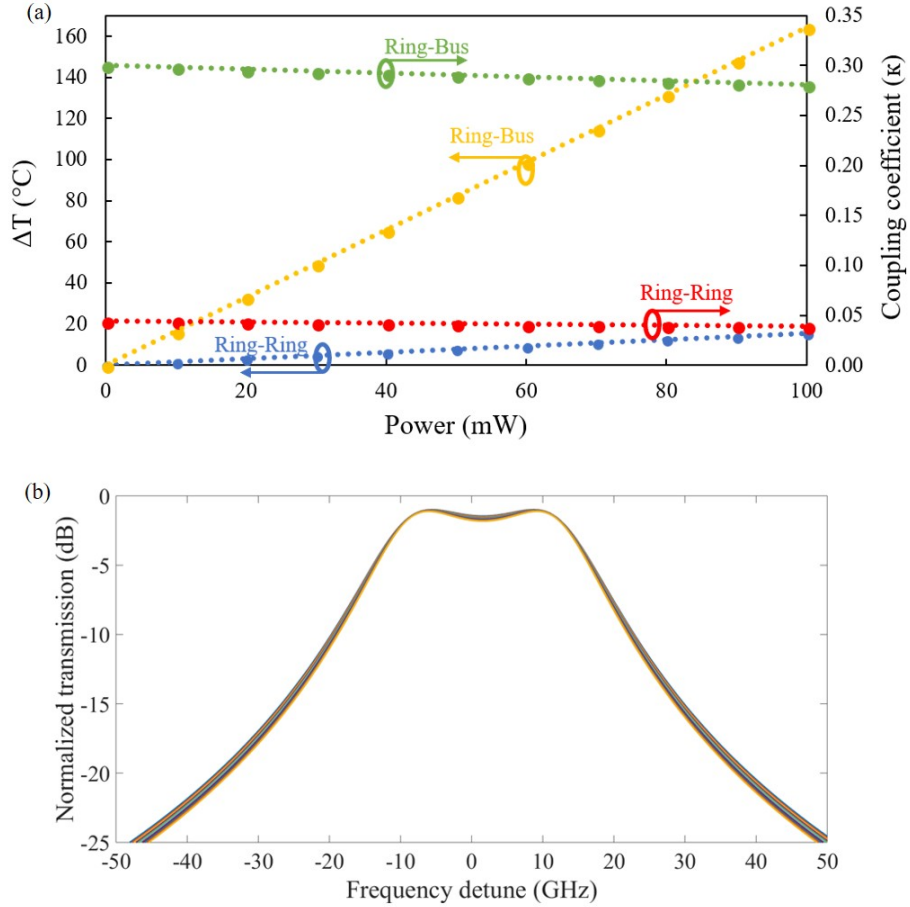


Figure 3.3: (a) Plot of the bus-to-ring and ring-to-ring coupling coefficients and the temperature changes of the corresponding coupling junctions vs. the heater power. (b) Simulated spectral responses of the filter at different heater powers over one FSR of tuning range.

dB (in the experiment the filter shape can be further optimized to reduce this ripple). These simulation results show that the DMR filter design is robust to temperature tuning across its FSR.

3.1.3 Tuning Performance of the DMR Filter

We measured the spectral response of the DMR filter using continuous-wave (CW) light from a tunable laser over the 1480 nm - 1630 nm wavelength range. The laser light was adjusted to TE polarization using a polarization controller and butt-coupled to the input waveguide of the DMR via a lensed fiber. The transmitted light in

the output waveguide was collected using another lensed fiber and detected with a photodetector and power meter. To control and tune the microring resonances, each heater was probed by a Tungsten tip mounted on a Signatone S-725 high precised positioner. The other end of the probe was connected to a microcontroller that was used to control the applied DC voltage and measure the current through the heater. All measurements were performed with the chip at room temperature.

We first determined the tuning efficiency and thermal crosstalks of the device by measuring the resonant wavelength shifts of the microrings due to the power applied to each heater. The resonance shift of each individual microring was determined by measuring the wavelength of the resonance peak of that microring at the output port when it was sufficiently detuned from the other. Fig. 3.4 plots the resonant wavelength shift due to heating of the same microring (same-ring heating) and the resonance shift due to heating of the other microring (thermal crosstalk) as functions of each heater power. We observe that the resonant wavelength shifts due to same-ring heating and thermal crosstalk both exhibit linear dependence on the heater power. From the linear best fit lines of the shifts due to same-ring heating, we obtain a tuning rate of $t_{11} = 78.34$ pm/mW for microring 1 and $t_{22} = 99.25$ pm/mW for microrign 2. These values are lower than previously reported for single silicon microring resonators (e.g., 296 pm/mW in [60], 133 pm/mW in [69]), which can be attributed to the different design, dimensions and location of our heaters, and the fact that our heaters covered only a 240° arc instead of the full microring circumference. From Fig. 3.4 we also note that each microring experienced significant thermal crosstalk due to the other heater. The rate of resonance change of microring 1 due to heater 2 is $t_{12} = 5.13$ pm/mW and that of microring 2 due to heater 1 is $t_{21} = 4.58$ pm/mW. These crosstalks will be taken into account to generate tuning curves for the DMR filter as described below.

The tuning curves of the DMR filter were generated by determining the heater powers required to tune the microrings to a set of wavelengths about 50 GHz apart

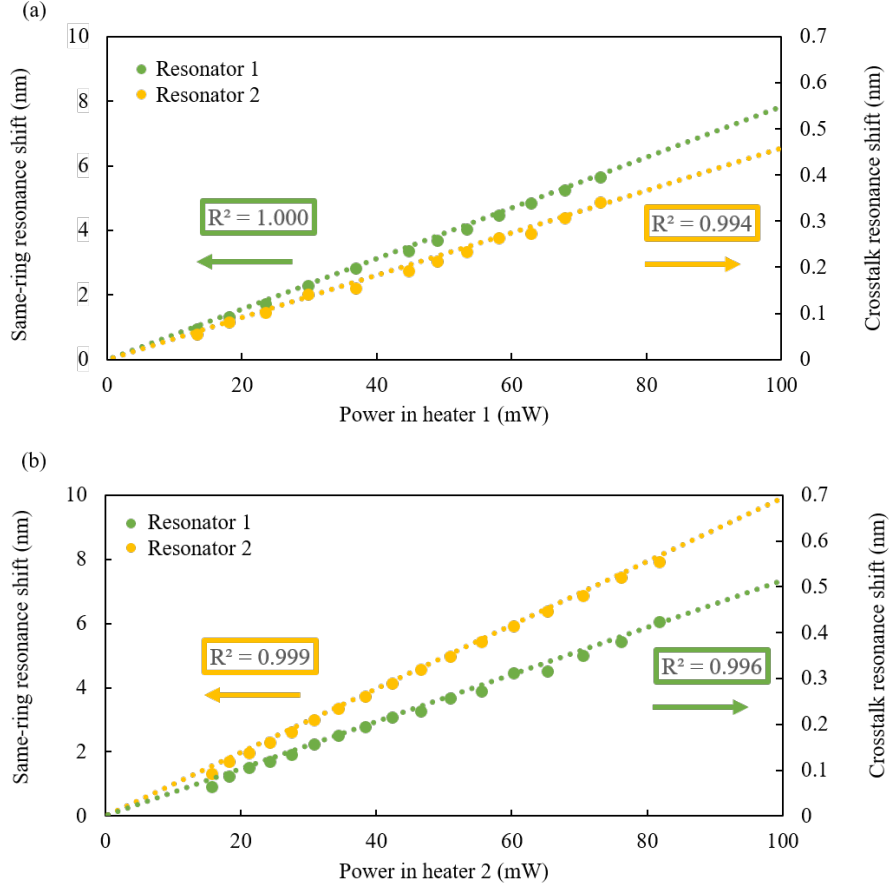


Figure 3.4: Plots of the resonant wavelength shifts due to same-ring heating and thermal crosstalk vs. the power in (a) heater 1 and (b) heater 2. The R^2 values are the correlations of the linear fits.

over one FSR (1531 - 1539 nm). Starting from an initial resonance detuning of 0.6 nm between the two microrings (caused by fabrication variations), we brought the two resonances into alignment and optimized the filter shape by scanning the resonant wavelength of each microring over the passband to minimize the ripple. The optimized spectra at the drop port and through port are shown in Fig. 3.5(b). Once the optimum heater powers $P_1(\lambda_1)$ and $P_2(\lambda_2)$ for the first wavelength setpoint ($\lambda_1 = 1531.296$ nm) were obtained, we then calculated the heater powers for the other wavelength setpoints using the linear relationships in Fig 3.4. In particular, the powers $P_1(\lambda_i)$ and $P_2(\lambda_i)$ of heaters 1 and 2 required to tune the filter to center

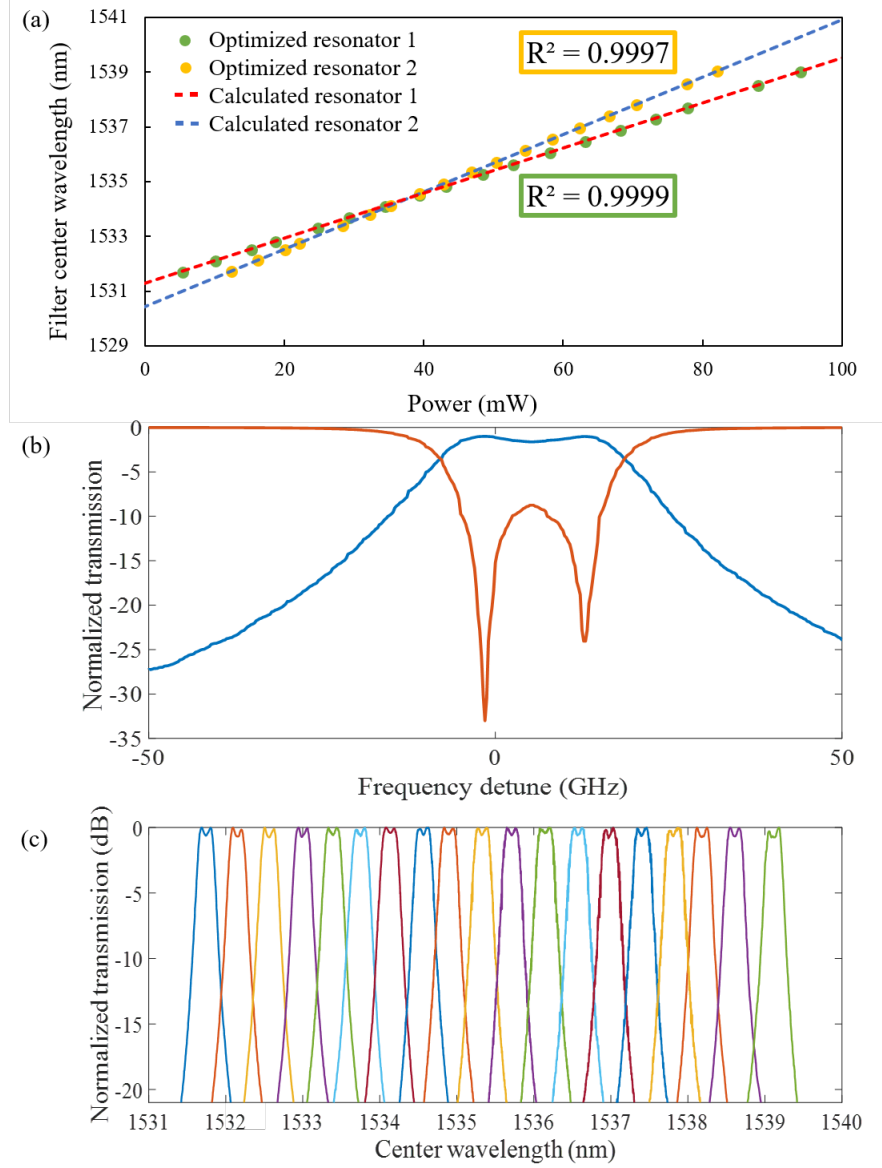


Figure 3.5: a) Calculated (dashed lines) and optimized (solid lines) tuning curves of the DMR filter showing linear relationships between the center wavelength of the filter passband and the heater powers. The R^2 values are the correlations of the best fit curves for optimized tuning. (b) Optimized spectral responses at the drop port and through port for center wavelength $\lambda_1 = 1531.296$ nm. (c) Optimized filter spectra at the wavelength setpoints over one FSR.

wavelength λ_i are found by solving the equations:

$$\lambda_i - \lambda_1 = t_{11}[P_1(\lambda_i) - P_1(\lambda_1)] + t_{12}[P_2(\lambda_i) - P_2(\lambda_1)] \quad (3.3)$$

$$\lambda_i - \lambda_2 = t_{21}[P_1(\lambda_i) - P_1(\lambda_2)] + t_{22}[P_2(\lambda_i) - P_2(\lambda_2)] \quad (3.4)$$

where the tuning rates t_{11} , t_{12} , t_{21} , t_{22} are give above. The plots of the calculated center wavelength vs. power for each heaters are shown by the dashed lines in Fig. 3.5(a). To validate these tuning curves, we applied the predicted heater powers to tune the filter to each wavelength setpoint. At each wavelength, the filter spectral response obtained was very close to the optimized filter shape at the initial setpoint λ_1 . To ensure that the filter response was optimum, we further adjusted the current through each heater to minimize the in-band ripple. Fig. 3.5(c) shows the optimized filter spectra, which have a maximum ripple of 0.7 dB and average 3-dB and 10-dB bandwidths of 27.5 ± 0.6 GHz and 75 ± 2 GHz, respectively. The average insertion loss across all the spectra is 2.5 ± 0.2 dB. By fitting the measured spectra with a 2nd-order filter transfer function, we determined the coupling coefficients of the device to be $\kappa_1 = 0.29$ ($\pm 2.5\%$), $\kappa_2 = 0.065$ ($\pm 2.5\%$), and $\kappa_3 = 0.30$ ($\pm 2.5\%$), where κ_3 is the bus-to-ring coupling at the output. In Fig. 3.5(a) we also plotted the optimized tuning curves (solid lines) for comparison with the calculated tuning curves. It can be seen that the two sets of tuning curves are very close to each other, both showing strongly correlated linear relationships between the heater powers and the center wavelength. The close agreement between the optimized and calculated tuning curves also implies that changes in the coupling coefficients due to heating did not cause significant distortion to the filter shape, as confirmed by the thermal simulations results in Fig. 3.3(b).

The optimized tuning curves can be used to determine the heater powers required to tune the filter center wavelength to any arbitrary value. To estimate the tuning wavelength accuracy, we calculated the standard deviation between the center wavelengths of the data points of the optimized spectra in Fig. 3.5(a) and those values predicted by the best fit lines. We obtained a wavelength uncertainty of ± 27 pm (or ± 3.4 GHz), which is about three times the specified wavelength stability of our laser (± 10 pm). We also note that this value is comparable to the wavelength accuracy of some commercial tunable filter (e.g., [70]) and can be further improved with more

precise control of the powers applied to the heaters.

In the continuous tuning operation of the filter, given a desired center wavelength of the passband, we determine the required power for each heater from the tuning curves and apply the corresponding current to each heater. We also note that the resistances of the heaters remained fairly constant over the full FSR tuning range, with the measured values of $91.7 \pm 0.9 \Omega$ for heater 1 and $105.1 \pm 0.9 \Omega$ for heater 2. To determine the wavelength tuning accuracy and filter spectral characteristics at arbitrary wavelengths, we tuned the device to six randomly chosen wavelengths in the 1531– 1539 nm range. Fig. 3.6 shows the filter spectra obtained, which are very close to the optimized filter shapes, with the minimum and maximum ripples of 0.58 dB and 0.74 dB, respectively. The standard deviation in the center wavelength detuning is ± 22 pm, with the minimum and maximum deviations of 4 pm and 37 pm, respectively. These wavelength deviations are consistent with our estimated tuning

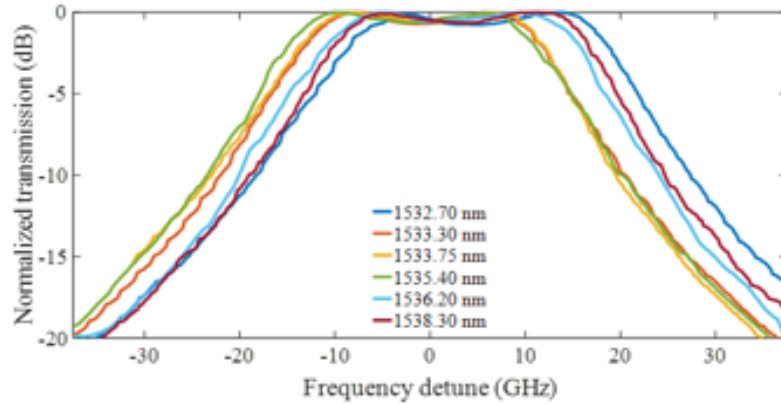


Figure 3.6: Tuned filter spectra at six arbitrarily chosen center wavelengths, with minimum and maximum ripples of 0.58 dB and 0.74 dB, respectively, and standard deviations in the center wavelength detuning of ± 22 pm.

wavelength accuracy of ± 27 pm. These results demonstrate that the filter can be continuously tuned with good wavelength accuracy and spectral performance over the FSR of the device.

3.1.4 Performance of Thermistors for Temperature Tracking

To evaluate the performance of the thermistors, we first obtained the response of each individual thermistor to heating power from each heater. Fig. 3.7 (a) and (b) plot the changes in the thermistor resistance due to same-ring heating and thermal crosstalk as functions of the power in heaters 1 and 2, respectively. We observe strong linear correlations between the thermistor resistance and the heater powers, which validate the effectiveness of the thermistor in tracking both the same-ring heating effect and thermal crosstalk. In particular, we found that thermal crosstalk contributes to about 34% of the total resistance change compared to same-ring heating.

To determine the actual temperatures sensed by the thermistors, we calibrated these resistance by heating the entire chip on a hot plate and measured the change in the thermistor resistance as a function of the temperature. Fig. 3.8 shows the change in the resistance of the thermistor arc segment surrounding each microring as a function of the known temperature. By fitting the data with the linear relation $\Delta R = \alpha \Delta T$, we extracted the thermal coefficient α of the thermistor to be 10.35 m Ω /K for thermistor 1 and 8.923 m Ω /K for thermistor 2. These values were then used to determine the temperature of the thermistors at different heater powers. Specifically, suppose the heater powers required to tune the filter to a particular wavelength are P_1 and P_2 , the total resistance changes of the thermistors are given by:

$$\Delta R_1 = r_{11}P_1 + r_{12}P_2 \quad (3.5)$$

$$\Delta R_2 = r_{21}P_1 + r_{22}P_2 \quad (3.6)$$

where $r_{11} = 3.415$, $r_{12} = 1.404$, $r_{21} = 1.183$, $r_{22} = 2.793$, all in units of m Ω /mW. The temperature changes sensed by the thermistors are then calculated from $\Delta T_1 = \Delta R_1/\alpha_1$ and $\Delta T_2 = \Delta R_2/\alpha_2$.

Fig. 3.9 plots the total changes in the thermistor resistance and the corresponding temperature changes as functions of the filter center wavelength. We again observe

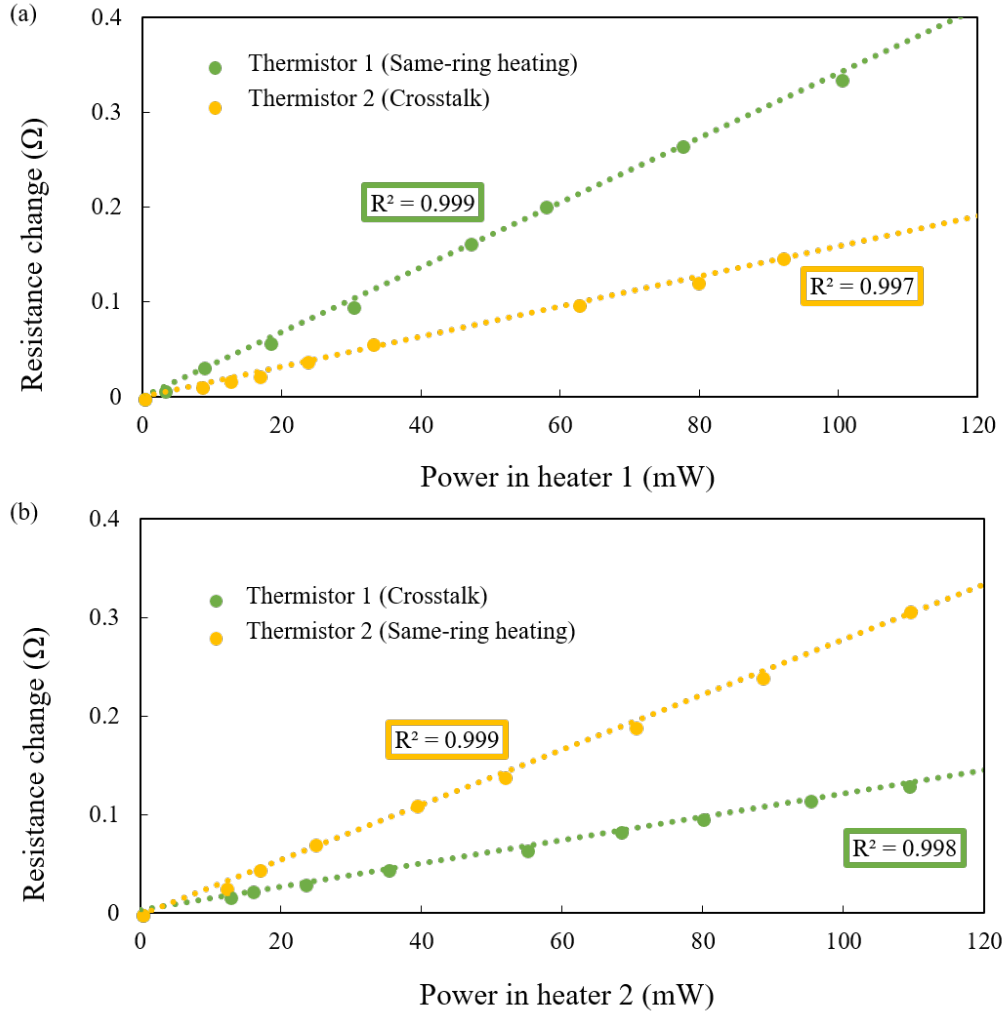


Figure 3.7: Changes in the thermistor resistances due to same-ring heating and thermal crosstalk as functions of the power in (a) heater 1 and (b) heater 2.

strong linear relationships between the thermistor resistances and the tuned wavelength. These relationships allows us to predict the expected thermistor resistance values and the corresponding temperature changes of the microrings at any center wavelength. in particular, from our simulation, we found that the maximum temperature change in the microring is 2.8 times as that in the thermistor due to the closer proximity of the microring to the heater. Thus, over the entire FSR tuning range, we can expect the temperatures of the microring to rise by about 120 °C. We can also estimate the precision of the thermistors in sensing the temperatures by computing the standard deviation between the data points in Fig. 3.9 and the best fit curves.

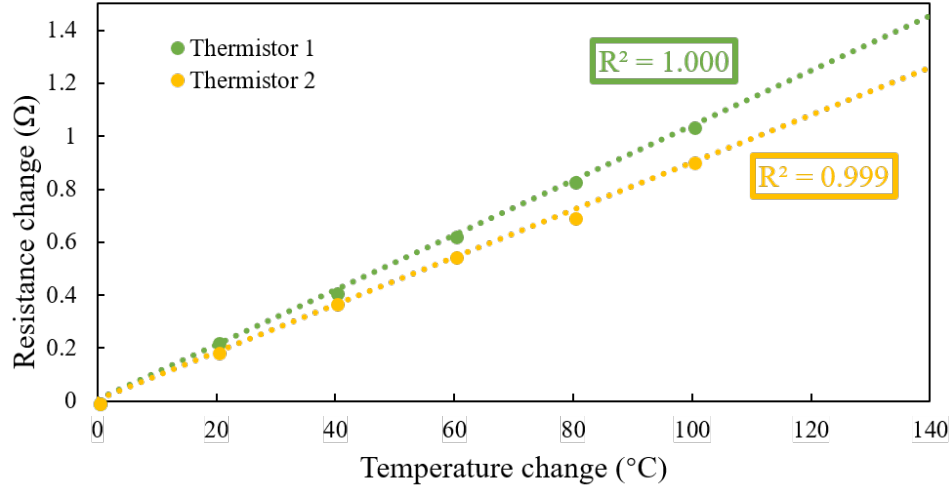


Figure 3.8: Change in the thermistor resistance as a function of the thermistor temperature.

We obtain a value of ± 0.1 °C for both thermistors, which translates to a center wavelength tracking resolution of ± 20 pm. This precision is adequate for tracking the center wavelength variations of the DMR filter, given that the tuning accuracy (resolution) of the ± 27 pm.

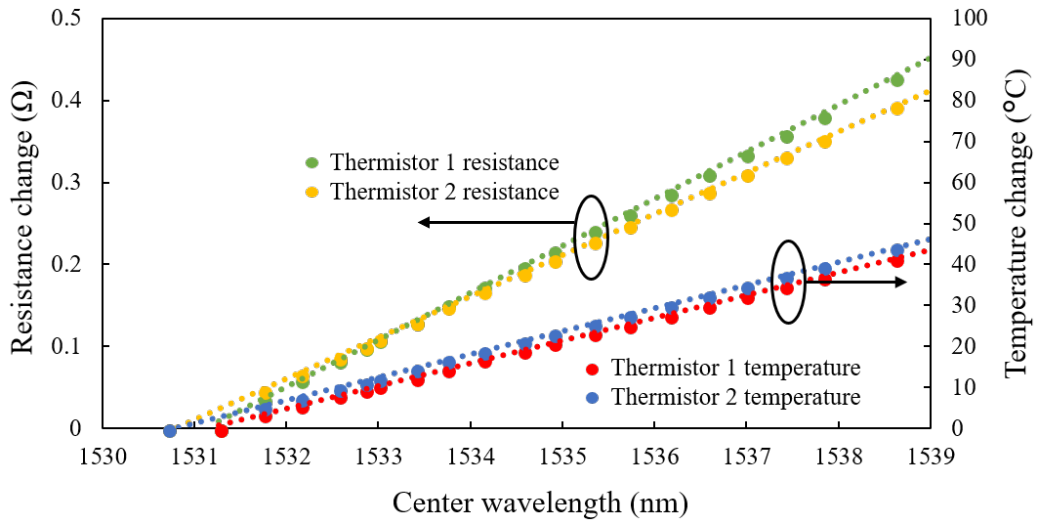


Figure 3.9: Changes in the thermistor resistances and the corresponding thermistor temperatures as functions of the filter center wavelength.

3.2 A Vernier Cascaded Microring Filter

3.2.1 Design and Implementation of VCMR Filter

In this section, we demonstrate the use of the Vernier effect to expand the effective tuning range of a filter by cascading two DMR filter stages of slightly different FSRs. Fig. 3.10(a) shows a schematic of a 4th-order VCMR filter, which is designed to have a tuning range of 32 nm over the optical C-band. Each DMR filter stage is designed to have a flat-top passband with a 3-dB bandwidth of 33 GHz, so that the cascaded spectrum will have a bandwidth of 25 GHz. To achieve this 2nd-order Butterworth filter response, the bus-to-ring and ring-to-ring coupling coefficients of both DMR stages are chosen to be $\kappa_1 = 0.38$ and $\kappa_2 = 0.07$. The filter tuning range is defined by the effective FSR of the VCMR, which is achieved by requiring the FSRs of the two stages to satisfy $N_1 \times FSR_1 = N_2 \times FSR_2 = 32$ nm. Choosing $N_1 = 4$ and $N_2 = 5$, we obtain the corresponding FSRs of the two DMR stages to be $FSR_1 = 8$ nm and $FSR_2 = 6.4$ nm. Figs. 3.11(a) and (b) show the simulated spectra of each stage, $H_1(\lambda)$ and $H_2(\lambda)$, and the cascaded filter response, $H_{VCMR}(\lambda) = H_1(\lambda)H_2(\lambda)$. The plots show that the VCMR filter has a cascaded bandwidth of 25 GHz for an effective FSR of 32 nm with spurious peaks remaining below -40 dB over its entire FSR.

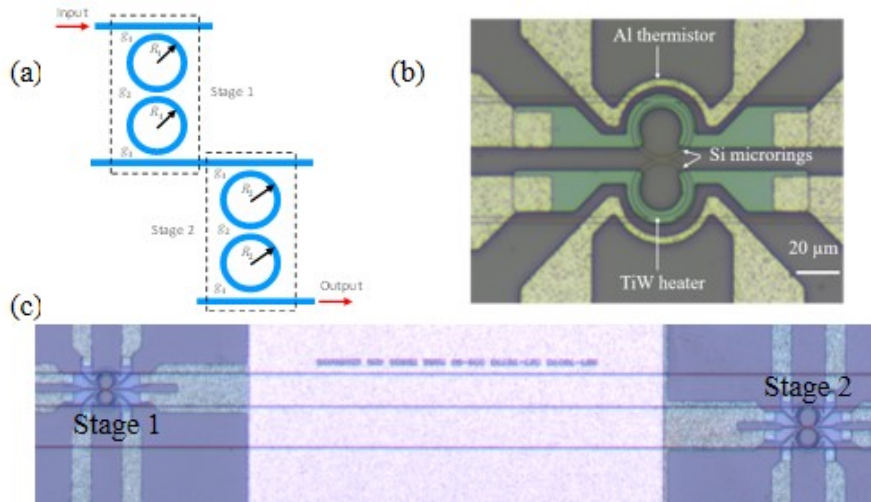


Figure 3.10: (a) Schematic of a 4th-order Vernier cascaded microring filter. Optical microscope images of (b) the first DMR filter stage and (c) the entire cascaded filter.

We implemented the VCMR filter on an SOI substrate with a 220 nm thick silicon layer on a 2 μm thick buffer oxide layer. The silicon waveguides had a nominal width of 450 nm for TE-mode operation and an oxide overcladding of 2 μm thickness. To obtain $FSR_1 = 8$ nm and $FSR_2 = 6.4$ nm, the microring radii of the two stages are set at $R_1 = 11.27$ μm and $R_2 = 14.13$ μm , respectively. The bus-to-ring and ring-to-ring coupling gaps of each stage were set to be $g_1 = 125$ nm and $g_2 = 300$ nm.

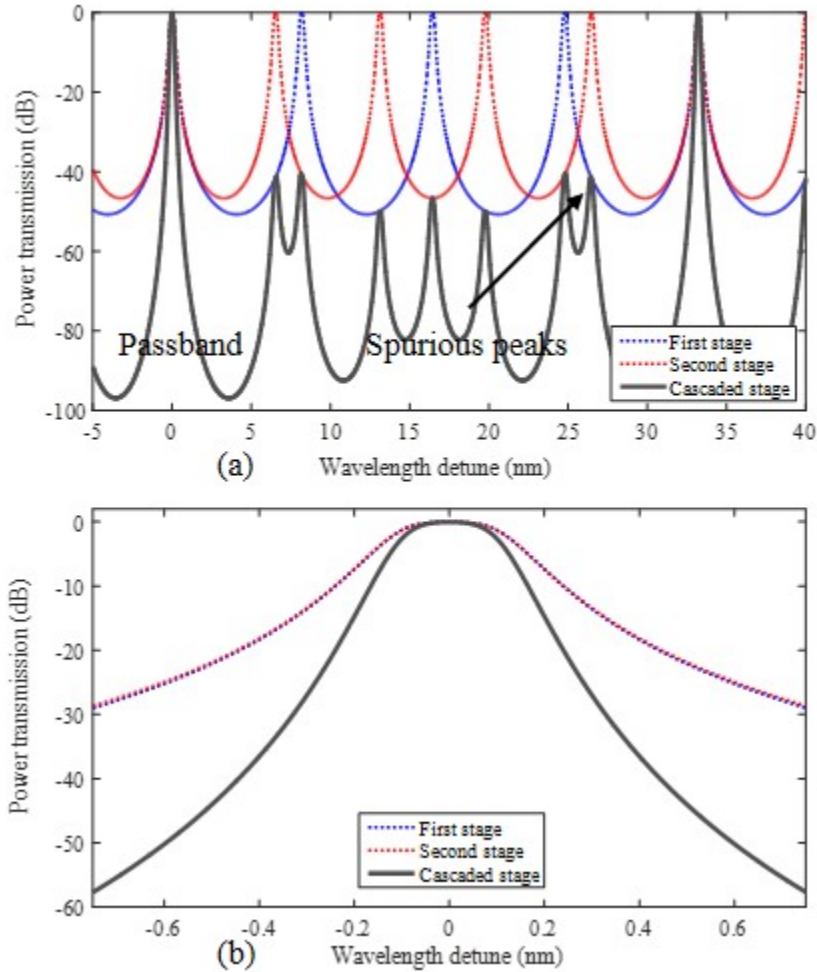


Figure 3.11: (a) Spectral responses of individual DMR filter stages and cascaded filter with overlapping passbands centered at zero wavelength detune. (b) Close-up view of passbands of DMR stages and cascaded filter.

The heaters and thermistors are designed in the same way to the DMR filters reported in the last section. The average resistance of the heaters is measured to

be 108Ω in the first stage and 125Ω in the second stage. Thermistors made of Al were also placed around the heaters, with an average resistance of 6.5Ω in the first stage and 6.8Ω in the second stage, respectively. In the tuning operation of the VCMR filter, the two stages can be heated to very different temperatures, depending on the set wavelength. To minimize thermal crosstalk between the two DMR filters, the two stages were separated by $600 \mu\text{m}$. The device was fabricated using Applied Nanotools' NanoSOI process. Figs. 3.10(b) and 3.10(c) show optical microscope images of a fabricated DMR filter stage and the cascaded filter.

3.2.2 Calibration and Tuning of DMR Filter Stages

We first calibrated each filter stage by adjusting the currents through the heaters to optimize the spectral response of the DMR filter to obtain flat-top passband with minimum ripple. The calibration process is similar to the process described in Section 3.2.3 except here we employed a dual-wavelength optimization method, which provides more symmetric filter response with smaller in-band ripple and more accurate center wavelength than previous methods employing just one wavelength [61]. The method requires two laser sources with the wavelengths set to approximately coincide with the 3-dB wavelengths on the left and right sides of the filter spectrum. The average of the two wavelengths then defines the center wavelength of the passband. By scanning the heater powers to maximize the total transmitted power at the two wavelengths, the optimized spectral response of the filter could be obtained. The method works best when the two wavelengths are set close to the 3-dB points of the passband where the total transmitted power is the most sensitive to heater powers.

To demonstrate the optimization procedure, we show in Fig. 3.12(a) the unoptimized filter response (yellow curve) of the first DMR stage around the 1558 nm wavelength. In the dual-wavelength optimization, we set the wavelengths of the two lasers to 1558.37 nm and 1558.63 nm, which correspond to a center wavelength of 1558.50 nm and an estimated 3-dB bandwidth of 0.26 nm or 33 GHz. The optimized

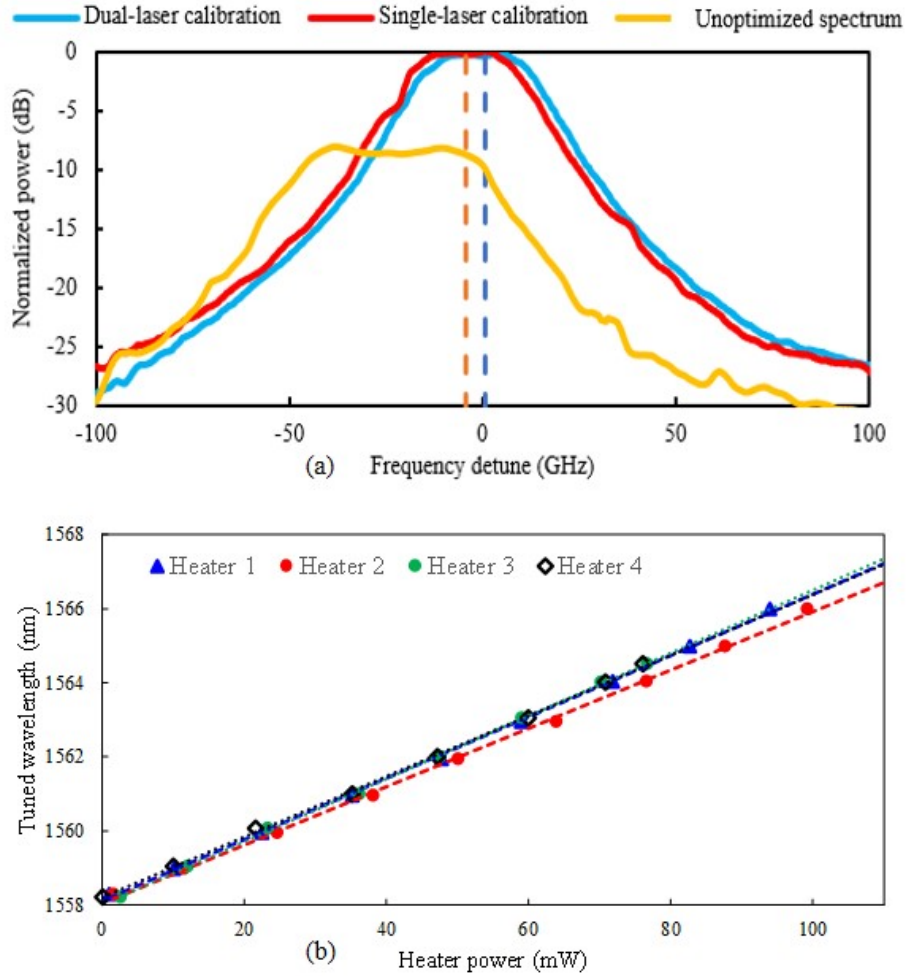


Figure 3.12: (a) Unoptimized spectrum (yellow) of the first DMR filter stage and optimized spectra obtained using the dual-wavelength (blue) and single-wavelength (red) optimization methods. The dashed lines indicate the center wavelength of the respective spectrum. (b) Tuning curves for Heaters 1 & 2 in Stage 1 and Heaters 3 & 4 in Stage 2 of the VCMR filter.

spectrum is shown by the blue curve in the plot, which shows a flat-top passband with a ripple of 0.17 dB and center wavelength detuned from the target wavelength by 7 pm. For comparison, we also performed the spectrum optimization using only a single laser set at the target center wavelength of 1558.50 nm. The spectrum obtained is shown by the red curve in Fig. 3.12(a), which has a slightly worse ripple of 0.20 dB, and much larger center wavelength detune of 33 pm. In general, we found that dual-wavelength optimization yields more symmetric and flatter spectral response than the

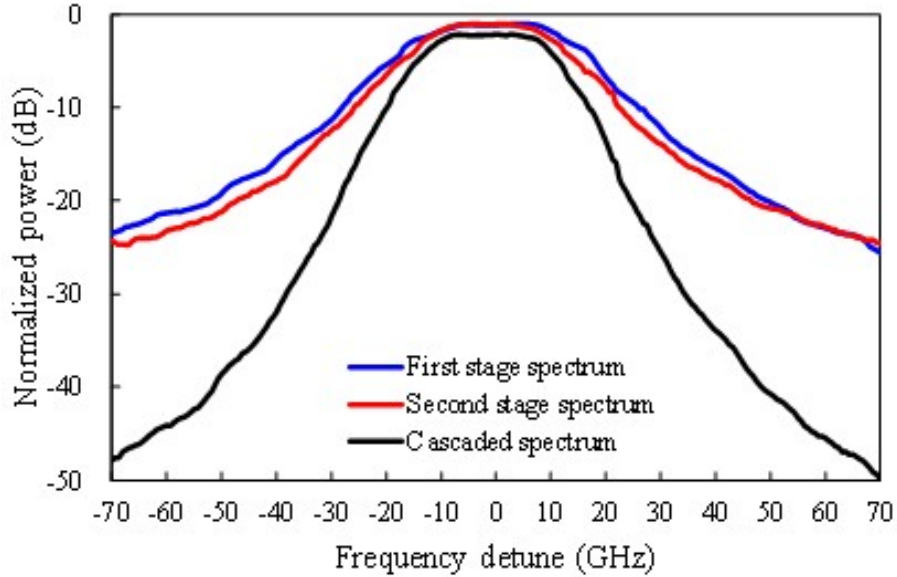


Figure 3.13: Passband characteristics of individual DMR filter stages and of the 4th-order VCMR filter at 1577.5 nm center wavelength.

single-wavelength method, especially for filters with large ripples in the passband.

We repeated the above calibration and optimization process for various center wavelengths across the FSR of each DMR stage to generate a tuning curve for that stage. Fig. 3.12(b) plots the relationships between the center wavelength of the optimized spectrum of each stage and the powers applied to the heaters to tune to that wavelength. The strong linear correlations between the heater powers and center wavelength allow each filter stage to be accurately tuned to any arbitrary wavelength within its FSR. From the plots, we determine the average tuning rates be 80.6 pm/mW for stage 1 and 83.4 pm/mW for stage 2.

3.2.3 Performance of VCMR filter

In the operation of the VCMR filter, given a desired center wavelength of the passband, we use the tuning curves in Fig. 3.12(b) to determine the required power for each heater to tune the filter stages to the desired wavelength. As an example, Fig. 3.13 shows the spectral responses of the individual DMR stages and the composite

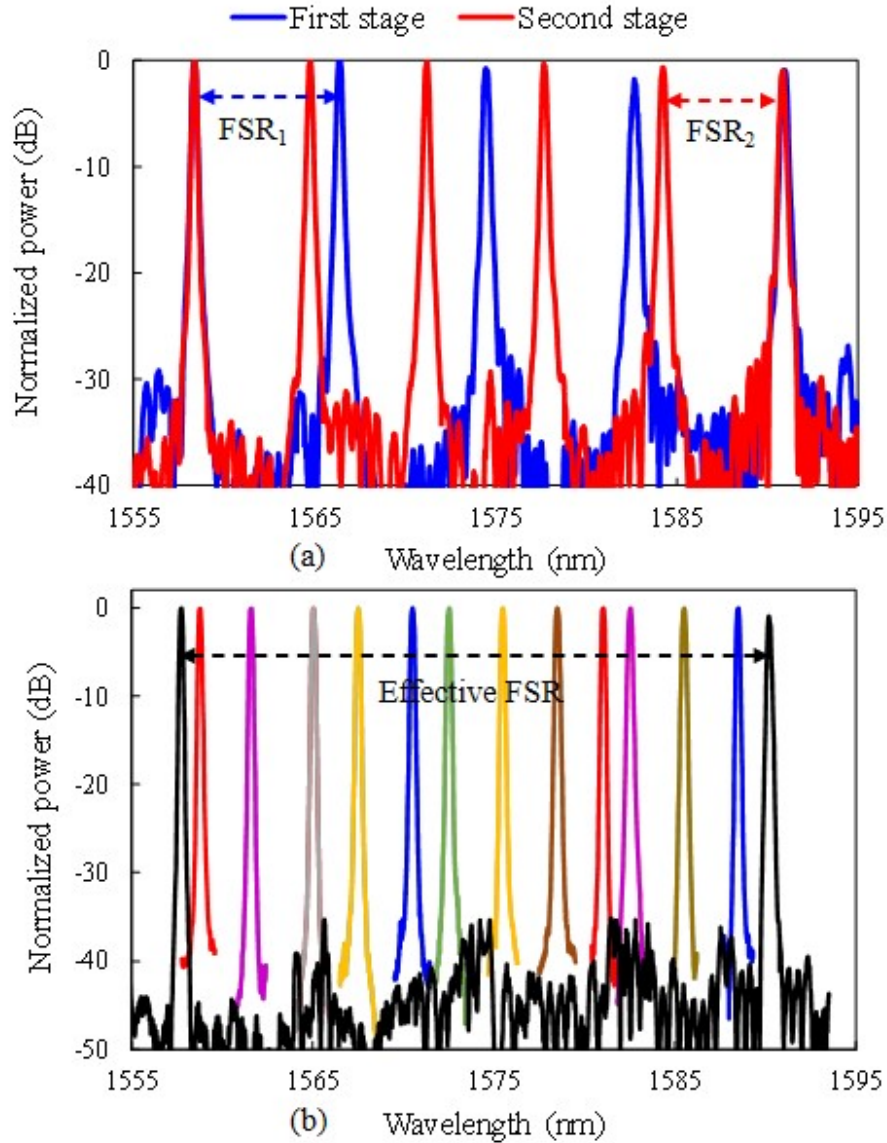


Figure 3.14: Measured spectra of (a) individual DMR stages and (b) cascaded filter. Plots in (b) show the filter spectrum tuned to various wavelengths across the 32.1 nm effective FSR of the VCMR filter.

spectrum of the cascaded filter tuned to 1577.5 nm wavelength. Each DMR filter stage has a 3-dB passband of 33.75 GHz, yielding a cascaded flat-top passband of 23.8 GHz, which is slightly smaller than the designed 25 GHz. The cascaded spectrum also shows sharp roll-offs characteristic of a 4th-order filter response, providing 40 dB isolation at ± 50 GHz from the center frequency. The insertion loss was 1.05 dB for each DMR stage and 2.1 dB for the VCMR filter.

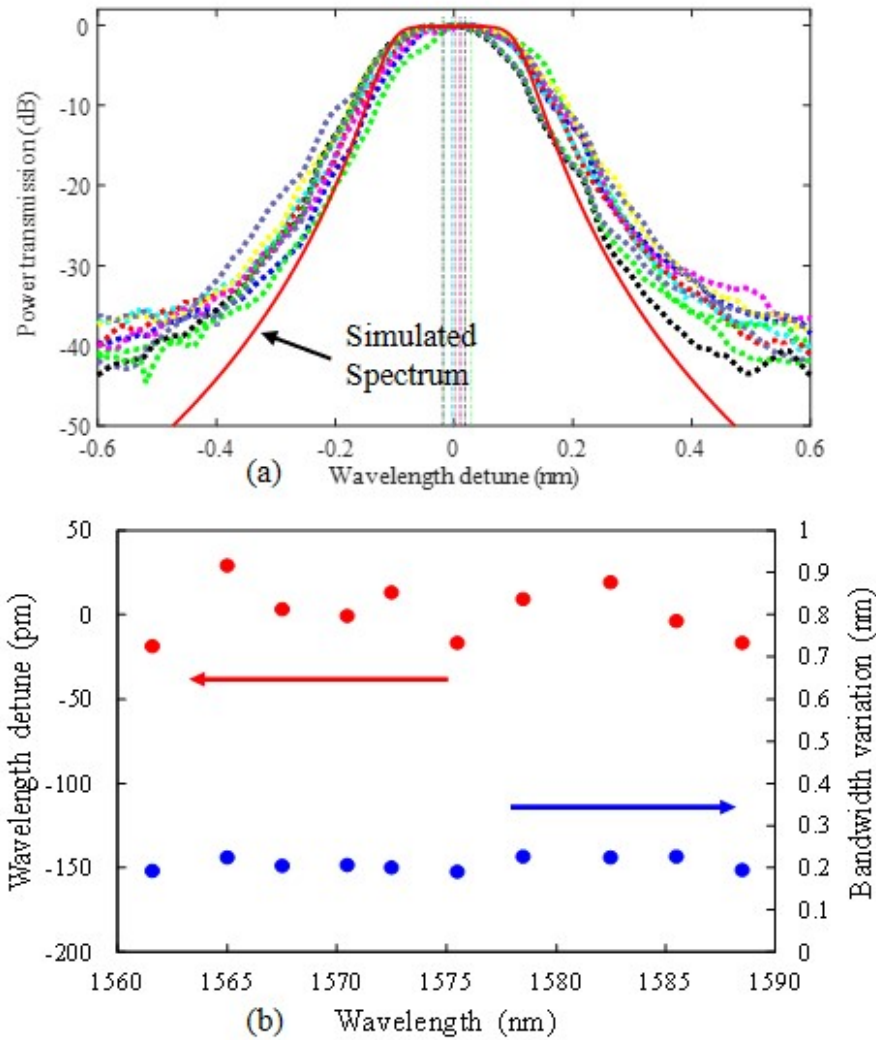


Figure 3.15: (a) Plot of VCMR filter spectra tuned to various different center wavelengths across its FSR. The dotted vertical lines near the center indicate the center wavelengths of the tuned spectra. (b) Plots of variations in the center wavelength detune (red dots) and 3 dB bandwidth (blue dots) of VCMR filter spectra tuned to different center wavelengths.

Figs. 3.14(a) and (b) show the spectral scans of the DMR stages and cascaded filter over 40 nm wavelength range. The FSRs of the two stages are 7.8 nm and 6.4 nm, which are close to the designed values. The cascaded spectrum has an effective FSR of 32.1 nm, with out-of-band rejection level of at least -35 dB. In Fig. 3.14(b) we also show the spectral responses of the VCMR filter tuned to various center wavelengths, demonstrating that the filter can be tuned across its 32-nm FSR.

In Fig. 3.15(a) we plot the spectral responses of the VCMR filter tuned to various wavelengths as functions of the detuning from the set wavelengths. The deviations in the tuned filter center wavelength from the set wavelength are also plotted in Fig. 3.15(b) along with the 3 dB bandwidths. We find that the average 3 dB bandwidth is 0.208 nm (or 26 GHz) with a standard deviation of ± 13.6 pm. The average wavelength detuning is 2.3 pm (0.3 GHz) from the target wavelength. The wavelength tuning accuracy, as given by the standard deviation in the center wavelength detuning, is ± 14.9 pm (or ± 1.86 GHz). We note that this tuning accuracy, which is achieved over the entire 32 nm tuning range, is better than both previously reported silicon microring filters [61] and some commercial tunable filters [70]. The main factor which limits the wavelength tuning accuracy is the uncertainty in controlling the heater current, which results in an uncertainty of ± 0.1 mW in the heater power. This uncertainty affects both the accuracy of the tuning curves used to calculate the heater powers required to tune the filter to the desired center wavelength, as well as the accuracy in setting these powers. A second, less significant source of tuning uncertainty is the fluctuation in the ambient temperature of the chip. For the detailed optimization procedure such as how we optimized heater current change, and the optimized optical power, we have attached the plots of each heater current sweep in Appendix I at the end of the thesis.

3.3 Summary

In this chapter, we first demonstrated continuous tuning of a silicon DMR filter over the full 7.8-nm FSR of the resonators, achieving a tuning wavelength accuracy of ± 27 pm. We also performed rigorous analysis to quantify the effects of thermal crosstalk on the device tuning characteristics. We demonstrated the feasibility of using on-chip thermistors to monitor the temperature stability of the microrings, achieving a temperature precision of ± 0.1 °C and a corresponding wavelength tracking accuracy

of ± 20 pm. We then cascaded two DMR filter stages with different FSRs to form a VCMR with a broad wavelength tuning range of 32.7 nm. The cascaded spectral responses also exhibit sharp skirt roll-off and out-of-band rejection level better than 35 dB over the full tuning range, thus providing better adjacent channel isolation for wavelength multiplexing/demultiplexing applications. We noted that filter spectral roll-off can be further sharpened by direct coupling 4 MRs to form a directly-coupled Vernier microring (DC-VMR) filter. In the next chapter, we will introduce a DC-VMR filter as a part of the fast wavelength selection circuit.

Chapter 4

Fast Wavelength Selector for High-Speed Optical Networks

Communication networks are experiencing rapid development toward high speed, high capacity, and low latency [71]. As a key platform for cloud computing and other emerging web applications, data centers (DCs) are facing tremendous challenges to meet the demand for increased transmission bandwidth and reduced end-to-end latency. Since data transmission configurations (e.g., routing path and wavelength channel) are usually fixed regardless of user dynamics (e.g., large and continuous flow and discrete small packets), conventional inter-DC data transfers suffer from both low wavelength resource utilization and heavy congestion [72]. Recently, optical network architectures based on flexible traffic scheduling methods, traffic monitoring and wavelength reconfiguration have been shown to mitigate traffic congestion and avoid massive cache employment [73][74][75][76].

A major feature distinguishing reconfigurable optical networks is whether they are based on circuit or packet switching. Circuit-based schemes mainly target DC networks (DCNs) in which long-term large and continuous data transfers are considered. For this reason, they are usually based on micro-electro-mechanical systems (MEMS) for large port counts, which have long reconfiguration times (in the orders of a few milliseconds). This delay is the period during which data packets cannot be transmitted and need to be held in cache, which increases traffic flow congestion. On the

other hand, packet-based optical networks fit better in bursty traffics, which rely on the fast path routing and wavelength setting[77]. Such a fast wavelength routing demand motivates the development of fast wavelength selectors (WS), which can pick a single wavelength out from a wavelength comb source to a specific port for data transmission [78].

Recently, an InP WS circuit using arrayed waveguide gratings (AWGs) and semiconductor optical amplifiers (SOAs) was demonstrated in [78], which could provide wavelength selection from a fixed wavelength comb in a few nanoseconds. Aalto et al. [79] also reported an integrated WS circuit using the AWGs-SOAs configuration on SOI with nanosecond selection time. Since AWGs have a fixed number of output channels at predetermined wavelengths, these WS circuits are not easily scalable and reconfigurable for various channel grid configurations. They also have large footprints; for example, the WSs reported in [78][79] occupied a chip area of $8\text{mm} \times 6\text{mm}$ but could accommodate only 19 wavelengths. In addition, the AWGs-SOAs design is not a fully integrated solution since the SOAs and AWGs must be realized on different materials platforms and need to be aligned and chip-bonded, which could result in excessive loss and lower yield and less reliability [79][80].

In this chapter, we propose and demonstrate a fast and compact WS circuit monolithically integrated on an SOI chip. As demonstrated in the previous chapter, broadband wavelength tuning can be achieved in silicon photonic MRR filters using the thermo-optic effect, especially when combined with the Vernier scheme. However, due to its slow response time, thermal tuning cannot perform fast wavelength switching in the sub-microsecond time scale, which is required in optical networks for low latency. Faster tuning can be achieved using free carrier (FC) injection in pn junctions, which are widely used for switching and modulation [81][82]. However, since the refractive index change due to FC dispersion (FCD) is small($\sim 10^{-3}$ for carrier injection and $\sim 10^{-4}$ for carrier depletion) [83][84][85][86] compared to the thermo-optic effect, only a limited wavelength tuning range can be achieved using the FC dispersion effect. To

overcome the shortcomings of both thermo-optic effect and FCD, we combine the broadband tunability of thermo-optic VMR filters with the fast switching capability of *pin*-junction Mach-Zehnder switch (MZS) to achieve fast and broadband wavelength selection over a 32 nm bandwidth. Under best-case operating conditions, our WS circuit can reduce the wavelength selection time from tens of μs to a few *ns*. Such a WS circuit could provide a cost-effective solution for fast wavelength selection in high-speed optical networks.

The rest of this chapter is organized as follows. Section 4.1 presents the design and fabrication of the fast WS circuit. As the first part of the WS circuit, we will characterize the 4th DC-VMR filter for broadband tunability in Section 4.2. This will be followed by an investigation of the *pin* MZS performance in Section 4.3. In Section 4.4, we demonstrate the wavelength selection operation of the WS circuit. The chapter is summarized in Section 4.5.

4.1 Fast Wavelength Selector Circuit Architecture

Fig. 4.1(a) shows a schematic diagram of the WS circuit architecture. At the input of the circuit, a 3dB coupler is used to split a comb of input wavelengths into two equal streams. A thermo-optical tunable MRR filter is used to drop a wavelength of interest from each stream, the pair of dropped wavelengths are then fed to a fast *pin* MZS, which is used to switch the selected wavelength to the output port (port 1 or 2). In the operation of the WS circuit, supposed that the MZS is initially set to select the dropped wavelength (λ_1) from the top MRR filter to Drop port 1. This leaves the bottom MRR filter free to be tuned to the next target wavelength (λ_2). When the bottom MRR filter is pretuned to λ_2 , the MZS can be switched to select this wavelength when needed. This wavelength switching time is only limited by the *pin* junction response time. In this way, we can overcome the slow thermal tuning time of the MRR filter and reduce the effective wavelength selection time to nanoseconds.

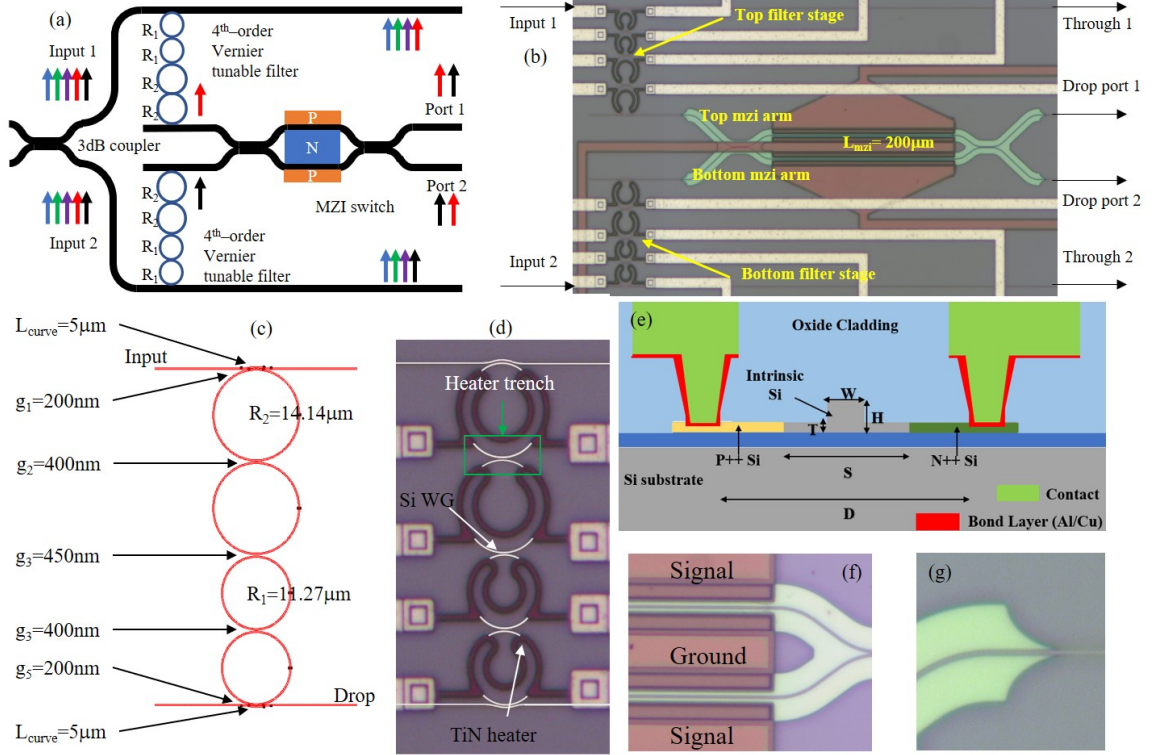


Figure 4.1: (a) Schematic diagram of the wavelength selector circuit and (b) microscope image of fabricated circuit. (c) Schematic of the DC-VMR filter and (d) image of a fabricated device. (e) Cross-sectional view of a waveguide arm of the Mach-Zehnder switch showing the embedded *pin* junction. (f) and (g) Close-up images of the *pin* junction waveguide of the MZS and the taper transition between the slab *pin* waveguide and passive strip waveguide.

In the implementation of the WS circuit, we develop the directly coupled Vernier microring (DC-VMR) filter configuration (to be characterized in section 4.3). A schematic of the DC-VMR filter is shown in Fig. 4.1(c), in which the radii of the first two microrings are slightly different from the radii of the last two microrings to achieve the Vernier effect. To compare the performance of the VCMR filter to a DC-VMR filter, we plot in Figs. 4.2(a) and (b) the passband response and whole spectral response of a 4th order VCMR and 4th DC-VMR filter designed for the 3-dB bandwidth of 25 GHz and FSR of 32 nm. From the plots we see that the DC-VMR filter has a sharper skirt roll-off (e.g., an extra 17 dB drop-off at 50 GHz) and higher out-of-band rejection (e.g., an extra 8 dB of spurious peak suppression over the full

FSR) than the VCMR filter. A disadvantage of the DC-VMR, however, is that it suffers from larger thermal crosstalk due to the proximity of all four microrings thus the filter optimization and tuning processes are more challenging. We designed the

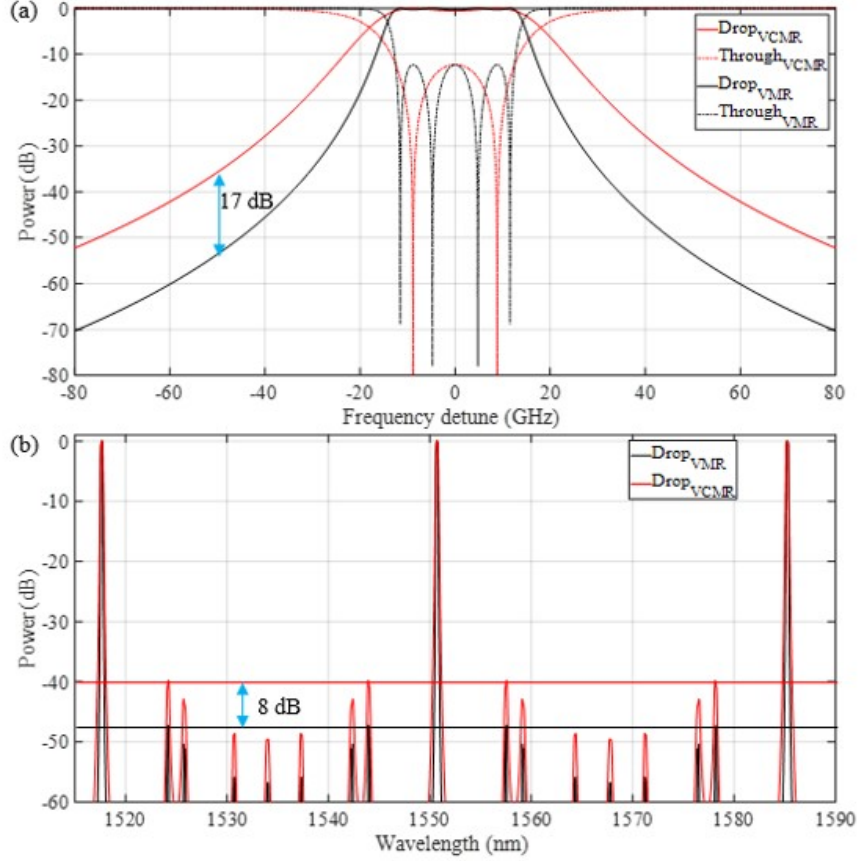


Figure 4.2: Comparison of simulated spectral responses of 4th-order VCMR filter and DC-VMR filter with the same bandwidth: (a) passband response, and (b) response over full FSR.

DC-VMR filter to have a 3-dB bandwidth of 25 GHz, 32 nm FSR and 45 dB out-of-band rejection for the TE polarization. The device was fabricated using the Advanced Micro Foundry [87] on an SOI chip consisting of a 220-nm thick Si layer laying on a 3- μm thick SiO₂ overladding layer. The silicon waveguides had a nominal width of 500nm. The coupling gaps were $g_1 = g_5 = 200\text{nm}$, $g_2 = g_3 = 400\text{nm}$, and $g_4 = 450\text{nm}$, corresponds to coupling coefficients of $\kappa_1 = \kappa_5 = 0.40$, $\kappa_2 = \kappa_4 = 0.08$, and $\kappa_3 = 0.04$. The microring radii are 11.27 μm for the first two microrings and

14.14 μm for the last two microrings. At the input and output ports of the filter, the bus waveguides were tapered down to a tip width of 200 nm to achieve efficient light coupling via lensed fibers.

To optimize the spectral response and tune the DC-VMR filter, we used microheaters made of TiN with 120 nm thickness, 2 μm width, placed 2 μm above the silicon waveguides. As depicted in Fig. 4.1(d), the heater is folded over each half of the microring (with a minimum bending radius of 2.5 μm) to increase the effective length and thus enhance the tuning efficiency. The nominal heater resistance is $120 \pm 1.3 \Omega$. Heater trenches in the oxide cladding were also designed near the coupling junctions to reduce thermal crosstalk between the microrings. To achieve fast and efficient switching, we used an MZS with both arms embedded with 200 μm -long *pin* junctions operated in the carrier injection mode. Fig. 4.1(e) shows a cross-section of an MZS arm showing a *pin* junction embedded in the SOI rib waveguide. The rib waveguide is designed for TE polarization and has thickness $H = 220$ nm, rib width $W = 500$ nm, and slab thickness $T = 90$ nm. The doping levels are $2 \times 10^{20} \text{cm}^{-3}$ for the p^+ region and $5 \times 10^{20} \text{cm}^{-3}$ for the n^+ region. The doping process flow uses phosphorus and boron implantation to form the n and p regions. The intrinsic region width S is set at 1.7 μm to minimize FC absorption (FCA) in the waveguide core. The electrical contacts are separated by $D = 4 \mu\text{m}$ to avoid the inference of optical mode, a top view image of the location of *pin* junction waveguides in carrier injection mode to waveguides is shown in Fig. 4.1(f). A 15 μm slab waveguide taper is used to reduce the mode propagation loss from the strip waveguides of the VCM filter and the rib waveguides of the MZS, a close-up image of the slab waveguide taper is shown in Fig. 4.1(e). The process uses the deep ultraviolet (DUV) lithography to define the silicon device pattern. A microscope image of a fabricated WS circuit is shown in Fig. 4.1 (b), which occupies an area of $500 \mu\text{m} \times 700 \mu\text{m} = 0.35 \text{mm}^2$.

Fig. 4.3 shows the simulated spectra of the WS circuit. Suppose the upper filter and the bottom filter initially are tuned to wavelength $\lambda_1 = 1553$ nm and $\lambda_2 = 1550$

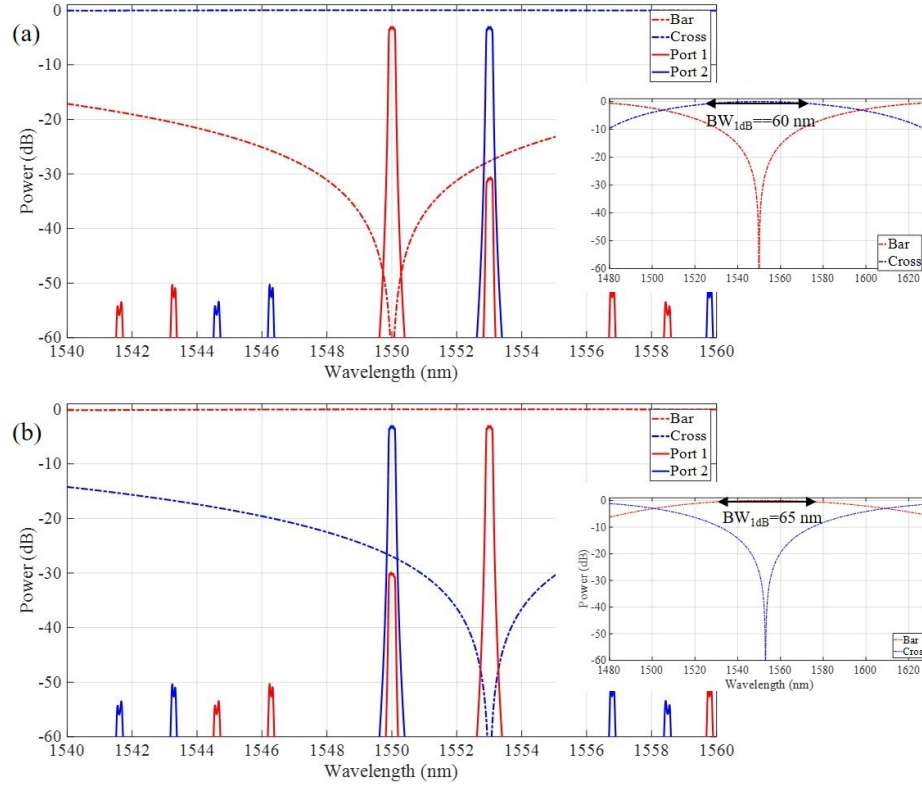


Figure 4.3: Output spectra of the WS circuit showing wavelength switching between $\lambda_1 = 1553\text{nm}$ from input port 1 and $\lambda_2 = 1550\text{nm}$ from input port 2: (a) when MZS is set in the “cross” state, and (b) when MZS is set in the “bar” state. In each figure, solid lines are the output port spectra of the WS circuit, the dash lines are the spectral responses of the MZS. Inset plots show the 1 dB bandwidth of the MZS spectra centered over the selected wavelength.

nm, respectively. The MZS initially is in the cross-state (e.g., turn on the cross path to transmit optical power but turn off bar path) so that λ_1 is transmitted to output port 2 of the MZS and λ_2 is transmitted to output port 1. As shown in Fig. 4.3(a). Since we set the maximally rejected wavelength in the bar-state spectrum at λ_2 , we can, in principle, kill the bar power entirely at this wavelength. Thus, the spectrum of the port 2 has an isolated peak at λ_1 with > 50 dB rejection on another wavelength. However, the port 1 spectrum has a ~ 30 dB side peak at the λ_2 , which is mainly caused by the less rejection of the bar-state at this wavelength. Similarly, suppose the WS circuit needs to select a new wavelength of λ_2 to output port 2. We can switch the MZS to the bar state (e.g., turn on the bar path to transmit optical power

but turn off the cross path). As shown in Fig. 4.3(b), by setting the maximally rejected wavelength in the cross-state spectrum at λ_1 , the spectrum of port 2 has an isolated peak at λ_2 with > 50 dB rejection on another wavelength. In principle, this wavelength selection process can be seamless (a few ns) if the bottom filter is pretuned to the target wavelength in advance, and we only need to switch the MZS. We plot inset each figure a bigger picture for the MZS spectra. From both insets, we see the 1-dB bandwidths are more than 60 nm centered at the maximally rejected wavelength. This wide bandwidth allows us to select the output wavelength from one filter with less than 1dB insertion loss while suppressing any undesired wavelength from the other filter within ± 30 nm apart from the selected wavelength.

4.2 Performance of 4th-order DC-VMR Filter

To characterize the performance of the DC-VMR filter, we first performed optimization of the filter spectrum by applying currents to the heaters to obtain a flat-top passband response at a target center wavelength. We employed both the single-wavelength method and the dual-wavelength method (described in Section 3.3.2) to optimize the filter passband. Fig. 4.4 shows the as-fabricated filter spectrum (black trace) and the optimized filter responses obtained by the single-wavelength method (red trace) and the dual-wavelength method (blue trace). For the single-wavelength method, the target wavelength was set to be 1555 nm which is also the center wavelength of the spectrum. For the dual-wavelength method, two wavelengths were set to be 0.2 nm (25 GHz) apart on each side of the center wavelength. From the spectra performance we note the optimized spectrum by dual-wavelength has 4.5 dB in-band ripple, which is still relatively large in comparison to the VCMR filter response, which was most likely caused by fabrication errors in the coupling gaps and could not be reduced by only adjusting the resonant frequencies of the microrings alone. Nonetheless, it is still much better than the optimized spectrum obtained from the single-wavelength

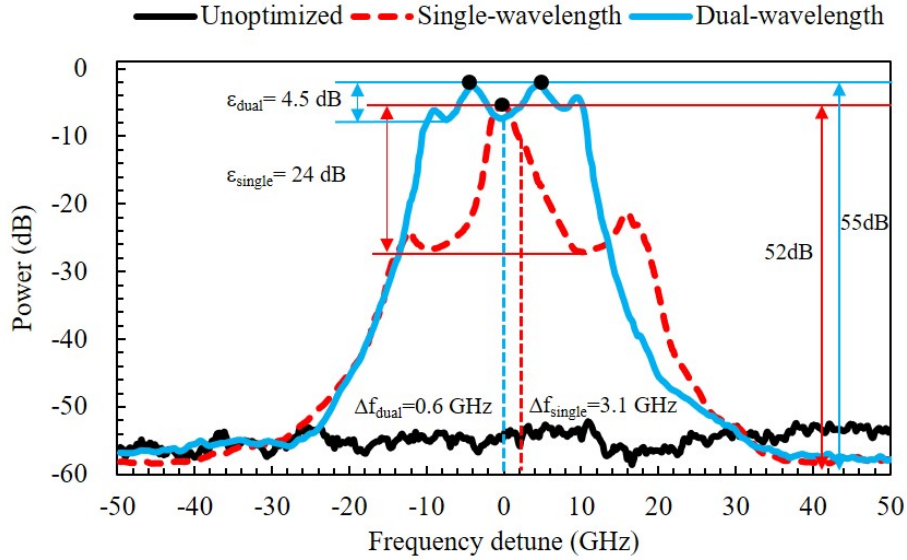


Figure 4.4: (a) Spectral optimization of the DC-VMR filter using the single-wavelength method (red trace) and the dual-wavelength method (blue trace).

method. The optimized spectrum has a 4.5 dB ripple bandwidth of 22 GHz and more than 55 dB out-of-band rejection. There is also a 2.9 dB extra insertion loss in the single-wavelength spectrum comparing to the dual-wavelength spectrum. We also determined the center wavelengths of the optimized filter spectra, which are taken to be the center wavelength of the 30-dB bandwidth. We obtained a center frequency detuning of 0.6 GHz for the dual-wavelength method and 3.1 GHz for the single-wavelength method. It can be seen that the dual-wavelength method outperforms the single-wavelength method in both center wavelength and bandwidth, especially when the optimized spectrum is still rippled. We attribute this difference between two methods to that the single-wavelength method could randomly recognize any of the local peaks as the center of the spectrum and converge the heater power control algorithm to this wavelength without evaluating the spectra performance at another wavelength. On the other hand, the dual-wavelength method needs to maximize the sum of side-band optical power, which does not rely on any local peaks.

Fig. 4.5(a) shows the filter spectra tuned to various wavelengths over the 32.7 nm effective FSR. We observe that the spurious peaks are suppressed below -46 dB over

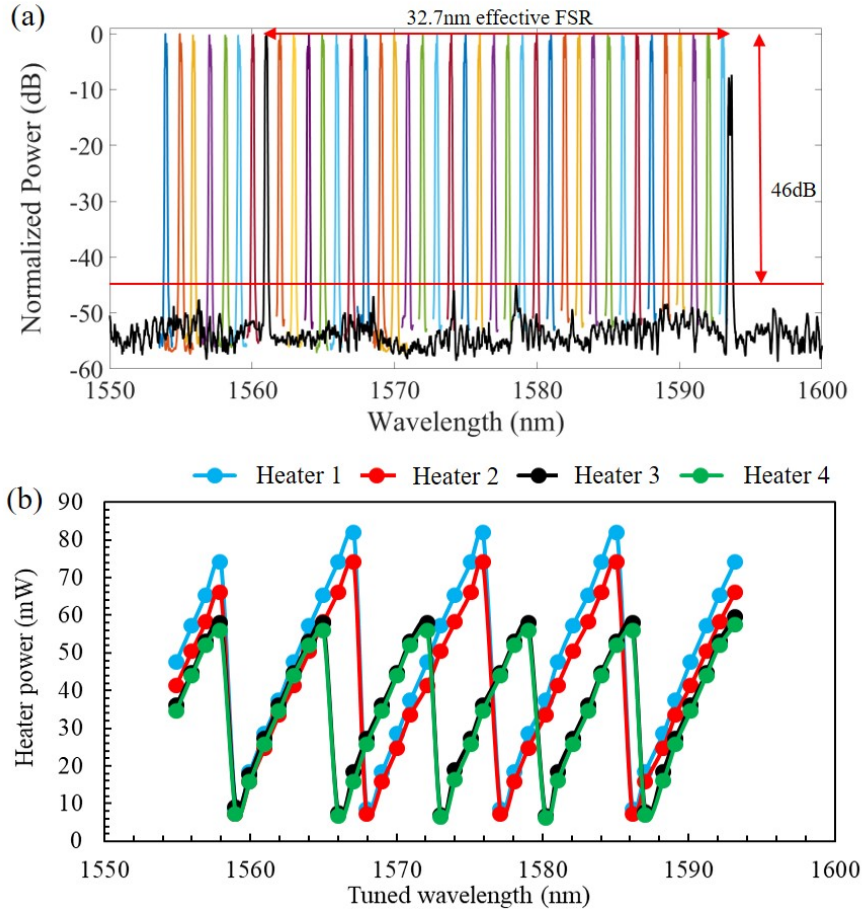


Figure 4.5: (a) Spectra of the DC-VMR filter tuned over the full 32.7 nm effective FSR (tuning range). (b) Thermal tuning curves of the 4 metal heaters over the tuning range in (a).

this wavelength range, which is ~ 10 dB comparing to VCMR reported in Chapter 3. The insertion loss remains relatively constant at 5.5 dB over the tuning range. Again, this value is higher than the insertion loss of the VCMR filter because of the large ripples in the passband of the DC-VMR filter caused by errors in the coupling coefficients-coupling gap implementation. Fig. 4.5(b) illustrates the powers required in 4 heaters to tune the DC-VMR filter to various wavelengths over the FSR. Again we observe that the power of each heater follows a fairly linear trend so that we can use these curves to tune the filter to an arbitrary wavelength by interpolating the tuning curves. The average tuning rate of the microrings is 115.3 pm/mW, which is about 40 % higher than the DMR and VCMR filters reported in previous works[88][89][90][82].

We attribute this improvement in the tuning efficiency to our folded heater design patterns. For the detailed optimization procedure, such as how we optimized heater current, and the optimized optical power, we have attached the plots of each heater current sweep in Appendix I at the end of the thesis.

4.3 Performance of *pin* MZS

MZSs are usually optimized to provide maximum extinction at some fixed center wavelength. In this case, the extinction bandwidth (e.g., 20 dB bandwidth) is limited by the dispersion of the differential phase between the two MZS arms. For our switch, since we can vary the phases of both arms of the MZS, we can dynamically tune the transmission spectra to provide maximum extinction at the selected wavelength. Fig. 4.6(a) shows the voltage responses at the two output ports of the MZS to bias voltage on the top arm. We observe that the device is initially in the bar state at 1558 nm wavelength, with a maximum extinction of 36 dB, as the spectra shown in Fig. 4.6(b). When we swept the bias current in the top arm of the MZS, the transmitted powers at the bar and cross ports at the 1558 nm wavelength follow the curves shown in Fig. 4.6(a). The device can be switched to the cross-state by applying 4.22 mA (at 1.06 V) to the top arm, as the spectra shown in Fig. 4.6(c), exhibiting a maximum extinction of 30 dB at 1558 nm. For both the bar port and cross port spectral responses, the measured 1-dB transmission bandwidth is more than 60 nm, which is fairly consistent with the simulation results.

In the operation of the WS circuit, since the two inputs to the MZS consists of only two narrow-linewidth wavelengths, we can effectively realize the broadband wavelength selection/suppression by tuning the minimum transmission of the MZS to the wavelength to be rejected. This can be achieved by varying the bias current to either the top arm or bottom arm. Figs. 4.7(a) and (b) show the transmission spectra at the cross port and bar port, respectively, of the switch for different bias current on

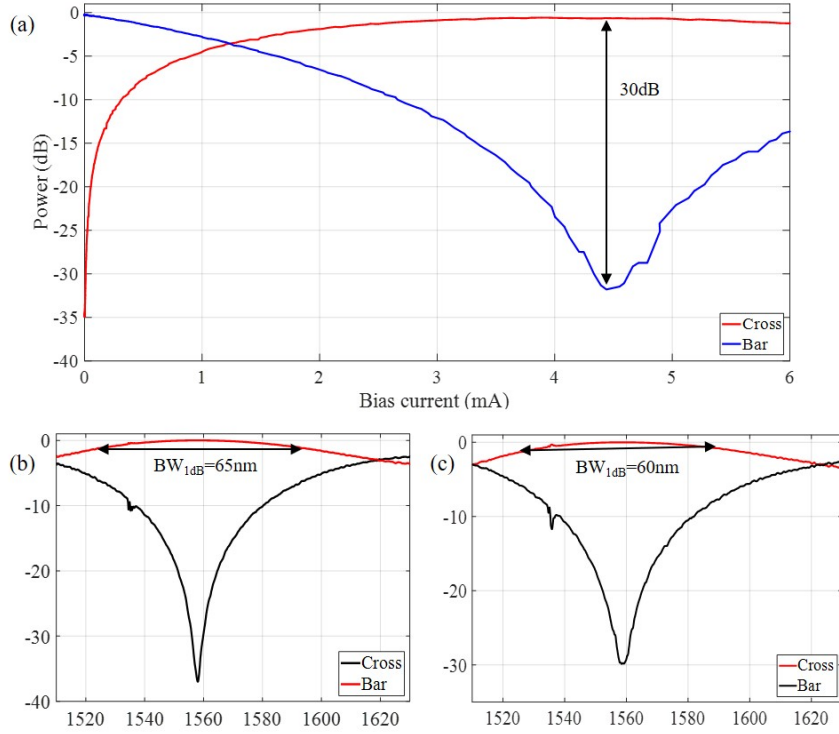


Figure 4.6: (a) DC voltage response of the MZS at 1558nm wavelength. (b) Measured spectra of the cross and bar states of MZS when bias current is 0 mA (c) Measured spectra of the cross and bar states of MZS when bias current is 4.22 mA .

the top and bottom arms. As seen in Fig. 4.7(a), the bar-state spectra is red-shifted when the bottom arm is biased and blue-shifted when the top arm is biased (here we show only the rejected port spectra to better illustrate the exact wavelengths with maximum extinction ratio). Due to the dispersion effect in input and output direction coupler, the extinction of the MZS spectra over the tuning range shows a varied transmission minimum dip. However, the extinction ratio is kept below 25 dB over the wavelength range 1505 - 1612 nm, yielding an effective 25-dB extinction bandwidth of more than 100 nm. For the cross-state spectra (where we only show "off" port spectra) in Fig. 4.7(b), we observe that the spectrum is blue-shifted with the increasing bias on the top arm and red-shifted with the increasing bias on the bottom arm. The maximum extinction ratio below -25 dB over the wavelength range 1520 - 1580 nm, yielding a smaller 25-dB rejection bandwidth of 60 nm. The unoptimized

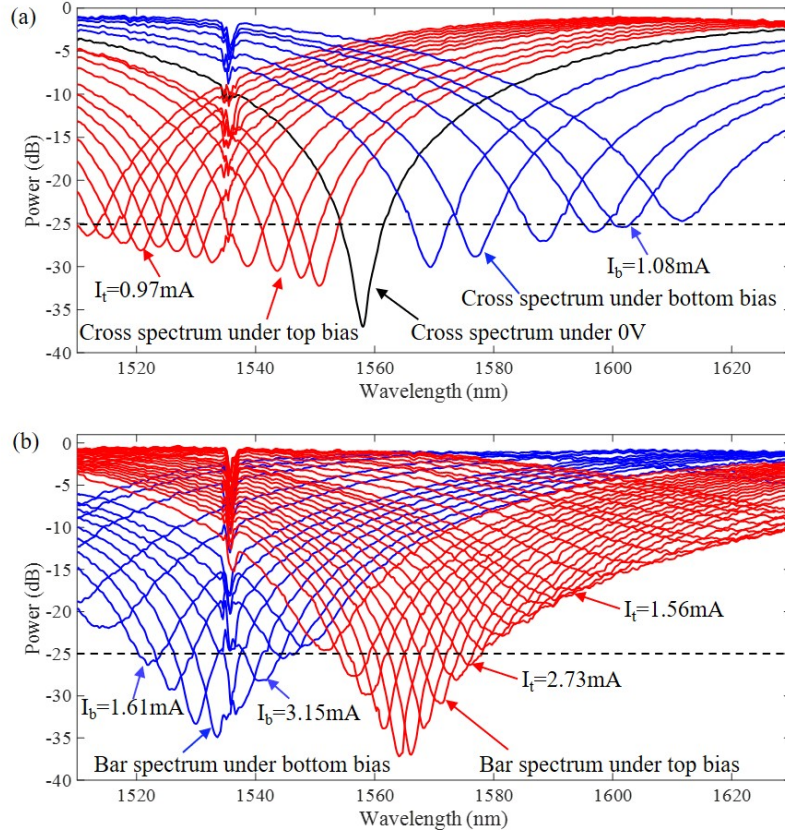


Figure 4.7: (a) Transmission spectra at the cross port of the MZS in the bar state when various bias current is applied to the top MZI arm (red lines) and to the bottom MZI arm (blue lines). (b) Transmission spectra at the bar port in the cross state with various bias current applied to the top MZI arm (red lines) and bottom MZI arm (blue lines).

design of 3-dB coupler mainly causes the difference in bandwidth measured in the bar state and cross-state. In addition, we note in Fig. 4.7(b), among all spectra under the bottom arm bias current, the spectrum for the maximum rejection has its minimum transmission power at 1536 nm, which is 12 nm blue-shifted from 1558nm. Similarly, among all spectra under top arm bias current, the spectrum for the maximum rejection has its minimum transmission power at 1566 nm, which is 8 nm red-shifted by 8 nm. This shift in minimum transmission can be mainly caused by the FCA in the MZS arms when the bias current is applied. More specifically, when FC is injected into the biased arm, the FCA reduces the power in this arm and thus changes the overall MZS spectra, which shows in the MZS spectrum, a shifted maximum rejection wavelength

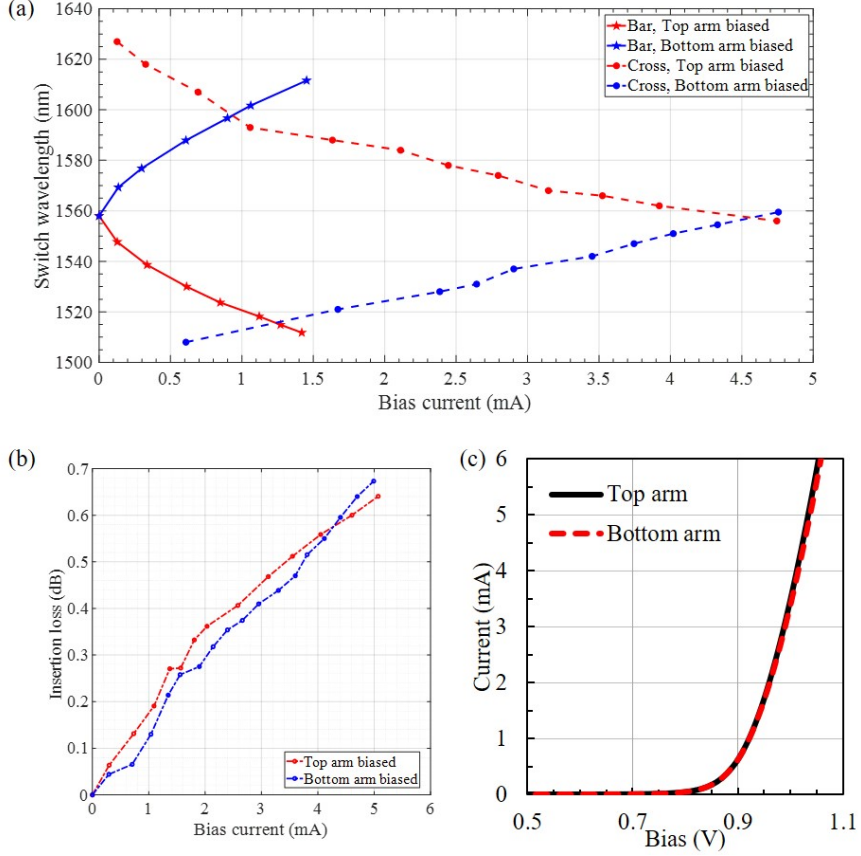


Figure 4.8: (a) Plot of the wavelength of maximum rejection as function of the applied bias current for the bar state (solid line) and cross state (dashed line). (b) Insertion losses of the MZS as functions of the bias current applied to the top and bottom arms. (c) I-V plot of the *pin* junction in each MZI arm.

(for the maximum rejection).

The maximum rejection wavelength tuning curves of the MZS are shown in Fig. 4.8(a), which plots the wavelengths of maximum bar-port rejection (circles) and cross-port rejection (stars) as functions of the bias current on the top (red curves) or bottom arm (blue curves) over the 25 dB rejection bandwidth, which is the operating bandwidth of the MZS. Fig. 4.8(b) plots the excessive insertion loss caused by FCA as a function of the bias current on each arm. It can be seen that the insertion loss is less than 0.7 dB over the entire operating bandwidth. Fig. 4.8(c) shows the I-V characteristics of the *pin* junctions in the top and bottom arms of the MZS. Thus we calculated the maximum electrical power required to perform switching to be 4.94

mW, which is the maximum power needed to obtain a π -phase shift between the two MZS arms within the operation wavelength range.

4.4 Performance of WS Circuit

To demonstrate the wavelength selection operation, we applied to the input of the WS circuit a signal consisting of two wavelengths, $\lambda_1=1570.3\text{nm}$, $\lambda_2=1572.2\text{nm}$, which are within the 25 dB switching bandwidth. VMR filter 1 (top filter) was initially tuned to the center wavelength λ_1 while VMR 2 filter (bottom filter) was tuned to the center wavelength λ_2 . The MZS was initially biased on the top arm with 0.175mA current to set it in the bar state, which transmitted wavelength λ_1 to output port 1. The initial spectrum measured at output port 1 is shown by the red curve in Fig. 4.9, from which we see wavelength λ_2 is suppressed by 29.3 dB compared to the selected wavelength λ_1 . We then switched the MZS to select λ_2 by applying a 2.96mA bias current to the bottom arm. The output spectrum is shown by the black curve in Fig. 4.9, which shows that wavelength λ_1 is now suppressed by 28.9 dB relative to λ_2 . For both cases, the wavelength isolation is limited by the extinction ratio of the MZS rather than the VMR filters (which had an out-of-band rejection ratio of 46 dB over 32.7 nm FSR). The insertion loss of the entire WS circuit is estimated to be 5.2 dB. In this example, the power required to select λ_1 to port 1 is $P_{VMR} + P_{MZS} = 142.16 + 0.14 = 142.3$ mW, and a total power of $199.12 + 2.82 = 201.94\text{mW}$ is required to select λ_2 at port 1. We note the VMR filter stage dissipates the most power, and the power consumption from the MZS could be ignored in most cases.

Next, we determined the wavelength selection time by measuring the thermal tuning time of the VMR filters, the switching time of the MZS and overall circuit frequency response. The measurement setup is shown in Fig. 4.10. A single-wavelength optical signal at 1560 nm from a tunable laser is adjusted to TE polarization and coupled to the WS circuit. Square-wave switching signals at the frequency of 1 kHz were generated and synchronized by a function generator and applied to the VMR

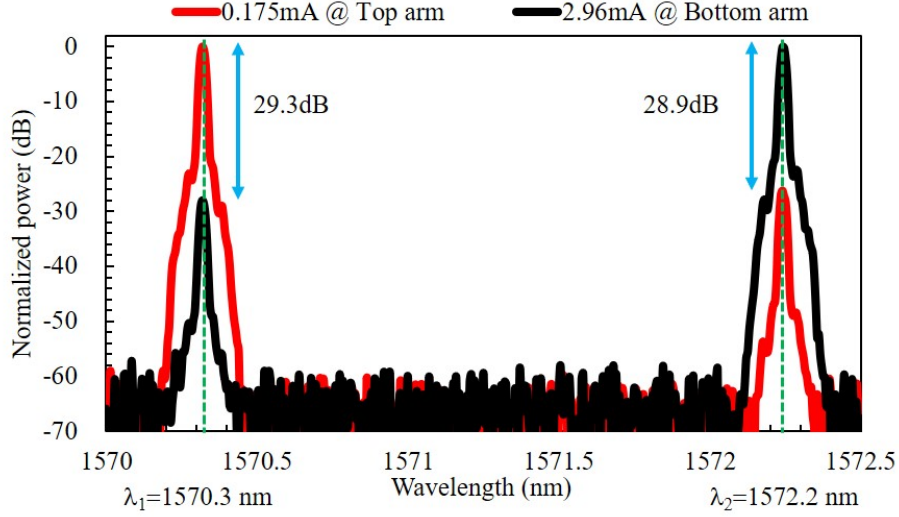


Figure 4.9: Measure spectral response at the output port 1 of the WS circuit for wavelength selection between two wavelengths $\lambda_1 = 1570.3nm$ and $\lambda_2 = 1572.2nm$.

filter stage. The amplitude of the square waves for all 4 heaters are 6 V, 5.34 V, 8.82 V, and 6.45 V to thermally tune the VMR filter to the wavelength λ_1 to drop the input wavelength while the other filter was tuned away from the wavelength. The dropped wavelength from filter 1 was then periodically switched to output ports 1 and 2 of the MZS using another 0.92 V square switching signal generated from another function generator. The transmitted optical power at port 1 (Bar port) of the MZS was detected by a high-speed photodetector and displayed on the oscilloscope. Figs. 4.11(a) and (b) show the oscilloscope traces of the VMR filter and MZS when each section works individually. From the trace in Fig. 4.11(a) we obtained the rise and fall times of the VMR filter to be 16 μs and 19 μs , respectively. From the trace in Fig. 4.11(b), we obtained 3.0 ns for both the rise and fall times of the MZS. We note that our equipment limits the switching time obtained for the MZS since the function generator produces a square waveform with a minimum rise/fall time of 3.0 ns. To further explore the WS circuit's wavelength selection time limit, we replace the square function generator for the MZS by a high-speed arbitrary signal generator, which outputs sinusoidal-wave up to 10 GHz. As demonstrated in Fig. 4.11(c), the WS circuit's time spectral response has an envelope at the frequency of 1 kHz,

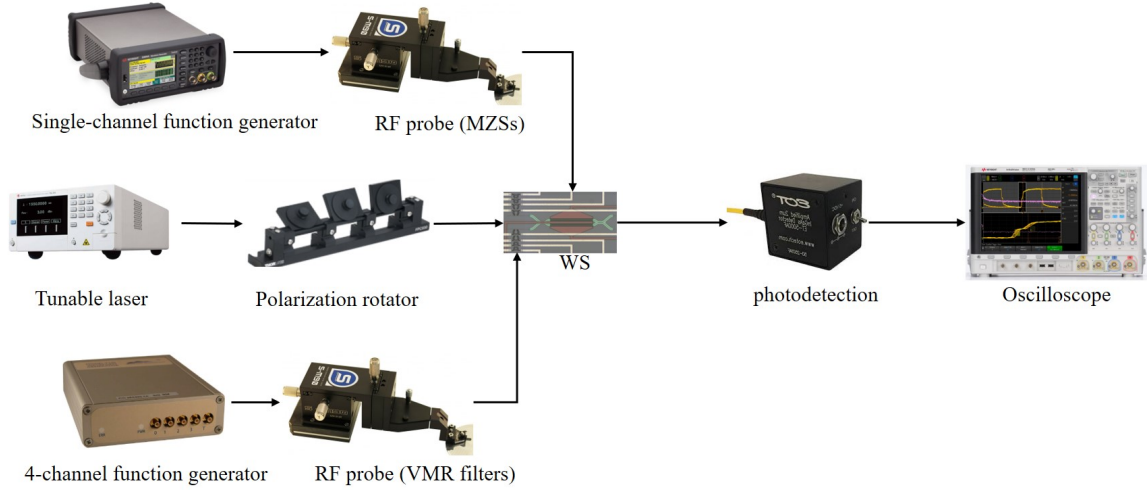


Figure 4.10: Experimental setup for measuring the time response of the WS circuit.

which is determined by the VMR filter controlled by the function generator. When the amplitude of the envelope is high, indicating the wavelength $\lambda_1 = 1560$ nm is dropped from the filter 1 and fed to the MZS, then the fast switching is performed by the MZS controlled by the arbitrary signal generator. Fig. 4.11(d) shows the WS circuit's frequency response at port 1 corresponds to the time spectrum shown in Fig. 4.11(c) under different MZS switching frequency. Results show that the output 3-dB bandwidth of the WS circuit is measured to be 300 MHz, representing an estimated switching time response of 1.5 ns of the MZS.

Under real operating conditions, the wavelength selection time is strongly dependent on the data transmission interval (T). The best case scenario is when the data transmission interval is longer than the thermal tuning time of the VMR filters. In this case, we can pretune the "free" VMR filter to the next wavelength without disturbing the data transmission on the currently selected wavelength. The next wavelength can then be selected by simply toggling the MZS switch, so the wavelength selection time is very fast (ns time scale). The worst case scenario occurs when the data transmission interval is shorter than the thermal tuning time. In this case, a new wavelength cannot be selected until one of the VMR filters is tuned to the desired wavelength. The wavelength selection time is thus limited by the thermal tuning time of the VMR

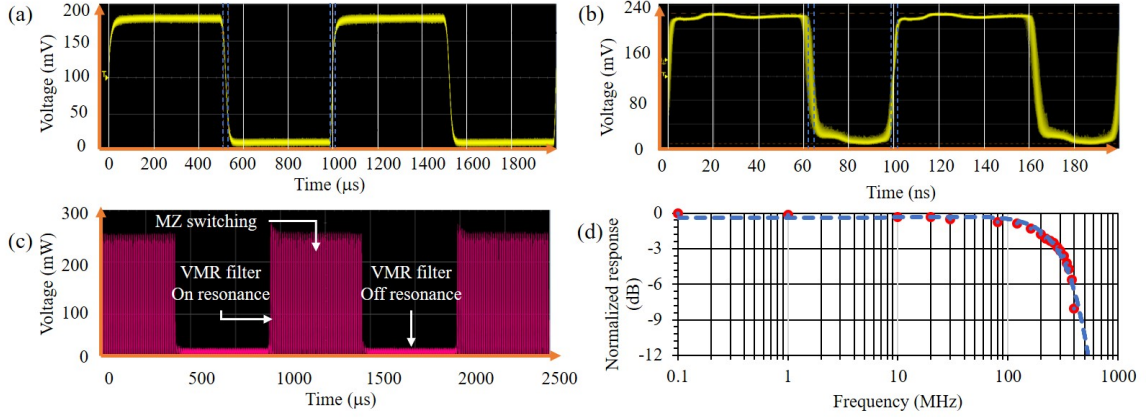


Figure 4.11: Time responses of (a) the 4th-order DC-VMR filter with thermal tuning, (b) the MZS with free carrier injection, (c) the WS circuit at port 1 when the filter 1 is tuned on-and-off resonance wavelength of 1560 nm periodically at 1kHz frequency, and filter 2 is tuned off resonance. MZS is switched on-and-off to pick the optical power between filter 1 filter 2 periodically at 100 kHz frequency. (d) Frequency response of the WS circuit when the MZS is modulated by the signal generator at various frequencies, showing a 3dB-bandwidth of 300MHz.

filters (μs time scale).

For data transmissions in WDM-PON systems, we define an update cycle as the time to complete traffic monitoring, demand estimation, and wavelength path setup. Current systems have update cycles varying from a few to hundreds of ms depending on the scale of the network [91][92][93]. These cycles are long enough for our VMR filters to be thermally tuned to the appropriate wavelengths as determined from traffic analysis results (e.g., the output port, output wavelength, output time slot) in every cycle. When needed, these wavelengths can be selected by the MZS within a few ns. Figs. 4.12(a) and (b) show the worst-case and best-case time responses, respectively, of the WS circuit as it switches from wavelength λ_1 (output of filter 1, shown in black) to wavelength λ_2 (output of filter 2, shown in red) to port 1. In case (a) where wavelength λ_2 is not preselected by filter 2, when the WS circuit changes the wavelength selection from λ_1 to λ_2 , MZS quickly switches off the optical power input from the filter 1 at λ_1 . However, the wavelength λ_2 will not be ready for pick up until the filter 2 is thermally tuned to λ_2 . Thus, the total response time of the

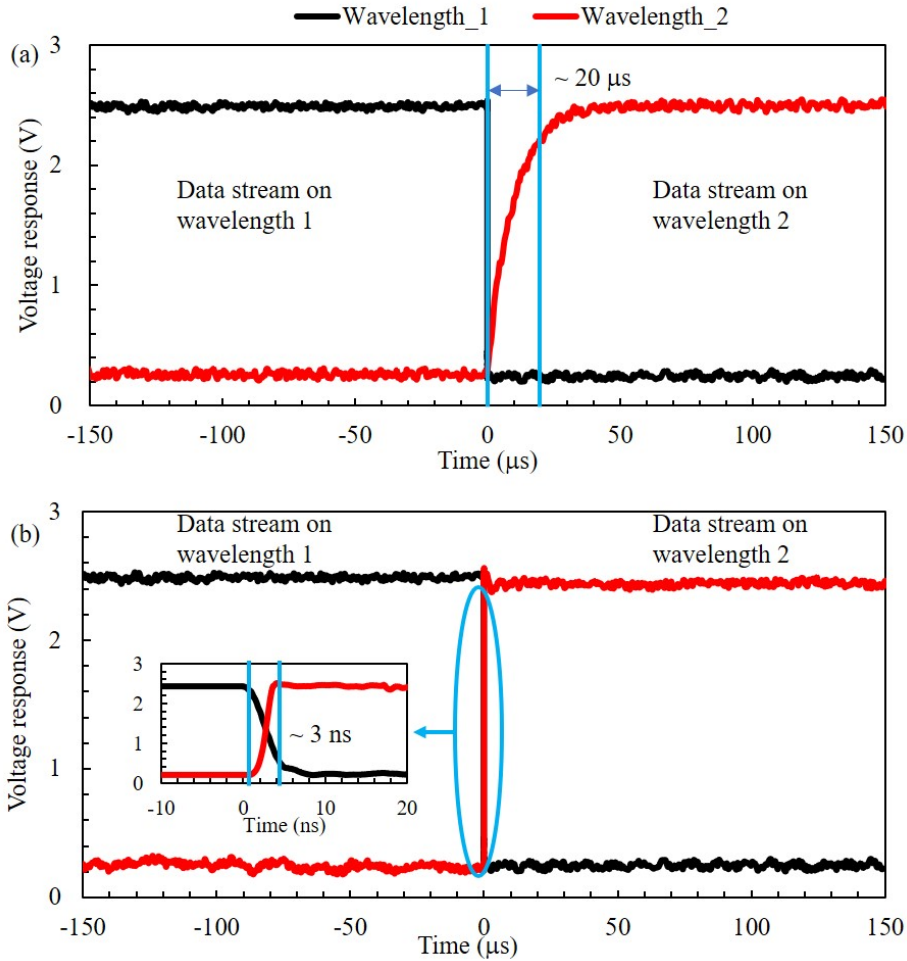


Figure 4.12: Comparison of the dead time in the operation of the WS circuit: (a) "worst case" when thermal tuning of the filter is needed, (b) "best case" when only the fast MZS switching is required.

wavelength selection is about $20 \mu\text{s}$. This time interval represents a dead time during which no data or packet can be transmitted. In case (b) where filter 2 is pretuned to wavelength λ_2 , as the inset plot of Fig. 4.13(b) indicates, it takes only 3 ns to do the wavelength switch between λ_1 to λ_2 , thus the dead time is much shorter, which significantly reduces the dead time and relief the load of cache memory.

4.5 Summary

In this chapter, we demonstrated a compact all-silicon photonic circuit for fast wavelength selection from a comb of laser wavelengths. The circuit incorporates a fast pin MZS with broadband tunable VMR filters, achieving a best-case wavelength selection time of 3 ns over 32.7 nm of wavelength channels. The WS circuit design is scalable to an arbitrary number of output wavelength channels by cascading more VMRs/MZS stages. For example, we have also realized an 8-channel WS consisting of a cascade of 8 pairs of VMR filters and 8 MZS's. Our silicon photonic circuit provides a novel compact solution for wavelength selection in high speed, low-latency optical networks.

Chapter 5

Variable Bandwidth Tunable Filters for Elastic Optical Networks

To meet the demand for increased data transmission volume and speed, optical networks are evolving towards becoming more "elastic" to achieve more efficient optical spectral utility. In WDM networks, the optical spectrum is divided into either a fixed wavelength grid or a flexible grid (ITU-T G.694.1). The fixed wavelength standard specifies the center wavelength spacing as 12.5 GHz, 25 GHz, 50 GHz or 100 GHz. Elastic optical networks (EONs) [94] adopt a flexible grid, which allows the center wavelength to be set at any multiple of 6.25 GHz starting from 193.1 THz, with variable transmission bandwidth set at any multiple of 6.25 GHz. Thus, an essential requirement of EONs is to change the channel transmission wavelength and bandwidth on demand dynamically. Toward this goal, there have recently been some efforts in developing CMR based ROADMs which are tunable in bandwidth [13][95][95][96].

The most straightforward approach for tuning a filter bandwidth is by cascading two fixed-bandwidth filter stages to form a VCMR filter, and varying the frequency detunes between the center wavelengths of the two stages [82][13][95]. The advantages of this scheme are that we only need two wavelength-tunable filters, such as the MRR filters demonstrated in Chapter 3. The bandwidth of the cascaded filter can be varied by merely tuning the center wavelengths of the individual filters. The disadvantage, however, is that the filter passband becomes severely distorted as the bandwidth is

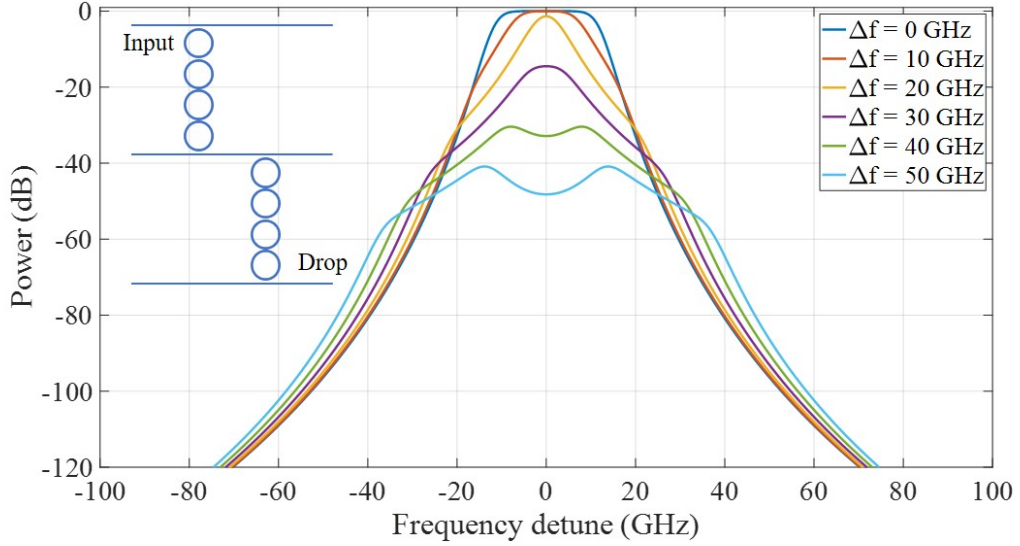


Figure 5.1: Simulated output spectral responses of a cascade of two 4th-order filters, each with 25 GHz 3-dB bandwidth, for various frequency detunings between the two stages.

varied, leading to high insertion loss. To demonstrate this, we show in Fig. 5.1 the spectral responses of two cascaded 4th-order MRR filters for various detunes Δf in the center frequencies of the two stages. As the frequency detune increases, the 3dB bandwidth decreases, but the passband shape becomes more pointy and eventually splits into two peaks. The insertion loss also increases significantly with increasing frequency detune.

In principle, to change the bandwidth of a coupled-cavity filter, we need to change the coupling coefficients between the cavities. There have been several VBW filter designs based on this approach. For example, Chen [97] reported a bandwidth tunable single-MRR filter which uses an interferometer structure to tune the coupling coefficient between the MRR and the input waveguide. The device only provides a first-order filter response and requires a separate heater (control) to tune the filter wavelength and another heater to optimize the bandwidth. Recently, Pouloupoulos [98] demonstrated a second-order MRR filter which employs 6 heaters to tune the three couplings and 2 additional heaters to tune the two MRR resonances, for a total

of 8 heaters altogether. The authors reported a tunable bandwidth of 12 GHz-116 GHz, although the filter shape became more pointy and skewed as the bandwidth was increased. Ding [95] and Dai [96] reported similar VBW MRR filter designs by combining two filters in parallel. However, their devices suffered from high insertion loss and high control complexity (in terms of the required number of heaters). To date, all the VBW filter designs reported have been limited to first or second-order spectral responses, and most need additional controls to tune the bandwidths.

In this chapter, we propose a universal architecture for a variable bandwidth (VBW) photonic filter with arbitrary (even) order. The design uses a Mach-Zehnder interferometer loaded with N MRRs on each arm to construct a filter of order $2N$, which we refer to as the MZI-MRR filter design. The center wavelength and bandwidth of the filter can be tuned by tuning only the MRR resonances without varying the coupling coefficients so that the filter does not require additional heaters (controls) bandwidth tuning. In particular, we show that by tuning only the MRR resonances, the ideal movement trajectory of the poles of the filter can be approximated along the imaginary axis (to be discussed in Section 5.2) while the zeros are still located on the imaginary axis so that the bandwidth of the filter can be tuned without causing insertion loss within a specified maximum ripple tolerance in the passband. The filter characteristics such as insertion loss, in-band ripple and out-band rejection level can thus be maintained over a wide bandwidth tuning range.

The rest of this chapter is organized as follows. In Section 5.1 we investigate the theoretical requirement for tuning a high-order filter bandwidth in terms of the movement of its poles and zeros. In Section 5.2, we investigate the bandwidth tuning performance of the MZI-MRR filter by approximating its poles' movement to the ideal pole trajectory of a VB filter. Section 5.3 presents the implementation and experimental characterization of a 4th-order VBW filter. The chapter is summarized in Section 5.4.

5.1 Ideal Pole and Zero Movements of a Bandwidth Tunable Filter

To understand the design requirements of a VB filter, we determine the ideal movements of poles and zeros of a filter when its bandwidth is varied. Suppose we have a filter with transfer function:

$$H(s) = \frac{P(s)}{Q(s)}. \quad (5.1)$$

Tuning the filter bandwidth is equivalent to scaling the frequency axis by

$$s' = s/a, \quad (5.2)$$

where a is a bandwidth scaling factor. If p is a pole the transfer function, then the polynomial $Q(s)$ contains a factor of the form:

$$Q_p(s) = s - p \quad (5.3)$$

The pole of the new transfer function after bandwidth tuning is given by the factor

$$Q_p(s') = Q_p(s/a) = s/a - p = (1/a)(s - ap) = (1/a)(s - p') \quad (5.4)$$

Thus the new pole is now given by

$$p' = ap = a \times Re(p) + ja \times Im(p) \quad (5.5)$$

As we increase the bandwidth (increasing a), the new pole p' follows a trajectory defined by a straight line through the origin in the complex plane. By the same analysis, the movements of the zeros also follow straight lines through the origin in the complex plane. As an example, we show in Fig. 5.2(a) the spectral responses of a 2^{nd} -order filter with varying bandwidths. Fig. 5.2(b) shows its pole locations as the bandwidth is increased, which follow straight lines through the origin. Thus to tune a filter bandwidth, we need to change both the real and imaginary parts of each pole (and zero) by the same amount. For a coupled microring filter, this generally requires changing both the coupling coefficients and the resonant frequencies of the

MRRs, which would require separate controls for both parameters. However, over a limited bandwidth tuning range, it is possible to approximate the ideal pole/zero movements by just the movements of the imaginary parts of the poles and zeros. The effect of this approximation is that we introduce ripples and even insertion loss in the passband. However, as we show in the next section, the MZI-MRR filter architecture allows for bandwidth tuning over a certain range without incurring extra insertion loss.

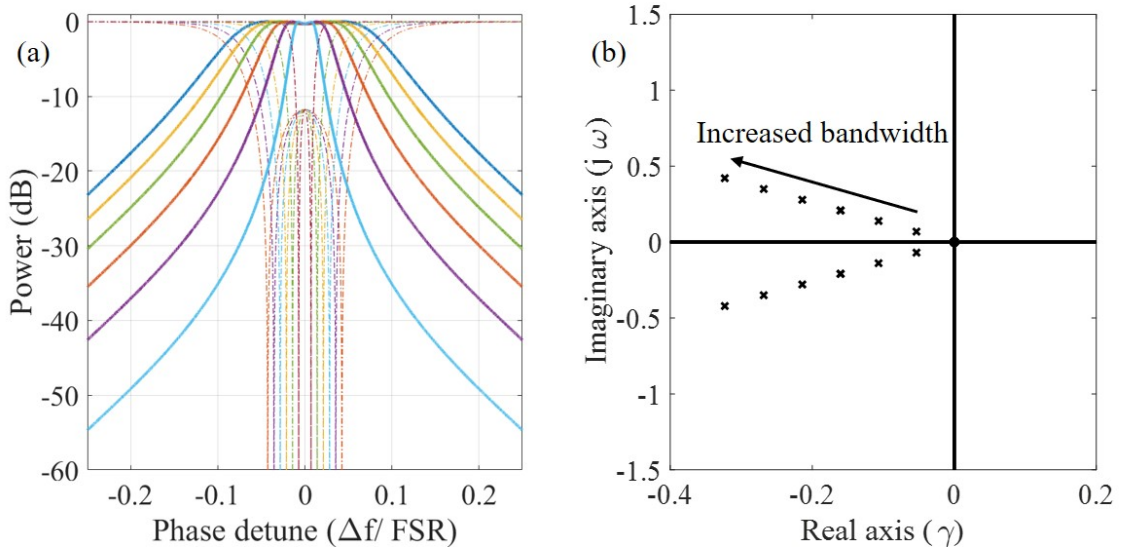


Figure 5.2: (a) Spectral responses of a 2nd-order Butterworth filter with different bandwidths. (b) Pole locations corresponding to the spectra in (a).

5.2 The MZI-MRR Bandwidth Tunable Filter Architecture

The MZI-MRR architecture is also known as the sum-difference filter architecture. It can be used to realize general filter transfer functions with $2N$ poles and $2(N - 1)$ zeros[35], where N is the number of MRRs in each arm of the MZI. Although the theory and design methodology as a general filter are well developed[99][100][101], the bandwidth tunability has been neither analyzed nor experimentally demonstrated

before. Our objective here is to show that the MZI-MRR configuration can also be used to realize VBW filters by tuning only the MRR resonance frequencies without causing extra insertion loss.

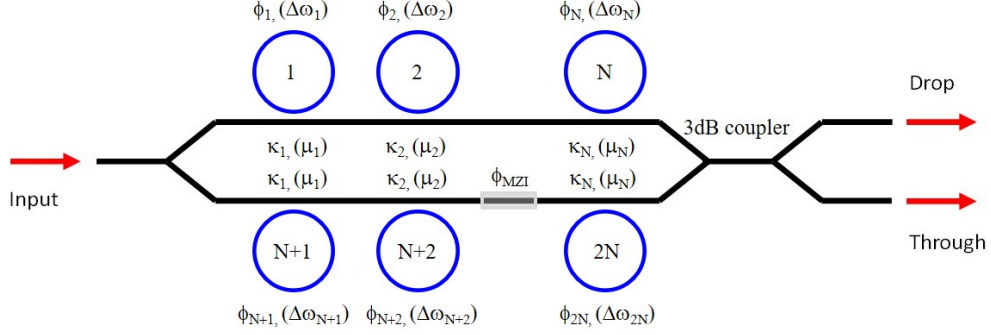


Figure 5.3: Schematic diagram of the MZI-MRR filter of order $2N$.

Fig. 5.3 shows a schematic diagram of an MZI-MRR filter of order $2N$. The input optical signal is split into two equal parts, each then fed into an all-pass (AP) network in each arm of the MZI. Each AP network consists of a cascade of N MRRs of same radius R in the all-pass configuration, with the k^{th} microring having a frequency detune $\Delta\omega_k$ and coupled to the MZI waveguide with coupling coefficient μ_k . The transfer functions of the two AP networks are designed to be complex conjugates of each other, which we denote H_{ap} and H_{ap}^* for the top and bottom networks, respectively. A phase shifter is placed on the bottom arm to introduce $\pi/2$ phase difference between the two arms. The outputs of the two AP networks are recombined at the output 3dB coupler to give the sum (through) and difference (drop) transfer functions:

$$H_+ = \frac{1}{2}(H_{ap} + H_{ap}^*), \quad (5.6)$$

$$H_- = \frac{1}{2}(H_{ap} - H_{ap}^*), \quad (5.7)$$

Since each AP network consists of a cascade of APMRs, its total transfer function is just the product of the transfer functions of the N APMRs. Specifically, the transfer function $A_k(s)$ in the complex frequency domain of the k^{th} MRR in each MZI arm

has the general form

$$A_k(s) = \frac{s - j\Delta\omega_k - \mu_k^2/2}{s - j\Delta\omega_k + \mu_k^2/2} = \frac{s + p_k^*}{s - p_k} \quad (5.8)$$

Thus the APMR has a pole at p_k and a zero at $-p_k^*$, with the real part determined by the coupling coefficient μ_k and the imaginary part determined by the frequency detune $\Delta\omega_k$:

$$p = -\mu^2/2 + j\Delta\omega, \quad (5.9)$$

$$z = -p^*. \quad (5.10)$$

The transfer function of the cascaded array of N microrings in the top MZI arm is thus

$$H_{ap}(s) = \prod_{k=1}^N \frac{s + p_k^*}{s - p_k}. \quad (5.11)$$

The above expression shows that the poles and zeros of the AP network are simply those of the N microrings. Since the transfer function of the bottom AP network is the complex conjugate of H_{ap} , its poles and zeros must be the complex conjugates of the corresponding poles and zeros of the top network. Therefore the N microrings in the bottom MZI arm must have identical coupling coefficients but opposite (negative) frequency detunes as those in the top arm. We also see that the poles of the sum/difference transfer functions of the filter are comprised of the poles of the two AP networks. Thus, we can directly move the poles of the MZI-MRR filter by moving the poles of the individual MRRs. In particular, we can vary the imaginary parts of the filter poles by simply varying the resonant frequencies of the MRRs. This allows us to approximate the ideal pole movement of the VB filter. In the next section, we will show that there is a range of bandwidth tuning, called the insertion loss-free (IL-free) tuning range, which does not cause insertion loss in the filter passband.

5.2.1 Insertion Loss-Free Bandwidth Tuning Range in MZI-MRR Filters

For a filter to have zero insertion loss, there must be at least one frequency in the passband where the power transmission is 1. To demonstrate that there exists an IL-free range of frequency detunes of an MZI-MRR filter, we will consider specific cases of a 2nd-order and a 4th-order filter. For a 2^{nd} -order MZI-MRR filter, each MZI arm is coupled to only 1 MRR with coupling coefficient μ and frequency detune $\pm\Delta\omega$. The transfer functions at the difference (transmission) port and sum (reflection) port are given by:

$$H_- = \frac{-j\mu^2\Delta\omega}{(s - j\Delta\omega - \mu^2/2)(s - j\Delta\omega + \mu^2/2)}, \quad (5.12)$$

$$H_+ = \frac{s^2 - (\mu^2/2)^2 + \Delta\omega^2}{(s - j\Delta\omega - \mu^2/2)(s - j\Delta\omega + \mu^2/2)}. \quad (5.13)$$

The condition that there is no insertion loss in the passband implies that the zeros of the reflection spectrum (H_-) must be located on the imaginary axis. From the above expressions, we obtain the zeros of reflection spectrum (H_+) as

$$z = \pm j\sqrt{\Delta\omega^2 - (\mu^2/2)^2} \quad (5.14)$$

Thus, for frequency detunes $\Delta\omega \geq \mu^2/2$, the zeros remain on the imaginary axis of s-plane and there is no insertion loss in the passband. The spectral response is maximally flat at $\Delta\omega = \mu^2/2$. As the detune $\Delta\omega$ increases, ripple starts to appear in the passband, but the peak transmission is always 1. The bandwidth tuning range in this case is limited by the maximum tolerable ripple in the passband. In contrast, we note that for a 2^{nd} -order serially-coupled filter, the through port (reflection) transfer function in the presence of symmetric frequency detuning $\pm\delta\omega$ in the two MRRs is given by:

$$H_t = \frac{s^2 + (\delta\omega + j\mu_0^2/2)^2 + \mu_1^2}{(s^2 + \mu_0^2/2 + j\sqrt{\mu_1^2 + \delta\omega^2})(s^2 + \mu_0^2/2 - j\sqrt{\mu_1^2 + \delta\omega^2})}, \quad (5.15)$$

where μ_0 , μ_1 , and $\delta\omega$ are the bus-to-ring coupling coefficient and ring-to-ring coupling coefficient, respectively. The zeros are given by:

$$s = \pm j\sqrt{(\delta\omega + \mu_0^2/2)^2 + \mu_1^2}, \quad (5.16)$$

which will never be pure imaginary for $\delta\omega \neq 0$, implying the insertion loss will occur for any amount of frequency detune. For the serially coupled microring filter architecture, IL-free bandwidth tuning can only be achieved if we vary both the frequency detunes and the coupling coefficients, whereas in the MZI-MRR architecture, we can vary the bandwidth by only detuning the MRR resonances.

For a 4th order MZI-MRR architecture, each arm now has 2 MRRs with two poles and two zeros. The transfer function of the AP network on the upper arm is:

$$H_{ap} = \frac{(s + p_1^*)(s + p_2^*)}{(s - p_1)(s - p_2)}. \quad (5.17)$$

and the transfer function at the sum port is:

$$H_+ = \frac{(s^2 - p_1^{*2})(s^2 - p_2^{*2}) + (s^2 - p_1^2)(s^2 - p_2^2)}{(s - p_1)(s - p_2)(s - p_1^*)(s - p_2^*)}. \quad (5.18)$$

The zeros of the sum port are obtained by solving the equation:

$$s^4 - (p_1^2 + p_1^{*2} + p_2^2 + p_2^{*2})s^2 + (p_1^2 p_2^{*2} + p_1^{*2} p_2^2) = 0. \quad (5.19)$$

By substituting the expressions for the poles and zeros in Eq. 5.9 and 5.10 into Eq. 5.19, we have

$$s^4 - \gamma_1 s^2 + \gamma_2 b = 0, \quad (5.20)$$

where

$$\gamma_1 = (\mu_1^2/2)^2 - (\Delta\omega_1)^2 + (\mu_2^2/2)^2 - (\Delta\omega_2)^2, \quad (5.21)$$

$$\gamma_2 = \eta_1 \Delta\omega_1^2 + \eta_2 \Delta\omega_2^2 + \eta_3, \quad (5.22)$$

and

$$\eta_1 = \Delta\omega_2^2 - \mu_2^4/4, \quad (5.23)$$

$$\eta_2 = -\Delta\omega_2 \mu_1^2 \mu_2^2, \quad (5.24)$$

$$\eta_3 = -\eta_1 \mu_1^4/4. \quad (5.25)$$

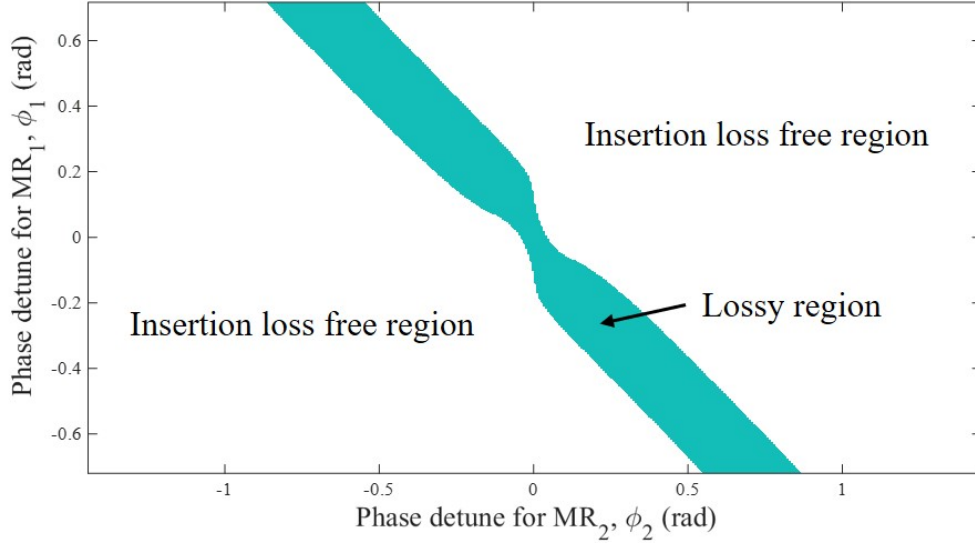


Figure 5.4: Plot of the IL-free region of a 4th-order MZI-MRR filter as functions of the phase detunes ϕ_1 and ϕ_2 of the 2 MRRs on the top MZI arm.

The criterion for both zeros to be imaginary is expressed as a relative condition on the frequency detunes $\Delta\omega_1$ and $\Delta\omega_2$ of the two MRRs:

$$\frac{\Delta\omega_1\mu_1^2\mu_2^2 - \sqrt{\Delta\omega_1^2\mu_1^4\mu_2^4 + (\Delta\omega_1^2 - \mu_1^4/4)^2\mu_2^4}}{2(\Delta\omega_1^2 - \mu_1^4/4)} \leq \Delta\omega_2 \leq \frac{\Delta\omega_1\mu_1^2\mu_2^2 + \sqrt{\Delta\omega_1^2\mu_1^4\mu_2^4 + (\Delta\omega_1^2 - \mu_1^4/4)^2\mu_2^4}}{2(\Delta\omega_1^2 - \mu_1^4/4)}, \quad (5.26)$$

for $\gamma_1 \geq 0$ and

$$\Delta\omega_2 \leq \frac{\Delta\omega_1\mu_1^2\mu_2^2 - \sqrt{\Delta\omega_1^2\mu_1^4\mu_2^4 + (\Delta\omega_1^2 - \mu_1^4/4)^2\mu_2^4}}{2(\Delta\omega_1^2 - \mu_1^4/4)}, \quad (5.27)$$

or

$$\Delta\omega_2 \geq \frac{\Delta\omega_1\mu_1^2\mu_2^2 + \sqrt{\Delta\omega_1^2\mu_1^4\mu_2^4 + (\Delta\omega_1^2 - \mu_1^4/4)^2\mu_2^4}}{2(\Delta\omega_1^2 - \mu_1^4/4)}, \quad (5.28)$$

for $\gamma_1 \leq 0$.

We have visualized in Fig. 5.4 the plot of the IL-free domain as functions of the normalized phase detunes $\phi_1 = 2\pi\Delta\omega_1/\Delta\omega_{FSR}$ and $\phi_2 = 2\pi\Delta\omega_2/\Delta\omega_{FSR}$ on each arm. The bandwidth tuning of the MZI-MRR filter can then be realized by simply detuning the phase of each MRs in the insertion-loss free region in Fig. 5.4. We also

note that when the condition $\Delta\omega_1 = 0$ is set for MR_1 on each arm, the criteria in Eq. 5.26-5.28 can be reduced to:

$$\Delta\omega_2 \geq \mu_2^2/2, \quad (5.29)$$

which is the result of Eq. 5.14, implying that a 4^{th} -order MZI-MRR filter response is degraded to a 2^{nd} -order MZI-MRR filter response after aligning two conjugate MRs on each arm. Therefore, a $2N^{th}$ -order MZI-MRR filter with coupling coefficients of $\mu_1 \dots \mu_N$ and frequency detunes $\Delta\omega_1 \dots \Delta\omega_N$, can realize any even number order filter response with variable bandwidth and no insertion loss for an order number $n = 2, 4, 6, \dots, 2N$.

5.2.2 Bandwidth Tuning Performance of a 4^{th} -order MZI-MRR Filter

In this section, we present the design of a practical 4^{th} -order MZI-MRR filter and analyze its bandwidth tuning performance. For more rigorous analysis, we will perform the analysis using the power coupling model of the MRRs. We design a 4^{th} -order MZI-MRR VBW filter with an FSR of 1 THz, a normalized 3dB bandwidth of $\Delta\lambda_{BW}/\Delta\lambda_{FSR} = 0.07$, in-band ripple of 0.3 dB. The filter is designed using the method of the delay-line circuit with ring waveguides [102], from which we obtain field coupling coefficients $\kappa_1 = 0.5$ for MRRs 1 and 3 and $\kappa_2 = 0.3$ for MRRs 2 and 4. The phase detunes are $\phi_1 = \pm 0.13$ rad for MRRs 1 and 3, $\phi_2 = \pm 0.30$ rad for MRRs 4 and 2. The transfer function of the k^{th} APMR on each arm in the z domain is:

$$A_{ap,k}(z) = \frac{\tau_k - \alpha_{rt}z^{-1}}{1 - \tau_k\alpha_{rt}z^{-1}} = \frac{p_k^*z - 1}{z - p_k} e^{-j\phi_k} \quad (5.30)$$

where $z^{-1} = \alpha_{rt}e^{-j(\phi_{rt} + \phi_k)}$ is the roundtrip delay variable, $\phi_{rt} = 2\pi\beta R$ is the roundtrip phase of the MRR and R is the radius of MRs, ϕ_k is the phase detune of the k^{th} MR, $\alpha_{rt} = e^{\pi\alpha R}$ is the roundtrip amplitude attenuation factor, α is the propagation loss in the microring waveguide, and $\tau_k = \sqrt{1 - \kappa_k^2}$ is the transmission coefficient of

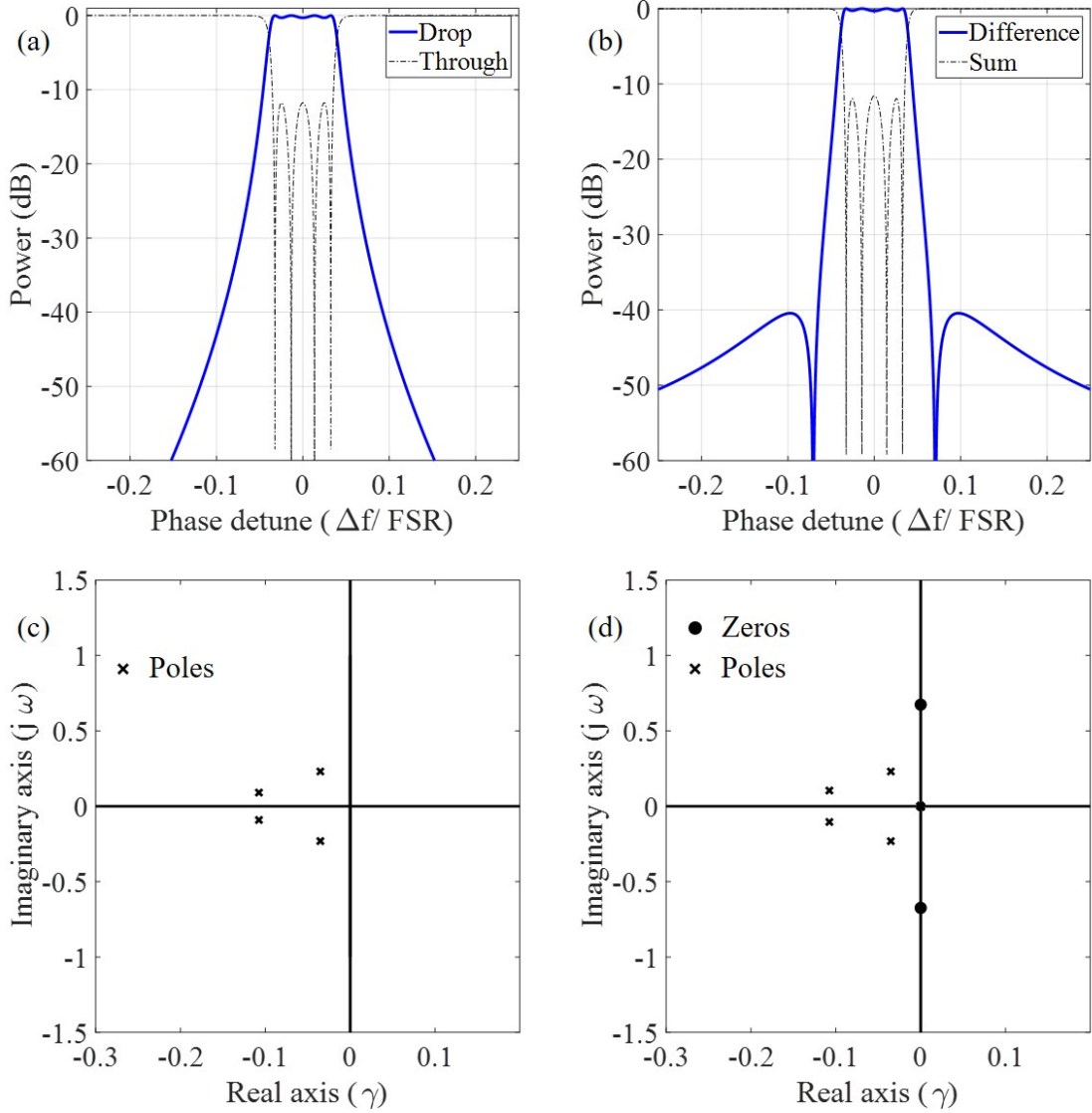


Figure 5.5: Comparison of the ideal spectral responses of (a) a 4th-order serially-coupled microring (CMR) filter and (b) a 4th-order MZI-MRR filter. Both filter spectra have 25 GHz ripple bandwidth and no insertion loss. (c) and (d) The corresponding pole-zero diagrams of the transmission spectra (blue curves) in (a) and (b).

the k^{th} coupling junction. The transfer function of microring k thus has a pole $p_k = \tau_k e^{-j\phi_k}$ and a zero at $1/p_k^*$, with the magnitude of the pole equal to the transmission coefficient τ_k and its phase equal to the phase detune ϕ_k of the microring. The transfer function of the cascaded array of N MRs in the top MZI arm is thus

$$A_{ap}(z) = \prod_{k=1}^N \frac{p_k^* z - 1}{z - p_k} e^{-j\phi_k}. \quad (5.31)$$

The transfer function of the bottom APMRs is just the complex conjugate of $A(z)$. Fig. 5.5(b) shows the spectral response of the 4th-order MZI-MRR filter with nominal design parameters. As a comparison, we plot in Fig. 5.5(a) the spectral response of a 4th-order CMR filter with the same bandwidth and inband ripple. The corresponding pole-zero diagrams for the CMR and MZI-MRR filters are displayed in Figs. 5.5(c) and (d).

In Fig. 5.6(b) we show the bandwidth variation of the 4th-order MZI-MRR filter corresponds to the poles trajectories shown in Fig. 5.6(c). As a comparison, Fig. 5.6(a) shows 4th-order CMR filter responses bandwidth equal to the bandwidth tuning range shown in Fig. 5.6(b), inset plots in Figs. 5.6(a) and (b) show the details of inband ripple for different bandwidth in both filters. Fig. 5.6(c) shows the poles movement of the CMR filter (in black) and MZI-MRR filter (in red). We note that poles of MZI-MRR filter only move along the imaginary axis, indicating the coupling coefficients are not changed. This fixed coupling coefficients with variable phase detunes lead to the increased inband ripple we observed in the inset plots of Fig. 5.6(b). In contrast, as both imaginary and real parts of poles are scaled, the poles plotted in black in Fig. 5.6(c) can maintain the fixed inband ripple, as shown inset plots of Fig. 5.6(a). The transformed pole trajectories in the inverse- z plane for both filters are displayed in Fig. 5.6(d), which is more accurate when it reflects the poles' real trajectory for broad bandwidth spectra. We note poles of the MZI-MRR filter rotate around the origin point with fixed radii, implying fixed coupling coefficients and variable phase detunes.

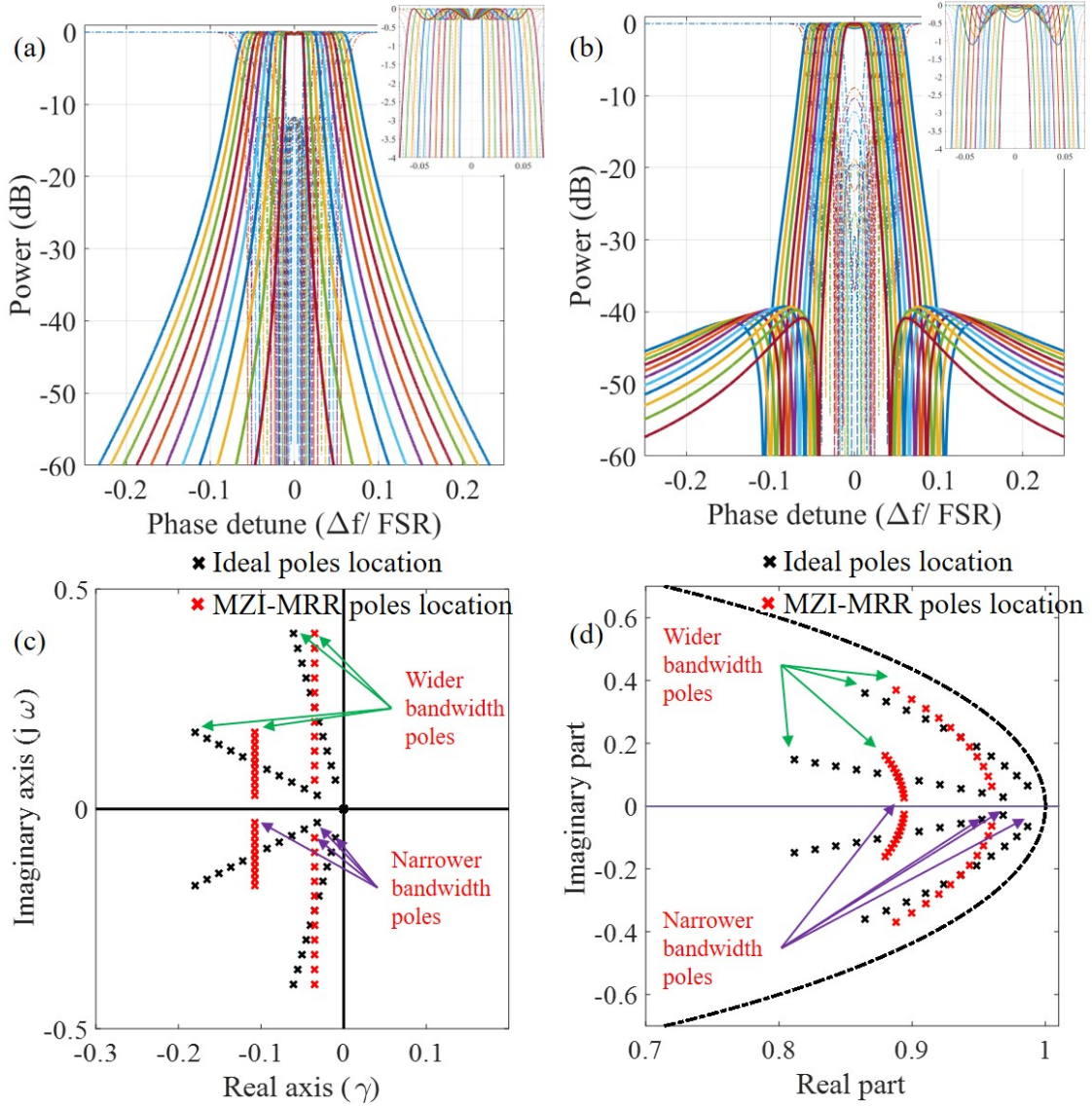


Figure 5.6: (a) Spectral responses of an ideal 4th-order filter with normalized bandwidth varied from 0.02 to 0.12. Inset plots show the details of inband ripples. (b) Spectral responses of a 4th-order MZI-MRR filter with bandwidth tuned from 0.02 to 0.12 by varying the MRR resonant frequencies. Comparison of the pole movements of the ideal CMR filter (black crosses) and MZI-MRR filter (red crosses) in (c) the s -plane and (d) the z -plane, the dash-line represents the unit circle in the z plane.

Therefore, it is possible to estimate the bandwidth tuning range of an MZI-MRR filter by setting a maximum inband ripple tolerance factor ϵ_m . Assuming the coupling coefficients $\kappa_1 = 0.5$ and $\kappa_2 = 0.3$, Figs. 5.7 show the variations of normalized ripple bandwidth, which is defined as the bandwidth to FSR ratio, for a certain ϵ_m in dB

scale, as functions of the normalized phase detune ϕ_1 and ϕ_2 . In particular, (a) and (b) plot the normalized bandwidth and corresponding inband ripple contour for $\epsilon_m = 1$ dB. The simulation result indicates the normalized bandwidth tuning range is from 0.01 to 0.12. Similarly, (c) and (d) show the normalized bandwidth tuning range and inband ripple contour for the case where $\epsilon_m = 2$ dB. We estimate the bandwidth tuning range is from 0.01 to 0.16.

Since all MRs are asynchronously detuned in a MZI-MRR filter, the spectral optimization is more challenging than in conventional CMR filters where the resonant frequencies of all the MRRs are aligned. In the next section, we report and experimentally demonstrate the MZI-MRR VBW filter with dynamic in-resonator photodetector for asynchronous phase control in the bandwidth tuning process.

5.3 Demonstration of a 4th-Order MZI-MRR VBW Filter

5.3.1 Design and Implementation of the MZI-MRR Filter

We realized the 4th-order MZI-MRR filter design in the previous section as shown in Fig. 5.8(a). Both the input splitter and output combiner of the MZI were implemented using Y-branch structures. Each MZI arm consisted of two identical race track (RT) resonators, each having 10 μm radius and 2- μm long straight sections to provide sufficiently strong coupling to the MZI waveguide. The coupling gaps between the two RT resonators and the MZI waveguide were designed to be 236 nm and 298nm, respectively, to obtain corresponding coupling coefficients of 0.5 and 0.3. The RT resonators had an FSR of 1 THz (8 nm) and were thermo-optically tuned using TiN microheaters placed on top. To minimize thermal crosstalk between heaters, the two RT resonators on each MZI arm were placed 100 μm apart. The MZI arms had an equal length of 400 μm , with microheaters covering a 200 μm length on each arm to control the phase. The device is fabricated on an SOI platform through Advanced

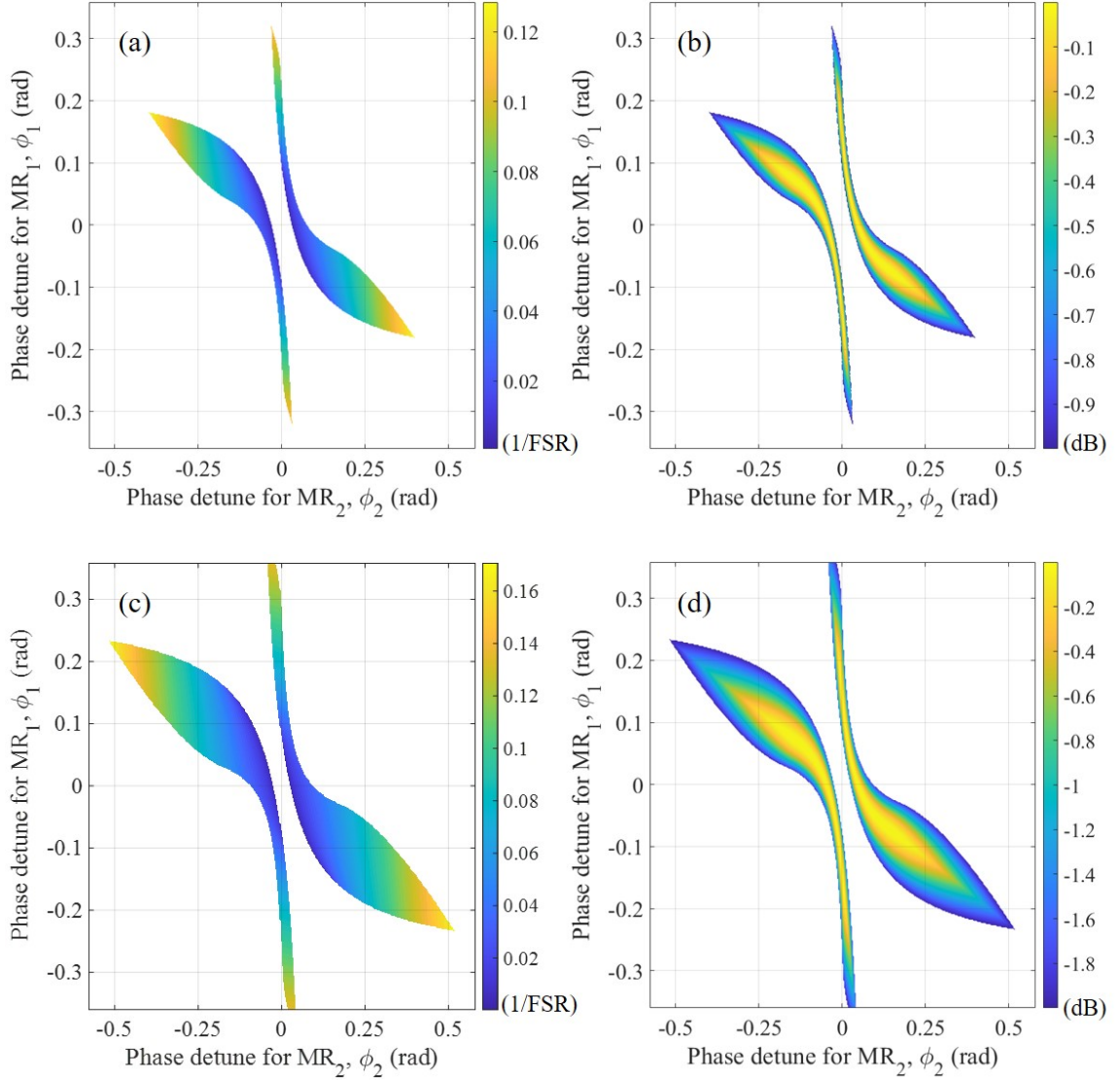


Figure 5.7: Contour plots of (a) the normalized ripple bandwidth and (b) the ripple variations for $\epsilon_m = 1$ dB, as functions of the normalized frequency detunes ϕ_1 and ϕ_2 . (c) and (d) are the ripple bandwidth and ripple variations contour plots for $\epsilon_m = 2$ dB. Both bandwidth plots are in the unit of $1/\text{FSR}$, both ripple variation plots are in the unit of dB.

Micro Foundry (AMF) in Singapore, where the waveguide structure was implemented using rib waveguides with 500 nm rib width and 90 nm slab thickness. The input and output rib waveguides of the MZI were tapered to 500 nm wide stripe waveguides by a 20 μm slab taper. The stripe waveguides were then extended to the edges of the chip, where they were further tapered down to 200 nm width for edge coupling with

lensed fibers. An image of a fabricated device shown in Fig. 5.8(b), with a close-up view of one of the RTs shown in Fig. 5.8(d).

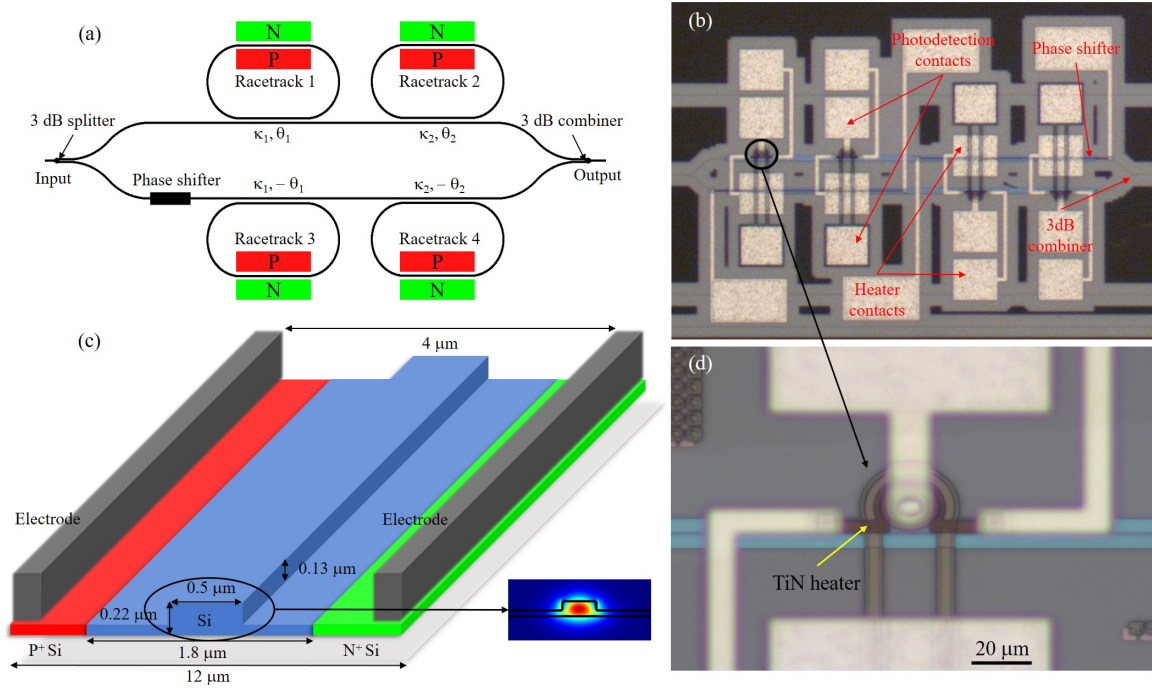


Figure 5.8: (a) Schematic of the 4th-order MZI-MRR filter design. (b) Microscope image of a fabricated device. (c) Schematic of the racetrack waveguide showing the embedded *pin* junction for resonance tracking. (d) Close-up view of an APMR on top arm.

For this device, we also embedded a *pin* junction in each RT to detect the photocurrent generated in the resonator. Such a current allows us to monitor the resonance frequency of each resonator during the filter tuning process. A cross-section view of the *pin* junction embedded in the RT rib waveguide is shown in Fig. 5.8(c). A reverse bias voltage is applied across each *pin* junction using separate electrodes from those for thermal tuning. Fig. 5.8(c) also shows the electric field distribution of the fundamental TE mode in the rib waveguide. It can be seen that the separation of doping areas and metal electrodes are large enough that the optical mode in the waveguide is well confined.

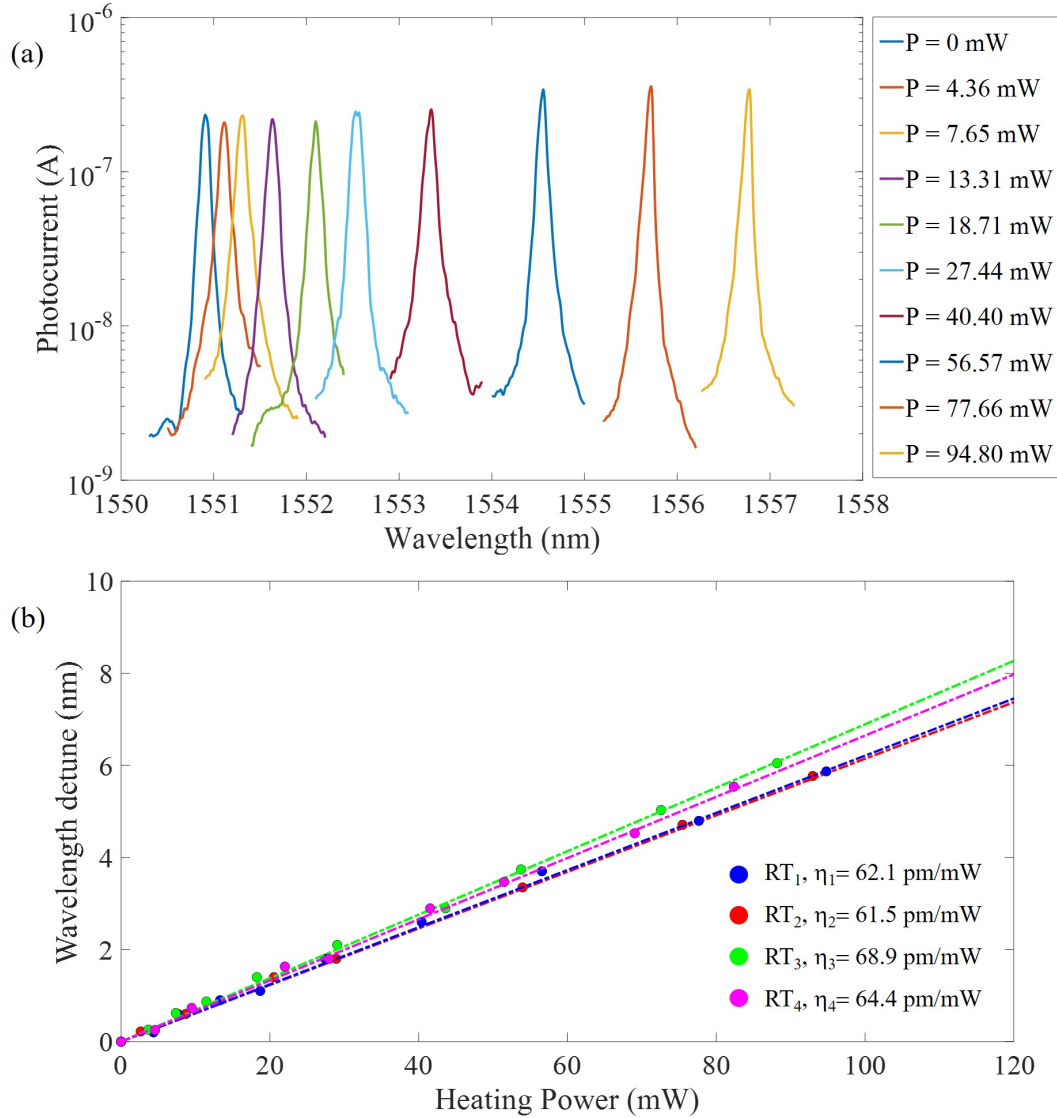


Figure 5.9: (a) Photocurrent spectra of RT 1 at different heater powers (similar spectra are obtained for the other RTs). (b) Wavelength tuning curves for RTs as determined from the wavelengths of the peak photocurrents in (a).

5.3.2 Performance of the MZI-MRR Filter

We first determined the thermal tuning curve of each RT resonator by measuring its resonance spectra at different applied heater powers. The resonance spectrum of the RT was obtained by sweeping the wavelength of an input TE-polarized CW laser and measuring the photocurrent generated in the *pin* junction of the RT. The reversed bias voltage applied across the *pin* junction was 15 V, and the input optical power

was set to be $100 \mu\text{W}$ to avoid thermo-optic nonlinearity in the resonator (this effect will be discussed in Chapter 6). Fig. 5.9(a) shows the photocurrent spectra of RT 1 measured for different heater powers, with similar spectra obtained for the other RTs. By determining the resonance wavelength shift versus the applied heater power, we generated the thermal tuning curves for each RT resonator, which are plotted in Fig. 5.9(b). The slopes of the linear best fit lines give the thermal tuning rates of the RTs, which are in the range of 60 - 70 pm/mW, as indicated in the plot. Since the RTs are placed far apart, there is negligible thermal crosstalk between them. These tuning curves will be used to tune the center wavelength and bandwidth of the MZI-MRR filter.

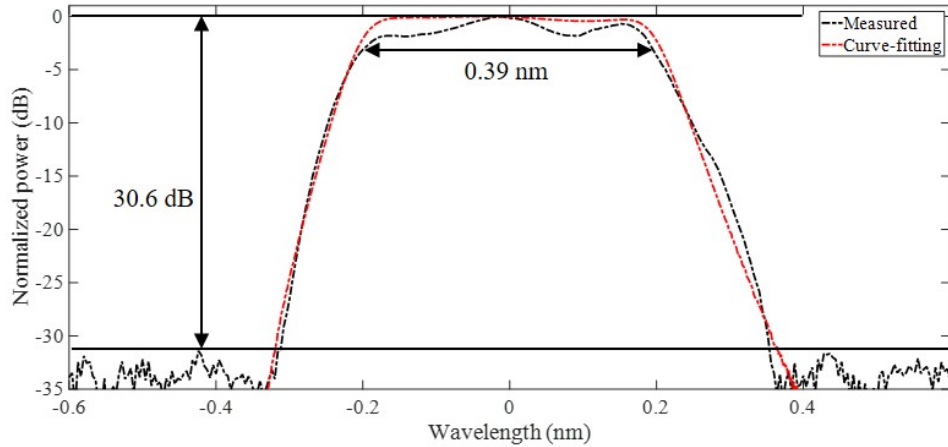


Figure 5.10: Measured spectrum (black dash trace) of the MZI-MRR filter optimized for 50 GHz bandwidth centered at 1551 nm. Red dash trace is the fitting curve performed to extract the coupling parameters and phase detunes of the device.

We next performed wavelength and bandwidth tuning of the filter by optimizing the transmission spectral response to obtain a 50 GHz bandwidth centered at 1551 nm wavelength. First, we used the bandwidth tuning map (e.g., Fig. 5.7 (a) and (c)) to determine the phase detunes of the four RT resonators, which would yield the 50 GHz bandwidth. These values for RT resonators [1, 2, 3, 4] were determined to be $[-0.065, 0.15, 0.065, -0.15]$ rad, which, given a resonator FSR of 8.1 nm FSR, correspond to resonance wavelength detunes of $[-0.084, 0.193, 0.084, -0.193]$ nm from the center

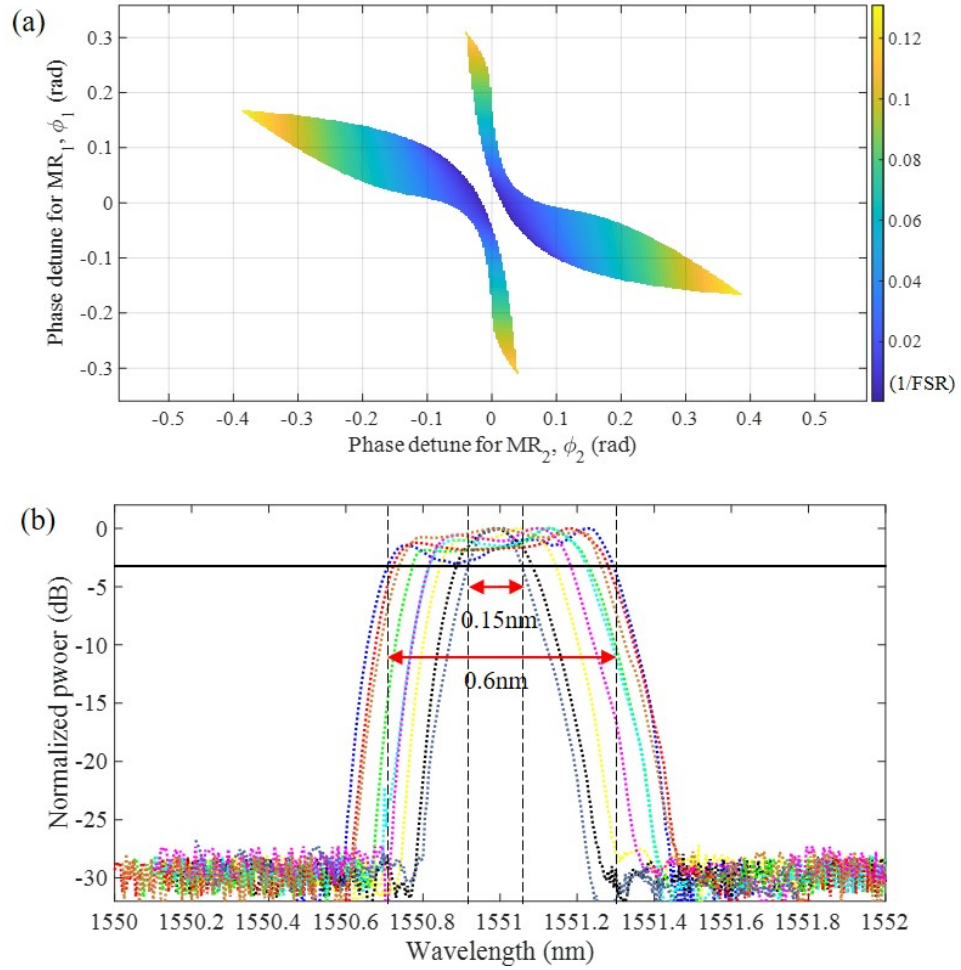


Figure 5.11: (a) Tuning map for the 3-dB bandwidth as functions of the phase detunes of RTs 1 and 2 for maximum 3 dB ripple, based on the coupling coefficients calculated from the measured spectrum in Fig. 5.10. Plots are in the unit of $1/\text{FSR}$. (b) Measured filter spectra tuned to different bandwidths from 0.15 nm to 0.6 nm, each spectrum is normalized to the maximum power collected from all spectra.

wavelength of 1551 nm. Since the initial resonance wavelengths of the four RTs were [1550.01, 1550.88, 1550.87, 1550.32] nm, we calculated the heat powers required to tune the four resonators to be [13.30, 4.44, 8.21, 20.54] mW. We also optimized the phase shifter of the top MZI arm by applying 48.4 mW to the heater to maximize the in-band transmission and minimize the out-of-band transmission power.

The optimized filter response is shown by the black dash line in Fig. 5.10. We obtained a 3dB bandwidth of 0.39 nm or 48.7 GHz, which are fairly consistent with the

designed values. The in-band ripple was measured to be 1.9 dB. We also performed curve fitting to the spectra (shown by the red dash line), which yielded coupling coefficients of [0.40, 0.25, 0.40, 0.25] for the 4 RTs, which are all smaller than the designed values. The insertion loss is estimated to be 2 dB, and fitted phase detunes of 4 RTs are [-0.074 0.167 0.095, -0.156]. We note the detunes are all larger than designed values, indicating that the smaller coupling coefficients require larger detunes to realize a designed bandwidth. We also note that the out-of-band rejection level is a little over 30 dB, which is limited mainly by the TM polarization noise from the input laser. Such noise could be further suppressed by having a polarization beam splitter (PBS) [103] at the input port to filter out the TM polarization.

The bandwidth of the filter could be varied by repeating the above optimization process for the desired 3dB bandwidth. Fig. 5.11(a) shows the estimated bandwidth variation based on the calibrated coupling coefficients. For a $\epsilon_m = 3$ dB, a maximum of bandwidth tuning range is 0.01 to 0.12, which is 0.09 - 0.97 nm for our device. Fig. 5.11(b) shows the optimized filter spectra for various bandwidth settings between 0.15 nm and 0.6 nm, corresponding to a 4-fold increase in the minimum bandwidth setting. We observe that the inband ripple increases as the bandwidth increases, but the roll-off slope remains relatively unchanged over the entire bandwidth tuning range. We note that for small bandwidth settings, the wavelength detunes of the 4 RTs are very close to 0 from the center wavelength, which requires more precise thermal control to achieve narrow passbands. Accurate thermal tuning is also necessary to equalize the in-band ripples and obtain more symmetric spectral responses. We expect that with more precise heater control, the spectral performance could be further improved, and the bandwidth tuning range could be further extended.

5.4 Summary

In this chapter, we proposed a new universal VBW filter based on the MZI-MRR architecture. The most distinct advantage of the proposed filter architecture is that it can be used to realize any (even) filter order. The bandwidth can be varied by simply tuning the microring resonances. We also mathematically proved that the insertion loss does not increase during bandwidth tuning. We also experimentally demonstrated a 4th-order MZI-MRR silicon photonic filter with bandwidth tunable from 0.15 nm to 0.6 nm with a maximum inband ripple of 3 dB. The RT resonators were tuned using microheaters, while their resonance frequencies could be tracked through the built-in *pin* junctions operated in reverse bias. We note that the MZI-MRR spectral performance depends critically on the accuracy of resonance detunes by the heaters. Thus future work should focus on improving the heater control stability and thermal tuning process to enhance the filter spectral response and maximize the bandwidth tuning range.

Chapter 6

Enhanced Responsivity in All-Silicon Photodetection for Optical Monitoring

As photonic integrated circuits increase in complexity [104][105], it becomes critical to monitor the optical signals at various nodes in the circuit, which ensures robust network operation [106]. Active optical power monitoring typically requires the detection of the optical signals using on-chip integrated photodiodes (PDs). However, since silicon has a bandgap energy corresponding to 1.1 μ_{ph} m wavelength, Si PDs based on single-photon absorption have very low detection efficiency in the telecommunication wavelength window (1.5 - 1.6 μ m). Thus, high-efficiency silicon-based PDs typically require Ge or Ge on silicon (GeSi) [107][108], all of which require a different material (Ge) or additional processing steps (hybrid integration of different materials) to fabricate. It is also possible to fabricate III-V semiconductor PDs (such as InGaAs [109][110] and InGaAsP [111][112]) on silicon but the large lattice mismatch (8.1% between III-V material and Si) significantly lowers the yield and quality of the devices. On the other hand, Si PDs based on two-photon absorption (TPA) do not require extra fabrication steps beyond the standard CMOS process and are thus more cost-effective to incorporate into Si PICs. However, due to the small TPA coefficient of Si around 1550nm wavelength, these devices have much lower responsivity than Ge based PDs, limiting their application. For this reason, very little work on

TPA-based Si PDs has been reported. Liang et al.[113] reported a straight waveguide Si photodetector with an estimated responsivity of only 1.8 mA/W for a input of 60 μ W optical power at 1.5 μ m wavelength. By incorporating Si PDs into a microdisk resonators, Chen *et al.* [114] was able to enhance the responsivity through optical resonance and achieved a value of 10 mA/W at 100 μ W continuous-wave (CW) optical power. The same group also demonstrated Si PD based on TPA in a microring resonator, although the reported responsivity was much lower, at 0.25 mA/W for 120 μ W input optical power [115]. By comparison, the responsivities of Ge based PDs are around 1A/W [116], which is two orders of magnitude higher than values achieved so far for Si PDs based on TPA.

This chapter investigates all-silicon photodetection based on TPA and avalanche effects and explores ways to achieve high responsivity in TPA-based Si PDs. We first investigate Si microring *pin* photodetectors (MR PDs), whose responsivity is enhanced by optical resonance. In particular, we propose two methods for further enhancing the responsivity. In the first scheme, we explore the bistability behavior of the MR PD to obtain a photocurrent response curve with a steep slope, which provides gain to the small-signal responsivity (SSR). We obtained an SSR as large as 180 mA/W, representing almost 10 times enhancement over direct detection of the optical signal by the same MR PD. In the second scheme, by exploiting the fact that the responsivity of a TPA PD increases with optical power, we can achieve large SSR by applying an optical bias to the MR PD. Using this scheme with the optical bias and signal tuned to two adjacent microring resonances, we could achieve an SSR of 141 mA/W. Both schemes can thus provide at least an order of magnitude improvement in the responsivity of small-signal detection compared to values previously reported for microdisk and microring Si PDs based on TPA [114] [115]. Besides, we also explore the avalanche mechanism in a p^+pn^+ junction, which enables the further responsivity enhancement to $> 1A/W$ at only 100 μ W input optical power. Such a responsivity is comparable to the responsivities of commercial GeSi PDs. The device and techniques

presented in this chapter have potential applications not only for wavelength channel monitoring but also amplitude demodulation, heterodyne detection and correlation measurements.

The rest of this chapter is organized as follows. Section 6.1 investigates the design, implementation, and experimental results of Si *pin* MR PD. Section 6.2 presents the performance and characteristics of Si p^+pn^+ MR PD under the avalanche condition. The chapter is summarized in Section 6.3.

6.1 Silicon Microring *pin* Photodetectors

Fig. 6.1(a) shows a schematic of a Si microring *pin* PD, which consists of a 20 μm -radius microring resonator evanescently coupled to a straight rib waveguide through a gap of 300nm. The microring waveguide is also a rib waveguide with an embedded *pin* junction, whose cross-section is shown in Fig. 6.1(b). The device is implemented on an SOI substrate consisting of a 220 nm-thick Si layer on a 2 μm -thick SiO_2 layer. The rib waveguide is designed for TE polarization operation, with a core width of 500nm, rib height of 130nm and slab thickness of 90nm. The *pin* junction consists of a 1.7 μm -wide intrinsic region (10^{10} cm^{-3} *p*-type concentration) centered over the rib waveguide core. The *p* and *n* type regions have doping concentrations of $2 \times 10^{20} \text{ cm}^{-3}$ and $5 \times 10^{20} \text{ cm}^{-3}$, respectively. Contacts made to *p* and *n* regions are separated by 5 μm . An image of the fabricated device is shown in Fig. 6.1(c). At the edge of the chip, the straight waveguide is tapered to a width of 200nm for butt-coupling with lensed fiber.

Fig. 6.2(a) shows the measured TE transmission spectrum of the microring resonator at zero bias voltage around the 1545.3nm resonance wavelength. The spectrum has a 3-dB bandwidth of 56 pm and a free spectral range ($\Delta\lambda_{FSR}$) of 5.3 nm. By performing curve fitting to the measured spectrum, we extracted the power coupling coefficient and linear propagation loss of the microring to be $\kappa^2 = 6.5 \%$ and

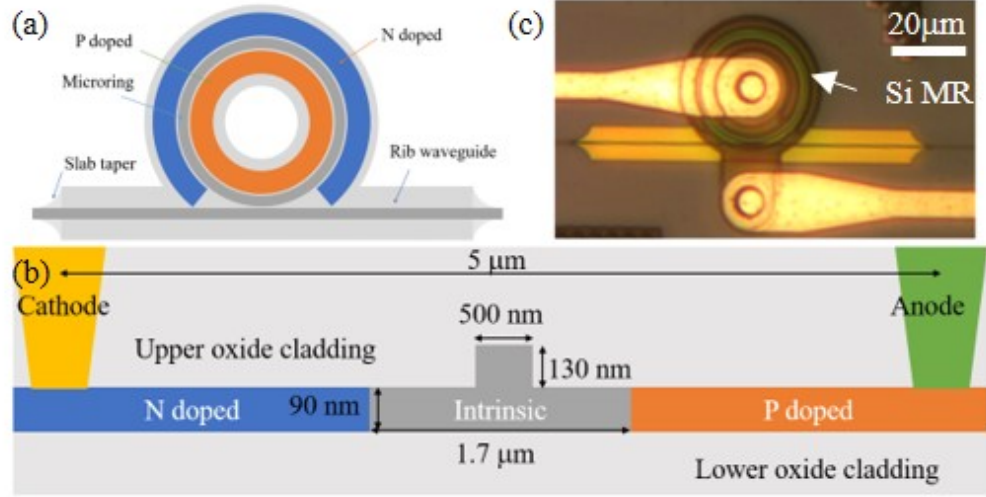


Figure 6.1: (a) Schematic of the Si microring photodetector. (b) Cross-section of the *pin* junction rib waveguide on a Silicon-on-Insulator substrate. (c) Microscope image of a fabricated device.

$\alpha_L = 4.1$ dB/cm, respectively. These values correspond to a Q-factor of 3.26×10^5 and maximum intensity enhancement of 43 times at the resonance. We also note that the microring is over-coupled. Ideally, to achieve maximum responsivity, it is preferable to operate the MR PD under critical coupling condition where the intensity enhancement is the highest. However, due to free carrier absorption (FCA), the loss in the microring increases with input optical power. To compensate for this power-dependent increase in loss, we designed the microring resonator to be initially over-coupled so that the resonator became closer to critical coupling when an input optical power was applied. For the *pin* junction embedded in the microring, the dark *i-v* characteristic with no input light is shown in Fig. 6.2(b), from which we obtain a dark current of 100 pA at 0 V bias 138 pA at -15 V reverse bias for the PD.

6.1.1 Response of *pin* MR PD to Single-Wavelength Input

We first characterized the response of the PD to a single CW laser light input tuned to the 1545.3 nm resonance of the microring. Fig. 6.3(a) and (b) show the transmitted optical spectra for different input optical powers P_{in} at bias voltage of -15 V and 0

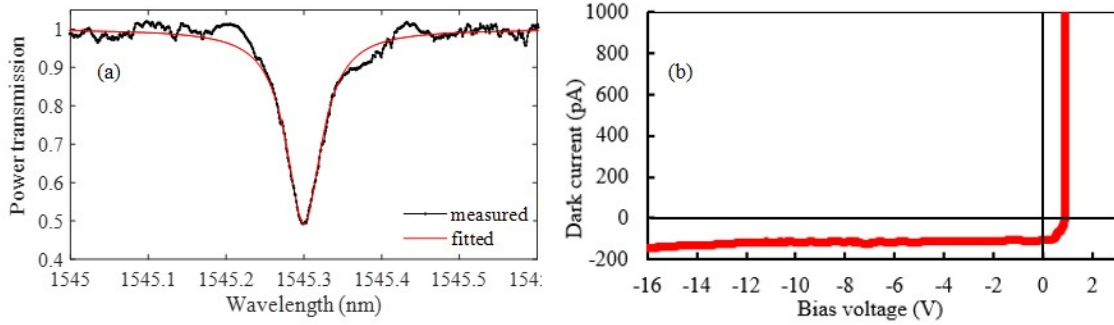
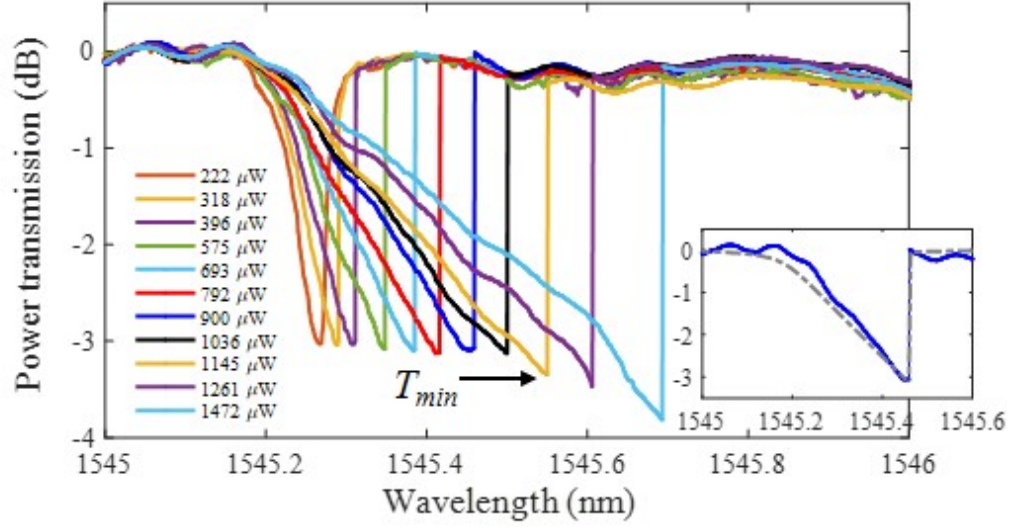


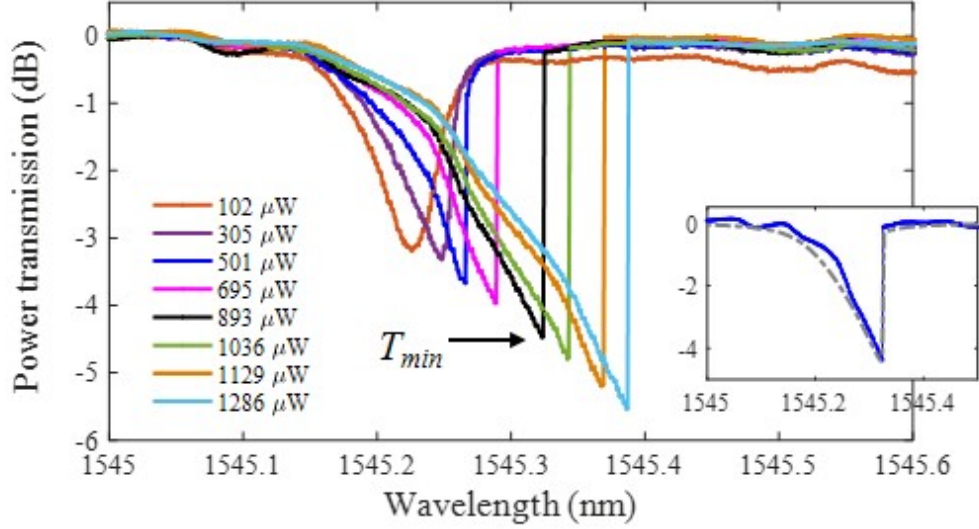
Figure 6.2: (a) Measured transmission spectrum of the MR PD around the 1545.3 nm resonance wavelength at 0 V bias. (b) Dark I-V curve of the PD.

V, respectively. In both plots we observe significant skewing of the resonance spectra at high input powers which is indicative of bistable behavior. This is predominantly caused by two opposing nonlinear effects arising from the TPA-generated free carrier density: a negative change in the refractive index of the silicon core due to free carrier dispersion (FCD) and a positive change in the index due to the thermo-optic effect accompanying free carrier absorption (FCA). The net red shift observed in the resonance spectra indicates that the latter is the dominant effect. We also note that for the spectra at -15 V bias, the minimum power transmission T_{min} does not change appreciably with the input power below 1 mW, indicating that FCA does not have a significant impact on the spectral response at lower powers. On the other hand, the transmission spectra at 0 V bias show a steadily decreasing T_{min} with increasing input power. Since the microring resonator is initially over-coupled, a deeper extinction in the resonance spectrum implies an increase in loss due to FCA, which is caused by a larger FC density in the waveguide at 0 V bias compared to -15 V bias for similar input power. This is expected since the steady-state FC density is proportional to the FC lifetime in the waveguide, and the effect of the reverse bias is to reduce the FC lifetime in the waveguide leading to smaller FC density at -15 V bias.

Since the photocurrent depends on the power in the microring, we need a nonlinear model to accurately predict the power in the microring for a given input power and wavelength. To accomplish this, we model the net phase shift in the microring due



(a)



(b)

Figure 6.3: Power transmission spectra of the MR PD for different input powers P_{in} at (a) -15 V reverse bias and (b) 0 V bias. Insets show the measured (solid curves) and computed spectra (dashed curves) at $P_{in} = 900 \mu\text{W}$ for (a) and $P_{in} = 893 \mu\text{W}$ for (b).

to both FCD and FCA-induced thermo-optic effects using the empirical relation:

$$\Delta\phi_{NL} = C_{\phi} P_r^{\eta_{\phi}}(\lambda) \quad (6.1)$$

where P_r is the power in the microring, C_{ϕ} is the effective nonlinear phase coefficient, and η_{ϕ} indicates the power-law dependence. We also account for the nonlinear loss

in the microring due to TPA and FCA using a similar relation:

$$\alpha_{NL} = C_\alpha P_r^{\eta_\alpha}(\lambda) \quad (6.2)$$

where C_α and η_α are parameters to be determined. The power in the microring in the presence of nonlinear phase shift and nonlinear loss is given by:

$$P_r(\lambda) = \frac{P_{r,max}}{1 + F \sin^2[(\Delta\phi_L + \Delta\phi_{NL})/2]} = g_{opt} P_{in} \quad (6.3)$$

where

$$P_{r,max} = \frac{\kappa^2}{(1 - \tau\alpha_{rt})^2} P_{in} \quad (6.4)$$

is the peak of the power spectrum in the microring. In the above expression, $\tau = \sqrt{(1 - \kappa^2)}$ is the transmission coefficient of the coupling junction, $\Delta\phi_L = -2\pi\Delta\lambda/\Delta\lambda_{FSR}$ is the linear phase detune from a resonance, $\alpha_{rt} = \exp[-(\alpha_L + \alpha_{NL})\pi R]$ is the roundtrip field attenuation, $F = 4\tau\alpha_{rt}/(1 - \tau\alpha_{rt})^2$ is the contrast factor of the resonator, and g_{opt} is the intensity enhancement factor or optical gain of the microring. At the output of the MR PD, the optical power transmission is given by:

$$\frac{P_{out}}{P_{in}} = \frac{T_{min} + F \sin^2[(\Delta\phi_L + \phi_{NL})/2]}{1 + F \sin^2[(\Delta\phi_L + \phi_{NL})/2]} \quad (6.5)$$

where the minimum power transmission T_{min} is:

$$T_{min} = \frac{(\tau - \alpha_{rt})^2}{(1 - \alpha_{rt})^2} \quad (6.6)$$

Assuming that the transmission coefficient τ remains unchanged with input power, we can calculate α_{rt} , and hence the nonlinear loss coefficient α_{NL} , directly from the measured T_{min} for each input power using (6.6) as:

$$\alpha_{rt} = \frac{\tau + \sqrt{T_{min}}}{1 + \tau\sqrt{T_{min}}} \quad (6.7)$$

From Eq.(6.3) we also see that the minimum power transmission occurs at the linear phase detune $\Delta\phi_{L,min} = -\phi_{NL}$. The corresponding power in the microring obtained

from Eq.(6.5) is $P = P_{r,max}$. By relating the linear phase detune to the shift in the resonance wavelength, we obtain:

$$\Delta\lambda_{L,min} = \frac{\Delta\lambda_{FSR}}{2\pi} C_\phi P_{r,max}^{\eta_\phi} \quad (6.8)$$

The above relationship allows us to determine the nonlinear phase coefficient C_ϕ and the exponent η_ϕ by simply measuring the change in the resonance wavelength (where the minimum dip occurs in the spectrum) as a function of $P_{r,max}$, which can be calculated from the input power using Eq. (6.6)

In Fig. 6.4(a) we plot the nonlinear loss coefficient α_{NL} calculated from T_{min} of each spectrum in Fig. 6.3 as a function of $P_{r,max}$. We see that at 0V bias, the nonlinear loss closely follows a quadratic dependence on the power in the microring. This nonlinear behavior is expected since the FCA-induced loss varies linearly as the steady-state FC density N_{fc} , which in turn depends quadratically on the optical power. On the other hand, the loss coefficient at -15 V bias remains close to zero until $P_{r,max} \approx 40$ mW (corresponding to $P_{in} \approx 1$ mW), beyond which α_{NL} begins to rise with the optical power. This behavior suggests that at high reverse bias voltages, FCA is negligible for input power < 1 mW since free carriers are swept away from the waveguide core by the applied DC field. In Table 6.1 we summarize the model fitting parameters C_α and η_α for the nonlinear loss at 0 V and -15 V bias voltage. The units of P_r and α_{NL} in the model Eq. (6.4) have been assumed to be mW and μm^{-1} , respectively.

Bias	$C_\alpha^{(*)}$	$\eta_\alpha^{(*)}$	C_ϕ	η_ϕ	γ_{ph}	μ_{ph}
0 V	$1.614e-4$	2	$1.016e-4$	1.345	$5.8949e-8$	1.9678
15 V	$1.702e-4$	2	$2.986e-6$	1.731	$7.0594e-8$	1.9495

Table 6.1: Extracted nonlinear model parameters of MR PD. (*) C_α and η_α for -15 V bias voltages are valid for input power greater than 1 mW.

To determine nonlinear dispersion in the MR PD, we show in Fig. 6.4(b) the logarithmic plots of $\Delta\phi_{L,min}$ vs. $P_{r,max}$ for 0 V and -15 V bias voltage. We observe that both plots exhibit linear relationships, which allow us to perform linear curve

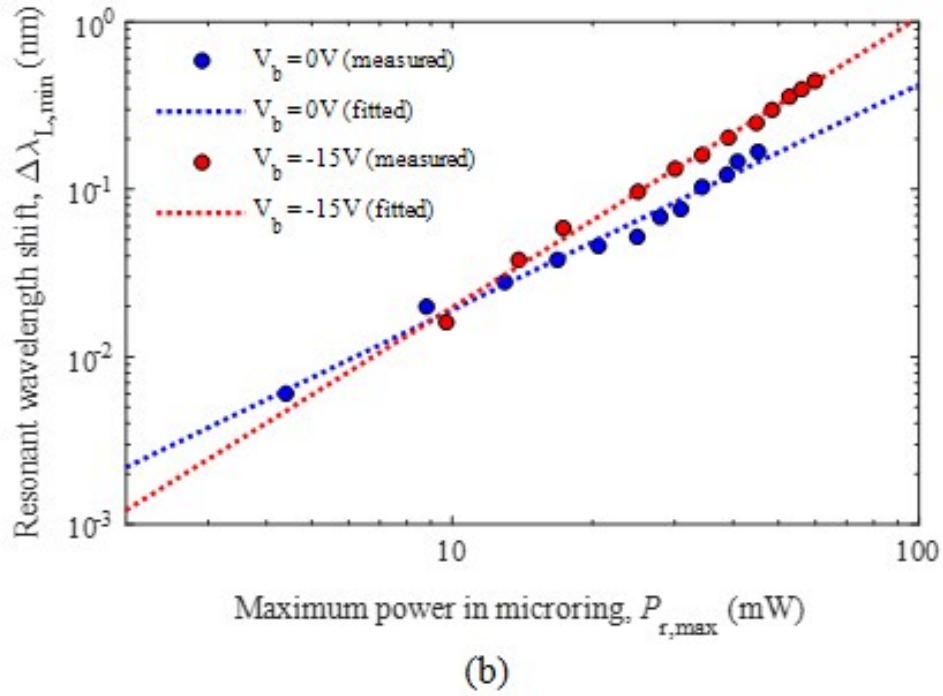
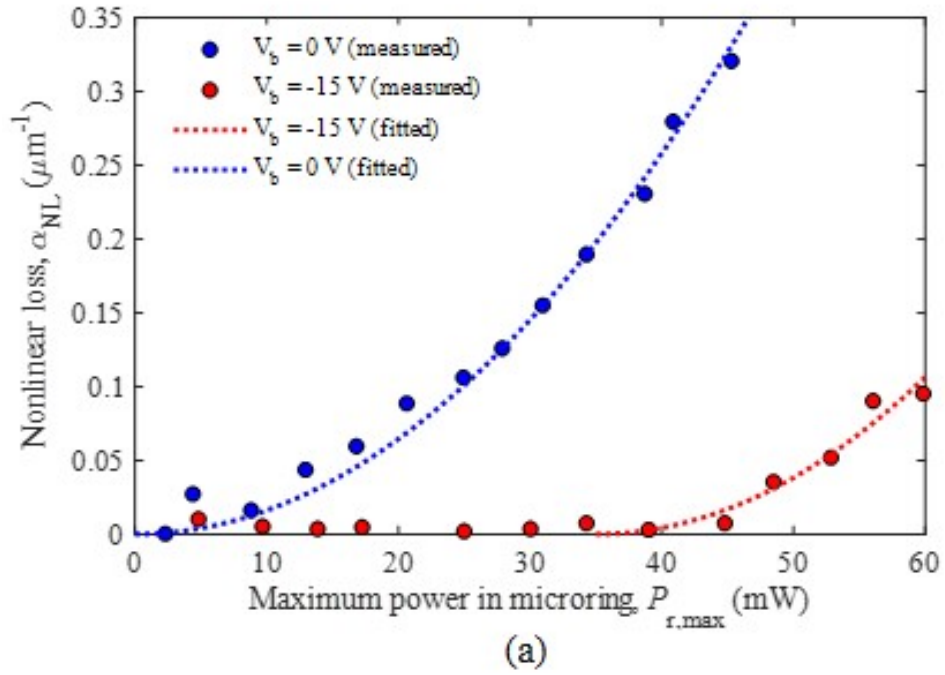


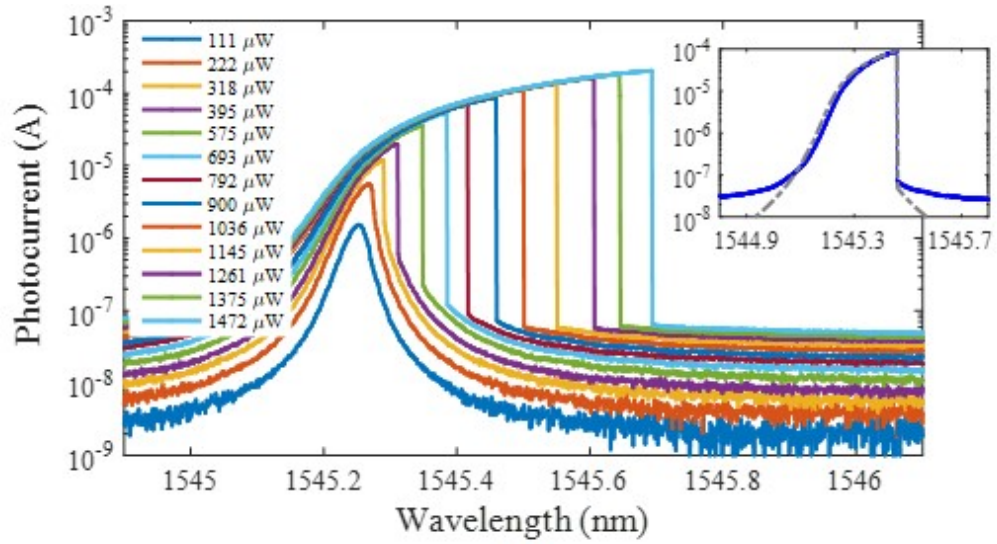
Figure 6.4: Plots of (a) nonlinear loss coefficient in the microring and (b) shift in the resonant wavelength of the microring transmission spectra as functions of the maximum power in the microring at 0 V and -15 V reverse bias voltage.

fits to extract the values for C_ϕ and η_ϕ . The results are also shown in Table 6.1, with the units of P_r and ϕ_{NL} in Eq. (6.3) assumed to be mW and radian, respectively. We note that the exponent η_ϕ in our empirical model in Eq. (6.3) is in general not an integer since the net nonlinear phase shift is due to a combination of FCD and FCA-induced thermo-optic effects, each of which has a different power-law dependence on the optical power. Also, the wavelength shift $\Delta\lambda_{L,min}$ and exponent η_ϕ at -15 V bias are higher than the values for 0 V bias, implying that the FCA-induced thermo-optic effect has a larger impact on the nonlinear phase shift at high reverse bias. This thermo-optic effect is itself due to joule heating associated with the diffusion current and the drift current through the *pin* junction. As the reverse bias voltage is increased, the drift current also increases, which causes more joule heating and hence the larger phase shift observed at -15 V bias compared to 0 V bias. Using the extracted nonlinear model parameters and the microring parameters, we computed the transmission spectra at various input powers using Eq. (6.7). The results for $P_{in} = 900 \mu\text{W}$ at -15 V bias and $P_{in} = 893 \mu\text{W}$ at 0 V bias are shown in the insets in Fig. 6.3(a) and (b), respectively. Good agreement between the computed spectra and measured spectra can be seen, which confirms the validity of our MR PD model. We also note that while both nonlinear dispersive and absorptive effects are present in the MR PD, the bistability behavior observed is predominantly of the dispersive nature, since non-saturable absorption of the type described by Eq. (6.5) by itself does not result in absorptive bistable behavior [117].

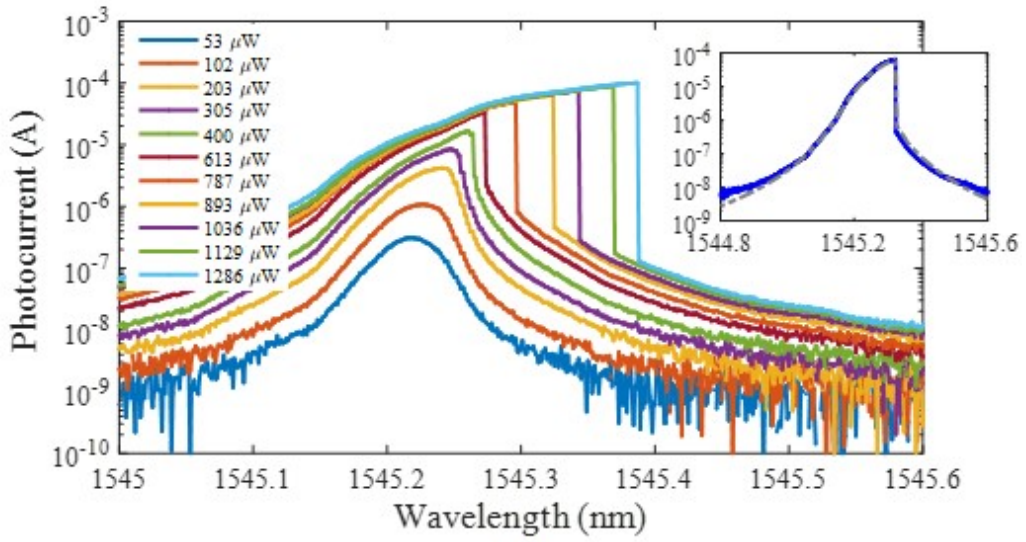
The nonlinear microring model allows us to accurately determine the optical power spectrum in the microring, which is then used to predict the photocurrent generated by TPA. In particular, the dependence of the photocurrent I_{ph} on the optical power P_r in the microring can be modeled by the equation:

$$I_{ph}(\lambda) = \gamma_{ph} P_r^{\mu_{ph}}(\lambda) \quad (6.9)$$

where $\mu_{ph} \approx 2$ indicates the power-law dependence. The coefficient γ_{ph} can be related



(a)



(b)

Figure 6.5: Photocurrent spectra of the MR PD for different input powers P_{in} at (a) -15 V reverse bias and (b) 0 V bias. Insets show the measured (solid curves) and computed spectra (dashed curves) at $P_{in} = 900 \mu\text{W}$ for (a) and $P_{in} = 893 \mu\text{W}$ for (b).

to the TPA coefficient β_{TPA} as follows. The FC generation rate, dN_{fc}/dt , due to TPA is given by [118]:

$$\frac{dN_{fc}}{dt} = \frac{\beta_{TPA}}{2\hbar\omega} \left(\frac{P_r}{A_{eff}}\right)^2 \quad (6.10)$$

where \hbar is the reduced Planck's constant, ω is the light frequency and A_{eff} is the effective overlap area between the microring waveguide mode and the intrinsic region of the *pin* junction. If we approximate the photocurrent from the FC generation rate as:

$$I_{ph} \approx eA_{eff}L \frac{dN_{fc}}{dt} \quad (6.11)$$

where e is the elementary charge and L is the microring circumference, then combining Eqs. (6.10) and (6.11) gives:

$$\gamma_{ph} = \frac{e\beta_{TPA}}{2\hbar\omega} \frac{L}{A_{eff}} \quad (6.12)$$

Figs. 6.5(a) and (b) show the photocurrent spectra measured for different input powers P_{in} at -15 V and 0 V bias voltage, respectively. We note that the peak photocurrent, $I_{ph,max}$, in each spectrum occurs at the corresponding peak power in the microring, $P_{r,max}$, and the relationship between them can be modeled by Eq. (6.11). Indeed, as shown by the logarithmic plots of $I_{ph,max}$ vs. $P_{r,max}$ in Fig. 6.6(a) for both -15 V and 0 V bias voltages, strong linear correlations are observed for both sets of data, which allow us to perform linear curve fit to extract the parameters γ_{ph} and μ_{ph} . The results are shown in Table 6.1, where the units of I_{ph} and P_r in Eq. (6.11) are assumed to be A and mW, respectively. We note that the value of the exponent μ_{ph} is very close to but slightly less than the ideal quadratic dependence characteristic of the TPA process. This small discrepancy could be due to uncertainty in the experimental determination of the nonlinear roundtrip loss, which is used to calculate $P_{r,max}$ in Eq. (6.6). Using Eq. (6.14) and the experimentally determined values for γ_{ph} , we calculated the value for the TPA coefficient to be $\beta_{TPA} = 4.6$ cm/GW, which is within the same order of magnitude as values reported in the literature (≈ 1.1 cm/GW) [119]. We also observe from Fig. 6.6(a) that the relationship between the

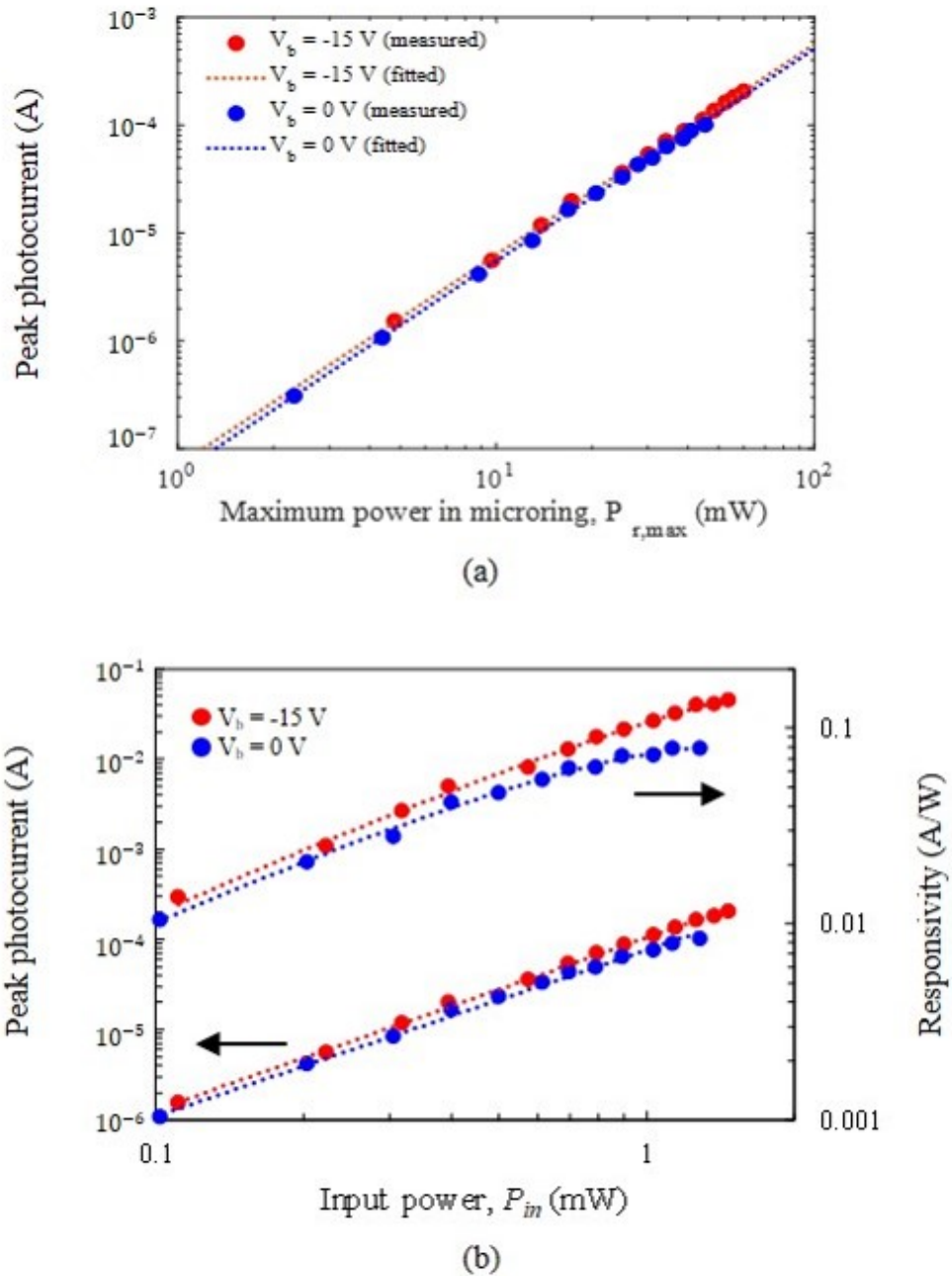


Figure 6.6: (a) Plots of the peak photocurrents of the MR PD as functions of the peak optical power in the microring at -15 V reverse bias voltage and 0 V bias voltage. (b) Plots of the peak photocurrent and responsivity of the MR PD as functions of the input optical power at -15 V and 0 V bias voltage.

photocurrent and optical power in the microring is not strongly influenced by the bias voltage since the rate of TPA-induced electron-hole pair generation does not depend on the bias voltage. To validate our photocurrent response model, we computed the

photocurrent from the optical power spectrum in the microring using the extracted parameters γ_{ph} and μ_{ph} . The results for input power $P_{in} = 900 \mu\text{W}$ at -15 V bias and $P_{in} = 893 \mu\text{W}$ at 0V bias are plotted in the insets in Figs. 6.5(a) and (b) along with the measured photocurrent spectra. Again, good agreement between our model and measurement can be seen.

In Fig. 6.6(b), we plot the peak photocurrent and the corresponding responsivity of the MR PD (defined as $R_{sb} = I_{ph}/P_{in}$) as functions of the input optical power for both bias voltages. We observe that the peak photocurrents and responsivities are nearly the same for both bias voltages at low input power. However, at high input powers, the photocurrent and responsivity at 0 V bias exhibit slight saturation behavior, which limits further improvement in the responsivity at higher powers. This saturation behavior may be caused by Auger recombination, which has the effect of reducing the effective FC lifetime and hence the FC density in the waveguide at high power. Because of the nonlinear dependence of the TPA-generated photocurrent on the optical power, the responsivity of the PD varies with the optical power. At low optical powers, the responsivity is close to zero, which renders the PD impractical for detecting small optical signals. However, much higher responsivity can be obtained if we operate the device at high input optical powers. For example, at 1.34 mW input power and -15 V bias, the responsivity increases to 154 mA/W, which corresponds to a TPA quantum efficiency of about 25 %. Such high responsivity performance has not been reported to date for Si PDs based on TPA.

It should be noted that the responsivity curves in Fig. 6.6(b) assume that for each input power level at a given wavelength, the resonance spectrum of the MR PD is tuned (i.e., by varying the linear phase detune $\Delta\phi_L$ to compensate for the nonlinear resonance wavelength shift) to give the maximum photocurrent. In a practical application, a more realistic detection measurement is that the linear phase detune $\Delta\phi_L$ is set at a fixed value and the photocurrent is detected as a function of the input power. The responsivity curve in this case takes on the bistability behavior of the

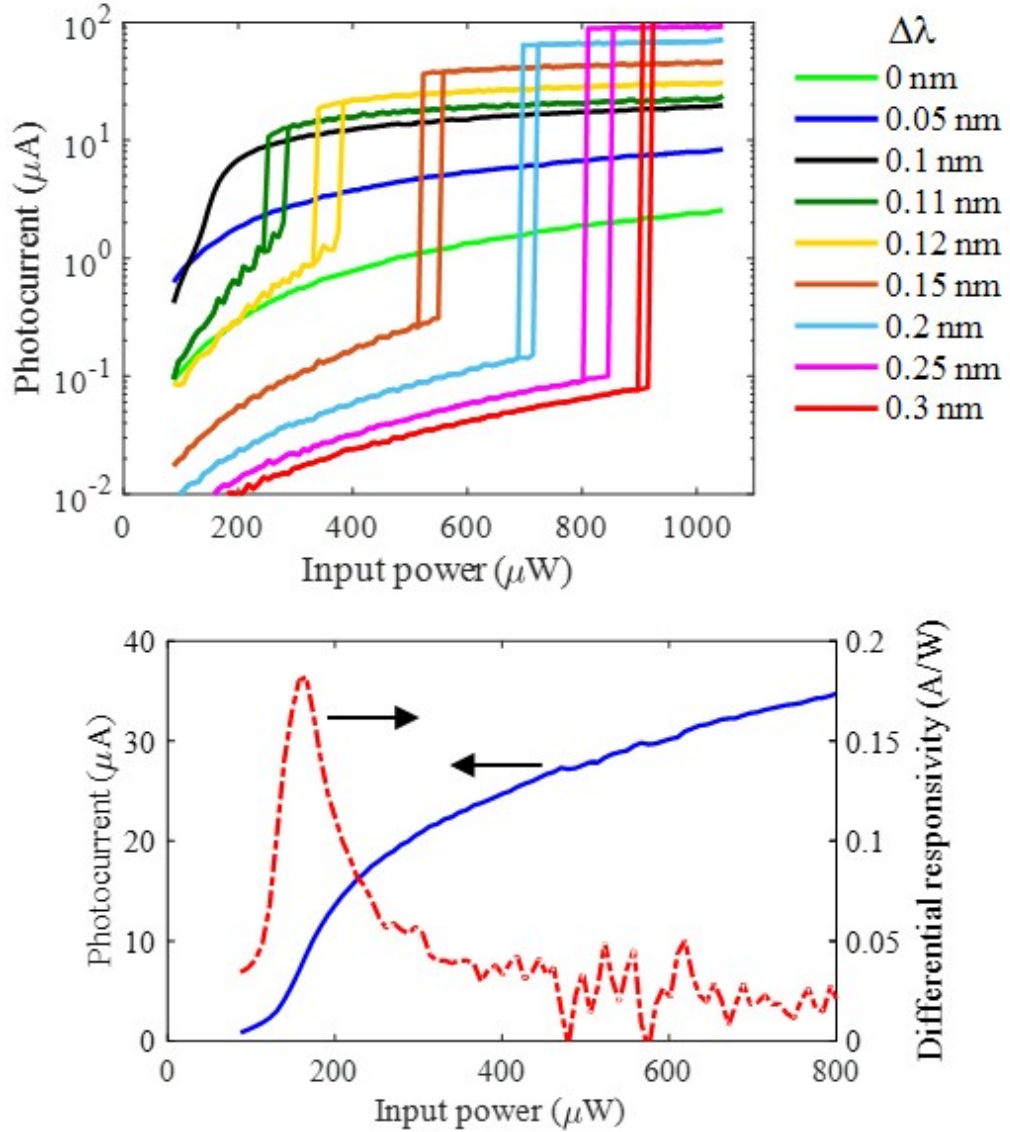


Figure 6.7: (a) Plots of the photocurrent vs. the input optical power at different wavelength detunings $\Delta\lambda$ from the linear resonance and -15 V reverse bias voltage. (b) Photocurrent (solid curve) and differential responsivity (dashed curve) at 0.1 nm wavelength detuning and -15 V reverse bias voltage.

nonlinear resonator as shown in Fig. 6.7(a) for different wavelength detunings $\Delta\lambda$ from the linear resonance at -15 V bias voltage. We observe that for large wavelength detunings $\Delta\lambda$, the photocurrent response curve exhibits a sharp jump between two bistable levels, forming a hysteresis loop as the input power is ramped up and then down. This bistability behavior may be used for binary amplitude demodulation. As

the wavelength detuning is decreased, the hysteresis disappears and is replaced by a single photocurrent response curve with a steep slope. This region can provide large differential responsivity which may be useful for detecting small AC modulations of an optical beam. For example, the photocurrent and small-signal responsivity $R_{ss} = dI_{ph}/dP_{in}$ at 0.1 nm wavelength detuning ($\lambda = 1545.4$ nm) are plotted as functions of the input optical power in Fig. 6.7(b), from which we observe a steep rise in the photocurrent around 165 μ W input power. The SSR at this point peaks at 182 mA/W. By comparison, the photocurrent obtained from direct detection by the MR PD of an input CW signal of 165 μ W power is only 3.4 μ W, giving a responsivity of only 20 mA/W, or 9 times less than the SSR achieved with the bistability curve. This example illustrates how the responsivity of the MR PD can be enhanced by exploiting the nonlinear bistability nature of the device. It is also possible to design the microring resonator to provide even steeper slope and hence higher differential responsivity around the input power level of interest.

6.1.2 Response of *pin* MR PD to Two-Wavelength Inputs

In this section we investigate the use of a second input CW light at a different wavelength to increase the responsivity of the MR PD to small optical signals. The technique is called optical biasing, in which a high-power CW optical beam (the optical bias) at a different resonant wavelength is injected into the microring to move the detection point of a signal beam up the responsivity curve in Fig 6.6(b). The absorption of a photon at the signal wavelength and a photon at the bias wavelength provides the energy needed to create an electron-hole pair to generate the photocurrent. The technique may be used to perform heterodyne detection or correlation between two signals of different wavelengths.

From Eq. (6.11) we can express the photocurrent as a function of the input power as:

$$I_{ph} = \gamma_{ph} g_{opt} P_{in}^2 \quad (6.13)$$

where g_{opt} is the optical gain factor define in Eq. (6.3) and we have set the exponent μ_{ph} to 2. For an optical input consisting of a bias beam with power P_b and a signal beam with power P_s at two different wavelengths, the total average input power is $P_b + P_s$. Assuming that $P_b \gg P_s$, the total photocurrent can be approximated as:

$$I_{ph} = \gamma_{ph}g_{opt}(P_b + P_s)^2 \approx \gamma_{ph}g_{opt}(P_b^2 + 2P_bP_s) \quad (6.14)$$

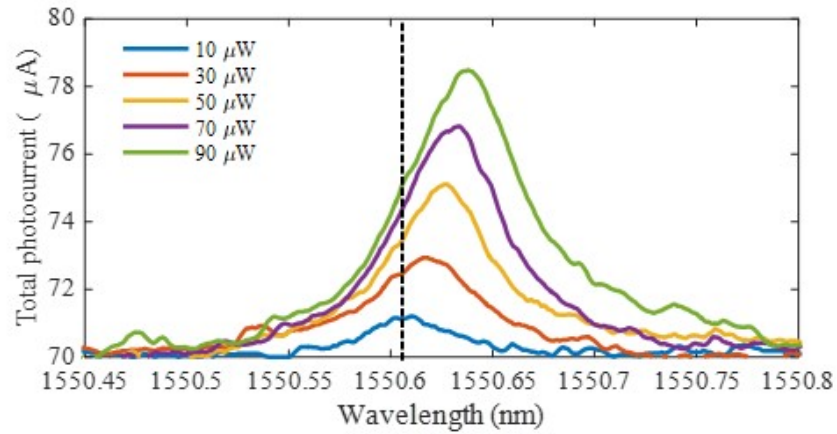
Thus, the photocurrent is the sum of a current due to the bias beam, $I_b = \gamma_{ph}g_{opt}P_b^2$, and a small-signal current due to the signal beam, $I_s = 2\gamma_{ph}g_{opt}P_bP_s$. The responsivity associated with the signal beam detection is:

$$R_{ss} = \frac{I_s}{P_s} = 2\gamma_{ph}g_{opt}P_b = 2R_{sb} \quad (6.15)$$

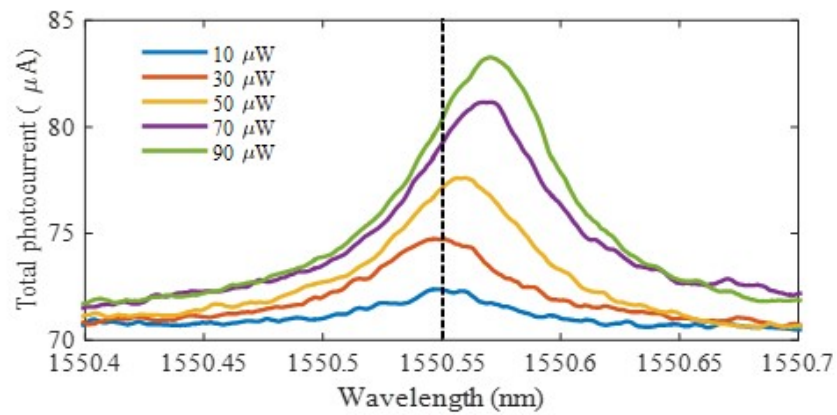
where $R_{sb} = I_b/P_b$ is the single-beam responsivity. Thus, the SSR is enhanced by two times with respect to the single-beam responsivity and is independent of the signal power. However, we note that Eq. (6.17) is only valid for small signal powers since it ignores the nonlinear phase shift caused by large signal powers.

To demonstrate the two-wavelength photodetection scheme, we used a CW bias beam tuned to the 1545.3 nm resonance and a CW signal beam tuned to the next resonance around 1550.5 nm of the microring. The polarization of each beam was individually adjusted to TE. The two beams were combined via a 3-dB coupler and coupled to the input waveguide of the MR PD. The power of the optical bias was set at 1 mW and, in order to compensate for the nonlinear phase shift, the wavelength of the bias beam was slightly blue detuned from the linear resonance of the microring. The bias photocurrent I_b was measured to be 70.9 μ A at 0 V bias and 70.3 μ A at -15 V bias, both corresponding to a single-beam responsivity of 75 mA/W. With the signal power set in the 10- 100 μ W range, we then scanned its wavelength across the microring resonance around 1550.5 nm. The small-signal photocurrent I_s was obtained by subtracting the total detected photocurrent by the bias current I_b .

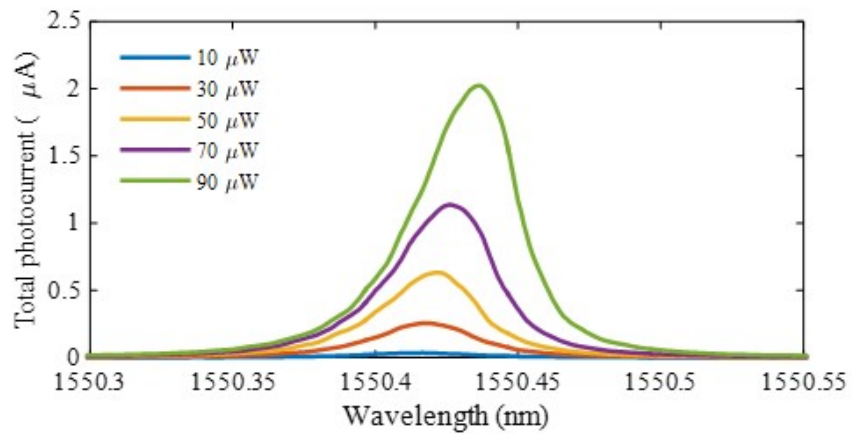
Figs. 6.8(a) and (b) show the total photocurrent spectra measured for different optical signal powers at -15 V bias and 0 V bias, respectively. For comparison, we



(a)



(b)



(c)

Figure 6.8: Plots of the total photocurrent spectra at different signal powers for (a) - 15 V bias and 1 mW optical bias, (b) 0 V bias and 1 mW optical bias, (c) 0 V bias and 0 mW optical bias. Dashed lines indicate the center wavelengths of the spectra at 10 μW signal power.

also show in Fig. 6.8(c) the photocurrent spectra obtained at 0 V bias and without any applied optical bias power ($P_b = 0$ mW). We observe that the spectra in all three cases remain fairly symmetric, although the applied optical bias caused the spectra to be slightly red shifted and their bandwidths slightly broadened compared to the case with no optical bias. In addition, there is a small red shift in the current spectra with increasing signal power at the resonance wavelength. To compare the responsivity

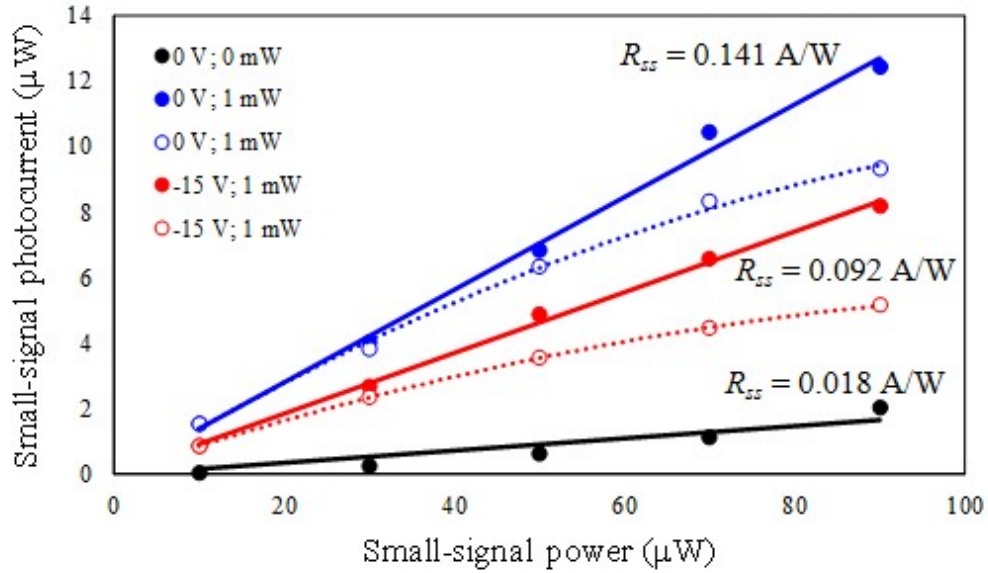


Figure 6.9: Plots of the small-signal photocurrent vs. the signal power for different optical bias powers and electrical bias voltages. The filled circles represent the peak values of the photocurrent spectra whereas the unfilled circles represent the photocurrent at a fixed wavelength indicated by the dashed lines in Fig. 6.8(a) and (b).

performance of the three cases, we plotted in Fig. 6.9 the peak photocurrent vs. the signal power, as well as the photocurrent detected at a fixed signal wavelength indicated by the dashed lines in Fig. 6.8. These wavelengths correspond to the peak of the photocurrent spectra at small signal power ($10 \mu\text{W} - 90 \mu\text{W}$) in each case. We observe that the relationships between the peak photocurrent and the signal power are fairly linear, from which we obtain small-signal responsivities of 92 mA/W and 141 mA/W for 1 mW optical bias at -15 V bias and 0 V bias, respectively. For comparison,

the estimated responsivity for the case of neither optical bias nor reversed bias is only 18 mA/W. These results demonstrate the potential of significantly enhancing the responsivity of small signal detection by optical biasing. However, due to the small nonlinear red-shift in the resonance spectrum with increasing signal power, the small-signal photocurrent shows saturation behavior for input signal powers above 40 μ W, which limits the linear dynamic range of the detector.

We note that with an optical bias applied, the small-signal responsivity at 0 V bias ($R_{ss} = 141$ mA/W) is roughly twice that of the single-beam responsivity at the bias point ($R = 75$ mA/W). This is consistent with our model prediction in Eq. (6.17). On the other hand, the small-signal responsivity at -15 V bias ($R_{ss} = 92$ mA/W) is only slightly higher than the single-beam responsivity ($R = 75$ mA/W). The lower small-signal responsivity at -15 V bias can be explained by the fact that the signal power causes a larger nonlinear shift in the optical power spectra than at 0 V. This shift has the effect of reducing the optical power in the microring, resulting in smaller change in the photocurrent for the same increment in the signal power.

6.2 Silicon Microring p^+pn^+ Avalanche Photodetectors

In this section, we investigate the operation of an MR PD under avalanche condition as a way to further enhance the responsivity of all-Si based PDs. The aim is to achieve responsivity of TPA-based photodetection above 1 A/W, which is comparable to the performance of Ge and Ge-Si PDs. In recent years, all-silicon avalanche photodiodes (APDs) have gained much attention due to their large ionization coefficients and ease of integration with CMOS electronics. Common APDs [120][14][121][122] use pn junctions in different geometries (e.g., zigzag [14], interleaved [121], and asymmetric [122]) and centered on the waveguide core region to maximize absorption of the incoming photons. However, a main concern of the pn junction is the trade-off

between the signal-to-noise ratio (SNR) and the avalanche gain, where a high gain is obtained at close to the breakdown voltage, but a tremendous amount of noise current is also triggered. Here we propose to separate the absorption region and the multiplication region (SAM) design[123], which will contribute to reducing the dark current noise while still maintaining a high avalanche gain. Our Si APD consists of a p^+pn^+ junction embedded in an MR, where the pn^+ junction is formed to further enhance the responsivity by avalanche. Measurement results show a responsivity as large as 1.25 A/W was obtained at 2.87mW input power at 15 V reverse bias voltage. In addition, due to the large thermo-optic nonlinearity in the MR APD, we first observed a thermo-optic resonance shift of ≥ 1 FSR by simply tuning the input optical power. Finally, the time response of the bistability switching of p^+pn^+ MR APD is measured at the level of nanoseconds.

6.2.1 Design of Silicon Microring Avalanche Photodetector

Our p^+pn^+ MR APD has a similar geometry to the pin MR PD described in the last section (Fig. 6.1), except the central region is replaced by a lightly p -doped region. The p -region is 1.7 μm wide and centered over the rib waveguide core, with a doping concentration of $3 \times 10^{17} \text{cm}^{-3}$. The p^+ and n^+ regions are heavily doped with doping concentrations of $2 \times 10^{20} \text{cm}^{-3}$ and $5 \times 10^{20} \text{cm}^{-3}$, respectively. Fig. 6.10(a) shows the measured TE transmission spectrum of the MR APD at 0 V bias around the 1522.5 nm resonance. The spectrum has a 3-dB bandwidth of 105 pm (or 13 GHz) and an FSR of 4.89 nm. By performing curve fitting to the measured spectrum, we extracted the power coupling coefficient and linear propagation loss of the microring to be $\kappa^2 = 6.9 \%$ and $\alpha_L = 3.03 \text{ dB/cm}$. This propagation loss is much higher than the pin MR PD and can be attributed to the increased FCA in the p -doped region of the waveguide core. At 0 V bias, the microring has a Q-factor of 14,500 and intensity enhancement of 11.8 times at resonance. Fig. 6.10(b) shows the dark current vs. the reverse bias voltage of the p^+pn^+ junction embedded in the MR

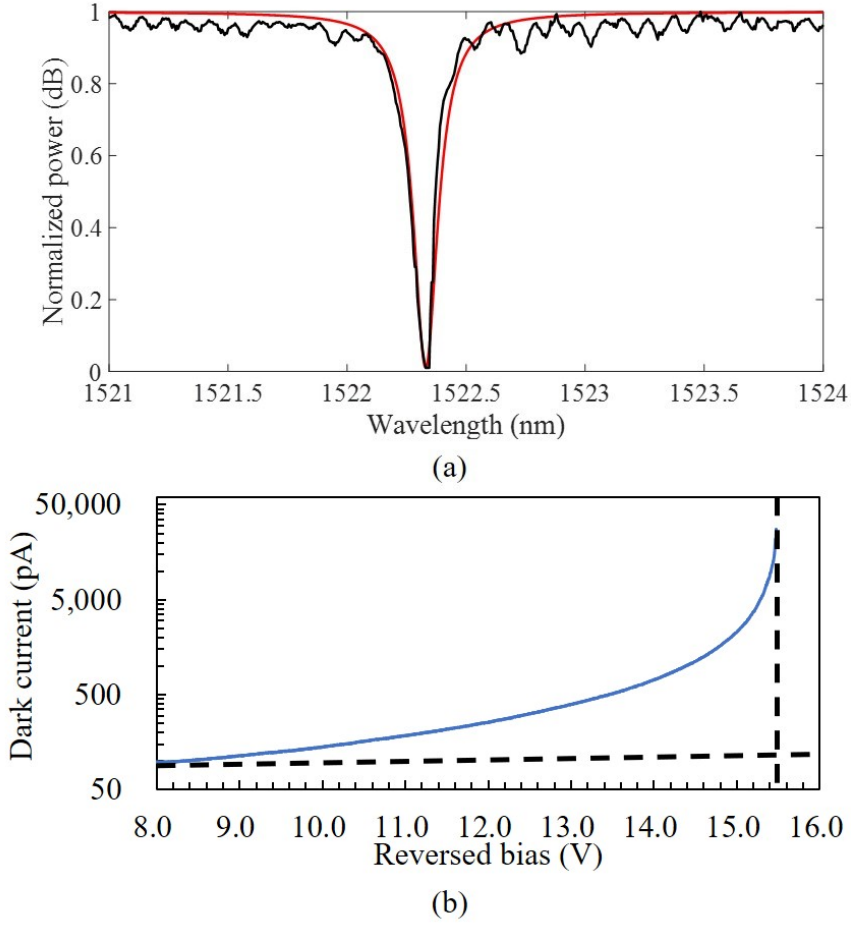


Figure 6.10: (a) Measured transmission spectrum of the MR APD around the 1522.35 nm resonance wavelength at 0 V bias. (b) Dark current of p^+pn^+ junction in MR APD as function of the reverse bias voltage.

APD. We observe that the dark current remains low (~ 80 pA) until 15.5 V, when it increases significantly, indicating the onset of impact ionization. Thus, we define the avalanche-mode operation of our p^+pn^+ MR APD to be around 15 V. We estimate the depletion width from the formula

$$W_d = \sqrt{\frac{2\epsilon V}{q} \left(\frac{1}{N_a} + \frac{1}{N_d} \right)}, \quad (6.16)$$

where $\epsilon = 1.03 \times 10^{-12}$ F/cm is the permittivity of silicon, V is the bias voltage on the junction, $q = 1.602 \times 10^{-19}$ C is the electron charge, and N_a and N_d are the acceptor and donor doping concentrations in cm^{-3} . For one-side abrupt pn^+ junction with $N_a = 3 \times 10^{17} cm^{-3}$ and $N_d = 5 \times 10^{20} cm^{-3}$, the depletion width is 266 nm at

a reverse bias voltage of 15 V, which is near the breakdown voltage of the junction. Thus, the edge of the depletion region at reverse bias voltages up to breakdown will remain in the slab region of the rib waveguide. Our APD thus has the SAM configuration. The photo-generated free-electrons diffuse across the p -doped region to reach the depletion region at the pn^+ junction, where they are accelerated by the high electric field to ionize more electrons and contribute to the output current. The SAM structure helps suppress current noise as random free carriers generated in the absorption region are not accelerated[123].

6.2.2 Responsivity of the MR APD

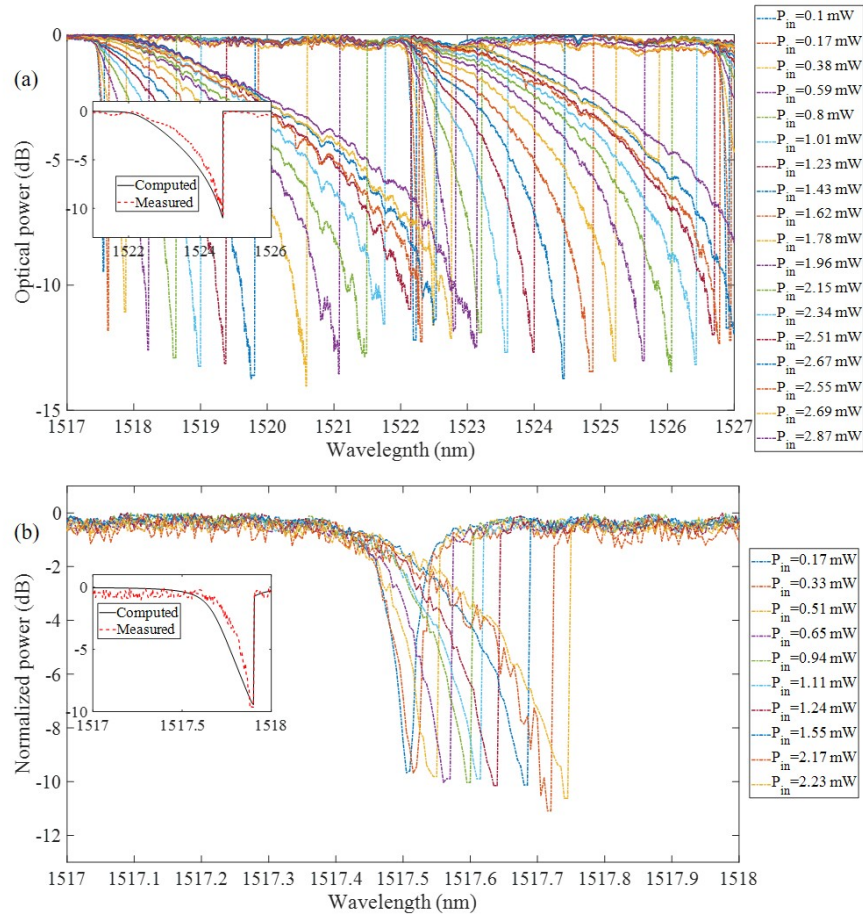


Figure 6.11: Optical transmission spectra of the p^+pn^+ MR APD for various input optical powers at (a) -15 V bias voltage, and (b) 0 V bias voltage. Inset plots show the measured (red dash) and computed spectra (black solid curves) at $P_{in} = 1.38$ mW input power.

We first characterized the response of the p^+pn^+ MR APD to TE-polarized CW laser light tuned to the 1517.5 nm resonance. Figs. 6.11(a) and (b) show the transmitted optical spectra of the device for different input optical powers P_{in} at bias voltages of -15 V and 0 V, respectively. In Fig. 6.11(a), we observe substantial resonance shifts and very strong skewing of the resonance spectra even at very low input powers (e.g., at $P_{in} < 100 \mu W$). The resonance shift and the degree of skewing are much more pronounced than observed in Fig. 6.11(b) for 0 V bias voltage at comparable input optical powers.

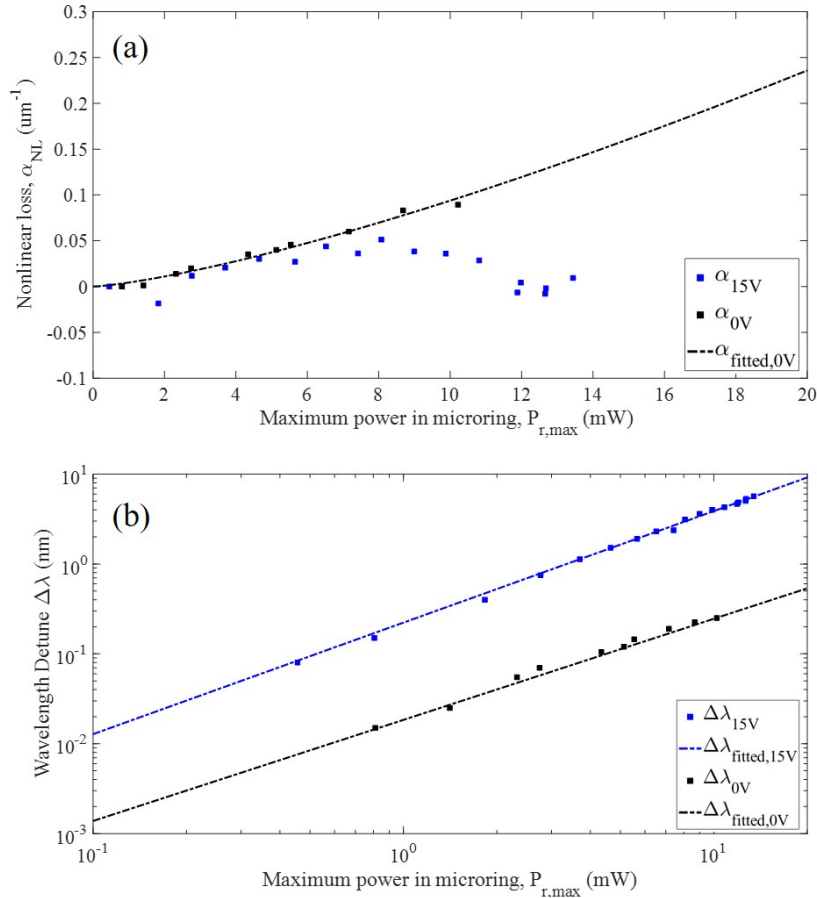


Figure 6.12: Plots of (a) the nonlinear loss coefficient in the MR APD for -15 V and 0 V bias voltages, and (b) nonlinear resonance shift for -15 V and 0 V bias voltages, as functions of the maximum power in the microring.

Due to the doping in waveguide core, photon absorption is contributed not only by the quadratic TPA effect but also largely by the linear defect-state absorption (DSA)

effect. To determine the dependence of the nonlinear phase shift and nonlinear loss on the optical power in the MR, we again assume the models given by Eqs. (6.1) and (6.2). In Figs. 6.12 (a) and (b) we plotted the nonlinear loss coefficient α_{NL} and the resonant wavelength detunes $\Delta\lambda$ vs. the peak power in the MR. By fitting the data with Eqs. (6.1) and (6.2), we extracted the parameters C_ϕ , η_ϕ , C_α , and η_α for 0 and -15V bias voltages and the results are summarized in Table 6.2. We found the nonlinear behaviors of the p^+pn^+ MR APD are similar to the pin MR PD at 0 V except that the nonlinear loss coefficient η_α is reduced from 2 to 1.331, indicating that the linear dependence of defect-state absorption (DSA) from the p -doping dominates over the quadratic dependence of TPA. However, the nonlinear loss is close to 0 and independent of the optical power at -15 V bias. We attribute the different loss behavior by the different absorption mechanisms at 0 V and -15 V bias voltages. Specifically, the loss at 0 V bias voltage is dominated by TPA and DSA, but the loss at -15 V bias voltage is more pronounced by avalanche induced FCA, which does not depend on the optical power. On the other hand, the nonlinear phase has a similar dependence on the optical power at both bias voltages, with the exponent factor η_ϕ close to 1. Again, the net nonlinear phase shift is due to a combination of FCD and joule heating from the generated photocurrent, but predominated by joule heating as the net red-shift is observed. Using the extracted nonlinear model parameters along with the microring parameters, we computed the optical spectrum for 1.4 mW input optical power for both bias voltage and plotted them the result inset Figs. 6.11(a) and (b), good agreement between the measured spectra (dash lines) and the computed spectra (solid lines) can be observed.

Figs. 6.13(a) and (b) show the measured photocurrent spectra corresponding to the optical spectra in Figs. 6.11 at -15 V and 0 V bias, respectively. We define the avalanche gain by comparing the maximum photocurrent of -15 V bias voltage spectrum to that obtained for 0V bias voltage with the same input optical power.

Bias	C_α	η_α	C_ϕ	η_ϕ	γ_{ph}	μ_{ph}
0 V	$4.37e7-3$	1.331	$2.461e-2$	1.135	$7.171e-4$	1.602
15 V	-*	-*	0.4475	1.054	0.1616	1.159

Table 6.2: Extracted nonlinear model parameters of MR APD. (*) C_α and η_α are not valid for -15 V bias voltage.

Using Miller's formula [124]

$$M = (1 - (V/V_b)^n)^{-1}, \quad (6.17)$$

where M is the avalanche gain factor, V is the applied voltage in Volt, V_b is the

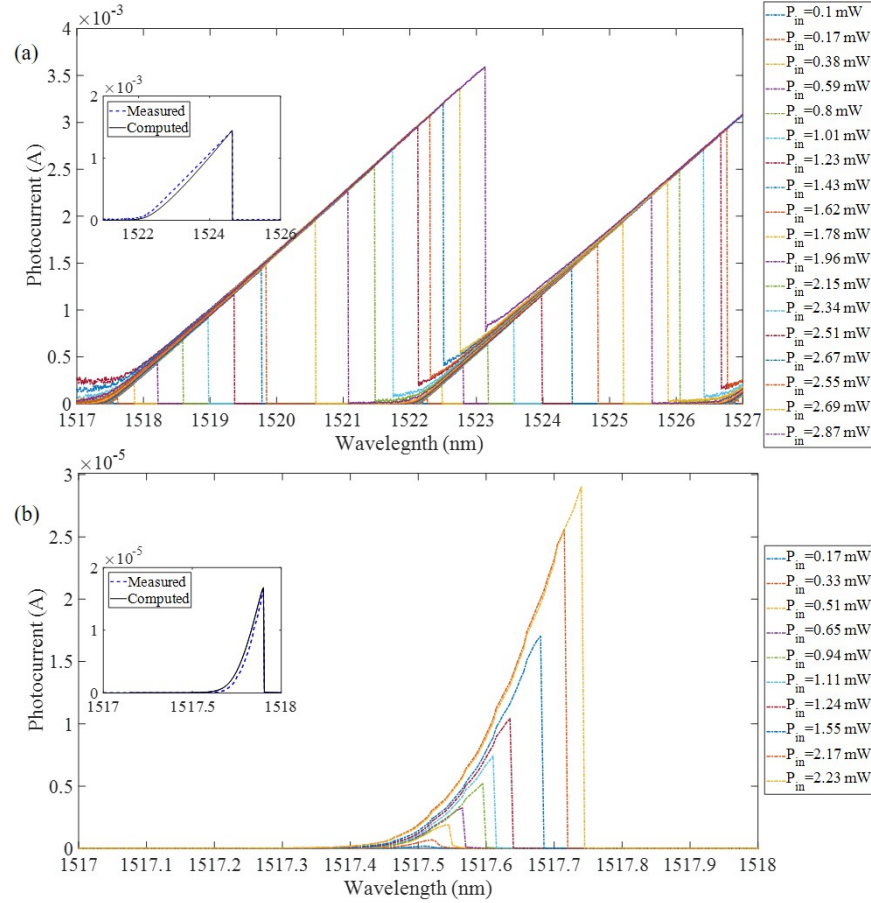


Figure 6.13: Photocurrent spectra for various input optical powers for (a) -15 V bias voltage and (b) 0 V bias voltage. Inset plot shows the measured (red dash curve) and computed (black solid curve) photocurrent spectra at $P_{in} = 1.38$ mW input power.

avalanche breakdown voltage, and exponent factor n is a constant that is 1.5–4 for

silicon [120]. After fitting the experimental data at different optical power, the fitted value of $V_b = 15.3\text{V}$ and $n = 1.85$ is obtained. The calculated V_b is fairly consistent with the breakdown voltage observed in Fig. 6.10(b). For plots in Figs. 6.13(a), we observe that for a fixed input optical power, the photocurrent increases fairly linearly as the wavelength is swept across the MR resonance. This linear dependence is a manifestation of the MR's bistability effect in the presence of strong thermo-optic nonlinearity. In particular, we observe that at high input powers at -15 V bias voltage, the linear increase in the photocurrent extends over more than one FSR of the MR, which implies that the nonlinear phase shift in the MR exceeds 2π . To the best of our knowledge, there has not been any report of nonlinear effect in a microring resonator strong enough to induce a nonlinear wavelength shift exceeding the resonator's FSR. In Fig. 6.14(a) we plot in logarithm the peak photocurrent $I_{ph,max}$ vs the peak power in the MR, $P_{r,max}$, for both -15 V and 0V bias voltages. Similar to Fig. 6.6 for the *pin* MR PD, strong linear correlations are observed for both sets of data, which allows us to perform a linear curve fit based on Eq. (6.9) to extract the parameters γ_{ph} and μ_{ph} . The results are shown in Table 6.2. We note that the exponent factor μ_{ph} of the p^+pn^+ MR APD is significantly less than 2 at both bias voltages. In particular, the photocurrent-optical power relationship is almost linear (e.g., $\mu_{ph} = 1.159$) at -15 V bias, suggesting that the DSA induced photocurrent out-scales the TPA induced photocurrent to be the main avalanche source current. Using the extracted parameters together with the microring parameters, we computed the photocurrent spectra for input optical power $P = 1.38$ mW for both bias voltage (i.e. same conditions as the spectra inset Figs. 6.11) and plotted the results inset Figs. 6.13(a) and (b). Close agreement between the computed and measured spectra can be seen, indicating the validity and accuracy of our photodetector model. To further explore the competition of TPA-induced photocurrent and DSA-induced photocurrent,

we adopt a second-order polynomial model [122]

$$I_{ph} = \gamma_{ph,NL}P_{r,max}^2 + \gamma_{ph,L}P_{r,max} \quad (6.18)$$

where $\gamma_{ph,NL}$ and $\gamma_{ph,L}$ represent the current-dependence coefficient of the TPA and DSA. The quadratic exponent factor is assumed as the coefficient μ_{ph} we extracted for *pin* MR PD is very close to 2. By fitting the polynomial modal with our experiment data, we extract the values of $[\gamma_{ph,NL}, \gamma_{ph,L}]$ to be $[9.69\text{e-}5, 1.64\text{e-}3]$ and $[7.25\text{e-}3, 1.66\text{e-}1]$ for 0V and -15V bias voltages, respectively. From both bias voltage we note that the linear component $\gamma_{ph,L}$ is significantly larger than the nonlinear component $\gamma_{ph,NL}$, indicating that the photocurrent from TPA ($\propto P_{r,max}^2$) negligible, the most of free-carrier generation is sourced by DSA and multiplied by the high electric field afterwards.

From the photocurrent plots in Fig. 6.14(a), we compute the responsivity of the MR APD as $R = I_{ph,max}/P_{r,max}$ and plotted the results as a function of the input optical power in Fig. 6.14(b) for both 0 V and -15 V bias. Compared to the *pin* MR PD, the responsivity of the p^+pn^+ MR APD at -15 V bias voltage is ~ 10 times higher than at comparable optical powers. In particular, responsivity values above 1 A/W can be achieved for optical powers above ~ 1 mW, reaching a value of 1.25 A/W at 2.87 mW optical power. This is comparable to the performance of Ge based PDs and, to our knowledge, such high responsivities have not been observed in all-silicon PDs before.

6.2.3 Bistability Behaviour of p^+pn^+ MR APD

The large photocurrent leads to strong thermo-optic nonlinearity in the MR APD through joule heating. This strong nonlinearity allows us to observe bistable behaviour at very low optical powers (< 0.1 mW) comparing to previously reported work [125][21][126][127]. In Fig. 6.15, we plot the photocurrent at -15 V bias voltage as a function of the input optical power at three fixed resonant wavelength detun-

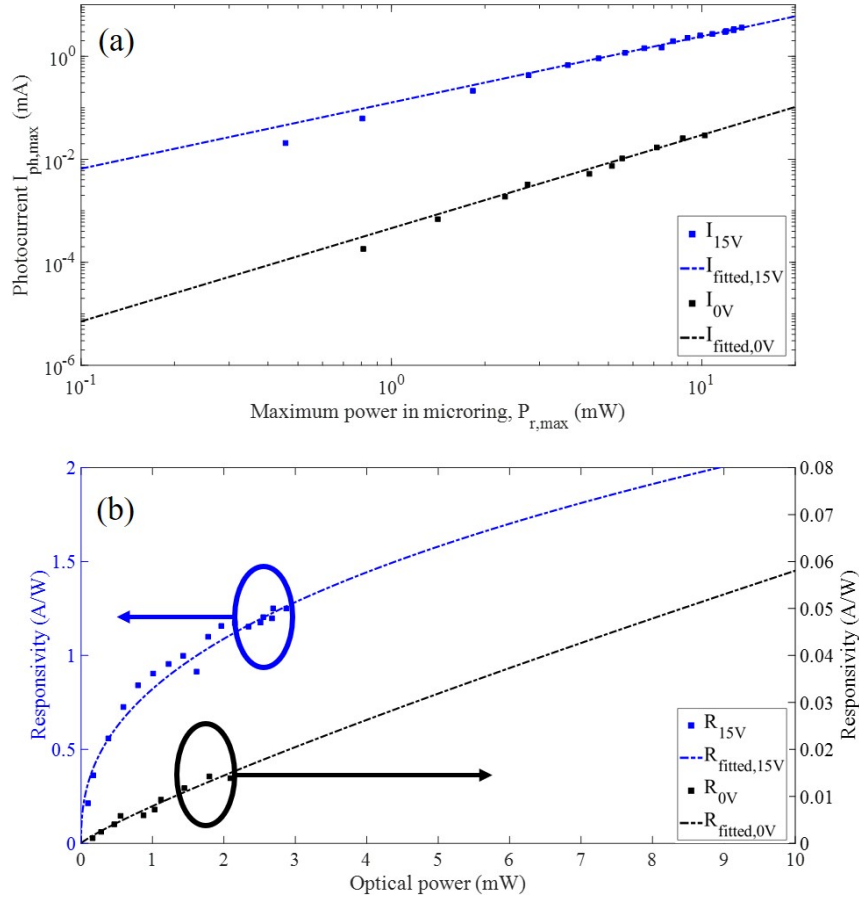


Figure 6.14: Plots of (a) the peak photocurrent of the MR APD as functions of the peak optical power in the microring for -15 V and 0 V bias voltages, (b) responsivities as functions of the input optical power at resonance for -15 V and 0 V bias voltages.

ings $\Delta\lambda$. We observe that for a smaller resonant wavelength detune, lower optical power is required to observe bistability. However, a sharper jump in the photocurrent occurs between two bistable photocurrent levels for larger resonance detune. Such a huge bistable photocurrent behavior may be used for binary amplitude detection. For example, at the linear resonance detune of $\Delta\lambda = 0.3$ nm, the threshold optical input power for the photocurrent response to a binary "1" and "0" are 0.25mW and 0.21mW, respectively. The binary photocurrent output for "1" and "0" are $0.15 \mu\text{A}$ and $197 \mu\text{A}$, which has more than 3 orders of magnitude extinction. Comparing to the *pin* MR PD, p^+pn^+ MR APD provide a much larger photocurrent value (e.g., 10 times larger) at a comparable optical power input (e.g., 0.1 mW). The large photocur-

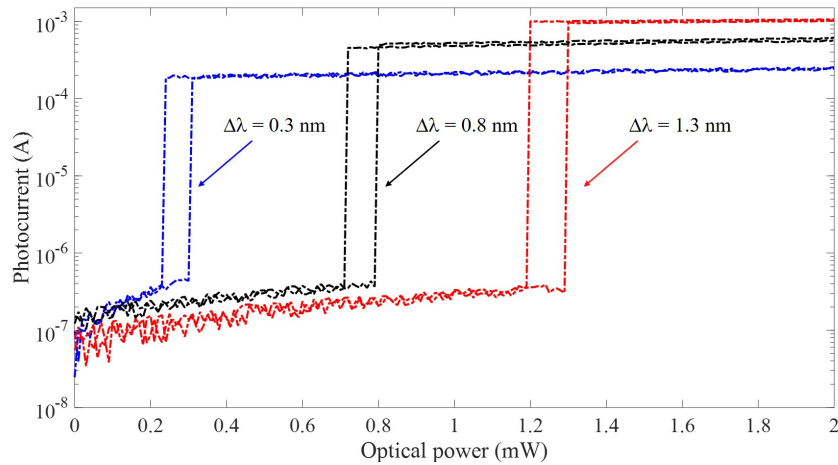


Figure 6.15: Bistable curves of the photocurrent vs. input optical power for different wavelength detunings $\Delta\lambda$ from the linear resonance. All photocurrents are measured at -15 V bias voltage.

rent allows the signal to be directly measured with no need to be amplified, which could effectively reduce the detection noise.

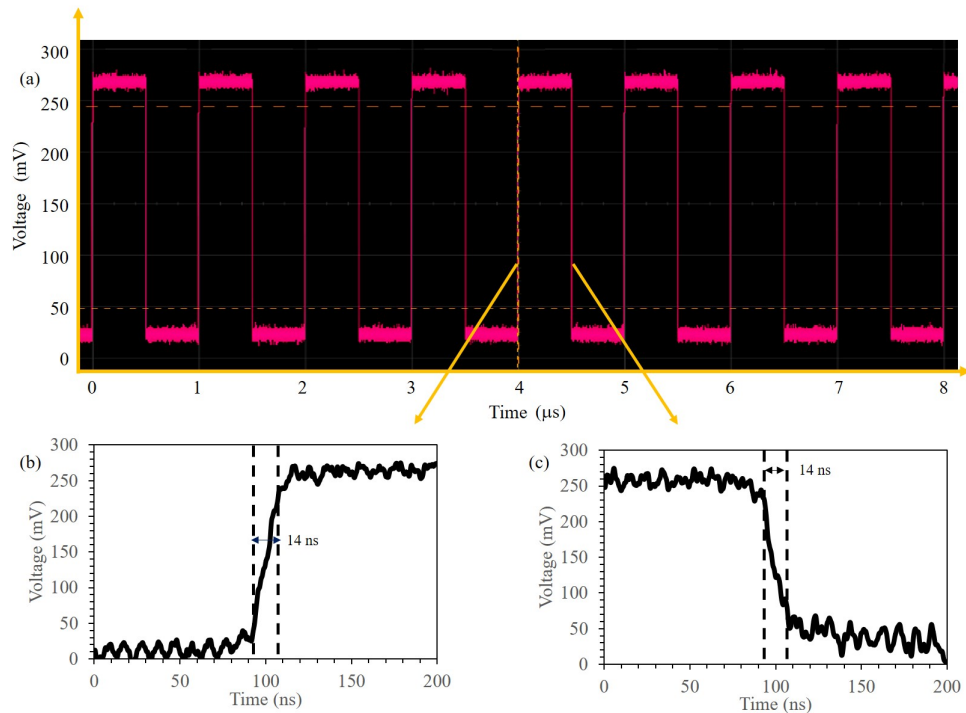


Figure 6.16: (a) Time trace of the photocurrent (converted to voltage) of the p^+pn^+ MR APD for an input optical pulse train. (b) and (c) plot the rise edge and fall edge measured in (a).

We also measured the time response of the MR APD to an amplitude modulated optical signal. A CW optical power at ~ 1 nm detune from the linear resonance wavelength is modulated by a high-speed optical modulator which is electrically driven by a 1 MHz square wave from an arbitrary function generator. The MR APD is biased by -15 V bias voltage. The bistable photocurrent was measured by a high-speed current probe, which was fed to a trans-impedance amplifier (TIA) to convert the photocurrent into a voltage signal. The voltage was finally captured and displayed on an oscilloscope, which is shown in Fig. 6.16 (a). Figs. 6.16(b) and (c) show close-up views of the time response rise and fall edges, where we obtained 14 ns for both rise time and fall time for the MR APD. It should be mentioned that the rise/fall time of our p^+pn^+ MR APD is mainly limited by the performance of our function generator, which has a rise/fall time around 10 ns. To the best of our knowledge, such a fast thermal-bistable switching time response has not been experimentally demonstrated.

6.3 Summary

In this chapter we investigated different ways to enhance the responsivity in all-silicon MR PDs. In the first part, we investigated two approaches for enhancing the SSR of a silicon pin MR PD for detecting small optical signals in the telecommunication wavelength range. The first approach exploits the bistability effect in the nonlinear MR to achieve a photocurrent response curve with a steep slope. The second approach employs an optical bias at a different resonant wavelength to enhance the signal responsivity. We achieved SSRs in the range of 100 – 200 mA/W in both approaches, which represent enhancement factors of almost 10 times over direct detection of small optical signals by the same MR PD. In the second part, we further enhanced the MR PD's responsivity by exploiting the avalanche mechanism in a p^+pn^+ junction biased near avalanche breakdown voltage. A record responsivity of more than 1 A/W was achieved for optical powers ≥ 1 mW, which is comparable to commercial Ge/GeSi

PDs. Due to the large photocurrent generated, the MR APD exhibited strong thermo-optic nonlinearity at an ultra low optical power of ≤ 0.1 mW, enabling the wavelength tuning of more than 1 FSR by just simply applying different optical power into MR PDs. We also note that the responsivity of the MR PDs can be further increased by minimizing loss in the microring to achieve higher intensity enhancement in the resonator, and by optimizing the junction and SOI rib waveguide to maximize the overlap between the optical mode and the absorption region to increase the quantum efficiency.

The MR PD devices and detection methods presented may have potential applications such as optical power monitoring, amplitude demodulation, and heterodyne detection. For example, the narrow linewidth of the microring resonance can be tuned to a channel in a WDM communication system to couple a small fraction of the power for detection while allowing the rest of the signal to pass through with only a small loss. Furthermore, the large difference between the bistable photocurrent levels (e.g., ≥ 1 mA) in p^+pm^+ MR APD can also be used for binary detection [128] with a detection time response of ~ 10 ns. Moreover, by scanning the microring resonance, e.g. with a microheater, the device can serve as a spectrometer to measure the spectral response of channel bandwidth.

Chapter 7

Conclusion and Future Research Directions

7.1 Summary of Research Contributions

Silicon photonics has become the most promising material platform for integrated photonic circuits owing to its high refractive index, low loss, cost-effective fabrication, and compatibility with CMOS integrated circuits. However, several challenges remain which limit the performance of silicon PICs. These include the limited refractive index tuning range from both thermo-optic and FC dispersion effects, and slow thermo-optic response time. On the detection side, the large bandgap of Si (relative to telecommunication wavelengths) prevents efficient PDs based on silicon to be realized in a cost effective manner.

As the demand in data bandwidth continues to grow, silicon PICs for WDM networks and optical interconnects must evolve towards being more flexible to allow for better utilization of network resources. In particular, the operation wavelength needs to be reconfigurable to any arbitrary wavelength grid along with flexible bandwidth settings. Furthermore, the reconfiguration must be fast to avoid network latency and massive cache usage. In this thesis, we have addressed several of these issues by developing flexible and scalable Si PICs that allow for fast adaptations to new network settings, including widely tunable ROADMs, variable bandwidth add/drop filters, and fast wavelength selection for data transmission. In addition, we also in-

investigated novel methods for real time on-chip monitoring of data signals and device performance, namely, by using on-chip thermistors for temperature tracking and all-silicon PDs based on TPA. Specific key contributions of this thesis are summarized as follows:

1. Demonstrated continuous tuning of 4th-order VCMR optical filter with the ± 15 pm of center wavelength tuning accuracy, which is the most accurate to date among microring-based photonic filters. On-chip integrated thermistors were also designed and implemented to indirectly track the microring temperatures and monitor the filter performance.
2. Demonstrated a scalable architecture of a fast WS circuit on SOI using thermo-optically tunable 4th-order DC-VMR filters and *pin* MZ switch. The circuit could select a single wavelength from a wavelength comb with ≥ 25 dB rejection on other wavelength over 32.7 nm wavelength selection range. A best-case selection time of 3 ns is experimentally demonstrated.
3. Proposed a new universal VBW filter design based on the MZI-MRR architecture. The center wavelength, bandwidth and filter order are all proved to be tunable by simply varying the resonant frequencies of the microrings without incurring excess insertion loss. A 4th-order MZI-MRR VBW filter was experimentally demonstrated, achieving a bandwidth tuning range from 20GHz to 80GHz with a maximum in-band ripple of only 3dB. To our knowledge, this represents the widest bandwidth tuning range while maintaining the high-order spectral response of the filter.
4. Demonstrated TPA-based silicon MR PDs with enhanced responsivity around 1.55 μm wavelength. Exploiting bistability effect and using optical biasing technique, we achieved small-signal responsivity close to 200 mA/W in *pin* MR PD, which is 10 times higher than previously achieved in silicon MR PDs. We also

demonstrated a p^+pn^+ MR APD for the SAM regime, which achieved responsivities above 1 A/W for optical powers as low as 1 mW. This performance is comparable to state-of-the-art Ge and SiGe PDs based on single photon absorption. In addition, a response time to the bistable switching photocurrent of about 10 ns was obtained. These devices and techniques expand the range of applications of all-silicon photodetectors to the extent that they could potentially become a key component of future integrated silicon photonics.

We have published parts of our research in the following journals:

1. Y. Ren, D. Perron, F. Aurangozeb, Z. Jiang, M. Hossain and V. Van, “A Continuously Tunable Silicon Double-Microring Filter With Precise Temperature Tracking,” in *IEEE Photonics Journal*, vol. 10, no. 6, pp. 1-10, Dec. 2018. [89]
2. Y. Ren, D. Perron, F. Aurangozeb, Z. Jiang, M. Hossain and V. Van, “Silicon Photonic Vernier Cascaded Microring Filter for Broadband Tunability,” in *IEEE Photonics Technology Letters*, vol. 31, no. 18, pp. 1503-1506, 15 Sept. 2019. [82]
3. Y. Ren and V. Van, “Enhanced Small-Signal Responsivity in Silicon Microring Photodetector Based on Two-Photon Absorption,” in *IEEE Journal of Selected Topics in Quantum Electronics*, vol. 26, no. 2, pp. 1-8, March-April 2020. [21]
4. Y. Ren and V. Van, “Silicon Microring Avalanche Photodetector with Linear Response for Frequency Chirp Applications,” (In progress).
5. Y. Ren and V. Van, “Variable Bandwidth Tunable Filter for Elastic Optical Networks,” (In progress).

We have also presented parts of our research in the following conferences:

6. Y. Ren, D. Perron, F. Aurangozeb, Z. Jiang, M. Hossain and V. Van, “A Continuously Tunable SOI Microring Filter with Temperature Tracking,” 2018 IEEE

Photonics Conference (IPC), Reston, VA, 2018, pp. 1-2. [88]

7. Y. Ren, D. Perron, F. Aurangozeb, Z. Jiang, M. Hossain, and V. Van, “Broadband-Tunable Cascaded Vernier Silicon Photonic Microring Filter with Temperature Tracking,” in Optical Fiber Communication Conference (OFC) 2019, OSA Technical Digest (Optical Society of America, 2019), paper Tu2J.4. [90]
8. Y. Ren and V. Van, “High-Responsivity Silicon Microring Photodetector Based on Two-Photon Absorption,” 2019 24th OptoElectronics and Communications Conference (OECC) and 2019 International Conference on Photonics in Switching and Computing (PSC), Fukuoka, Japan, 2019, pp. 1-3. [22]
9. Y. Ren, Z. Jiang, and V. Van, “A Fast Silicon Wavelength Selector for Optical Transceiver,” in Asia Communications and Photonics Conference (ACPC) 2019, OSA Technical Digest (Optical Society of America, 2019), paper T2D.5. [55]

In addition, a patent application is in progress for the invention of the new VB MZI-MRR filter:

1. Y. Ren, and V. Van, and Z. Jiang, “Variable Bandwidth Microring Optical Filters by Resonance Tuning,” 86711509US01, 2020 (In progress).

7.2 Recommendation for Future Research

7.2.1 Fast WS Circuit

An immediate future research goal is to reduce the reconfiguration time of fast WS, which is a time interval during which no data transmission is allowed. Therefore, reducing the dead time will be beneficial in terms of avoiding massive cache deployment, which in turn will significantly reduce the cost of building optical networks. We have proposed a fast wavelength selection architecture in Chapter 4 based on thermally

tunable microring filters and *pin* MZ switch in carrier injection mode. However, the circuit operation still relies on pretuning of the filters, which may not be desirable for many applications.

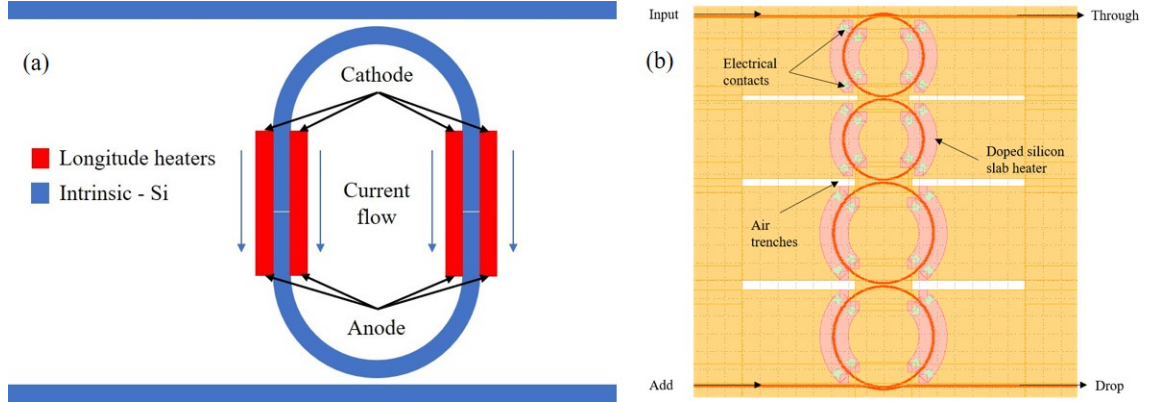


Figure 7.1: (a) Schematic diagram of an ADMR with in-line heater design. The heater is shown in red as the silicon slab on two sides of silicon waveguide. (b) Mask layout of the 4th-order VMR filter with in-line heater designs. The heating part of silicon slab is doped by phosphorus with an average concentration of $n = 5 \times 10^{20} \text{cm}^{-3}$. Air trench is implemented to mitigate the thermal crosstalk.

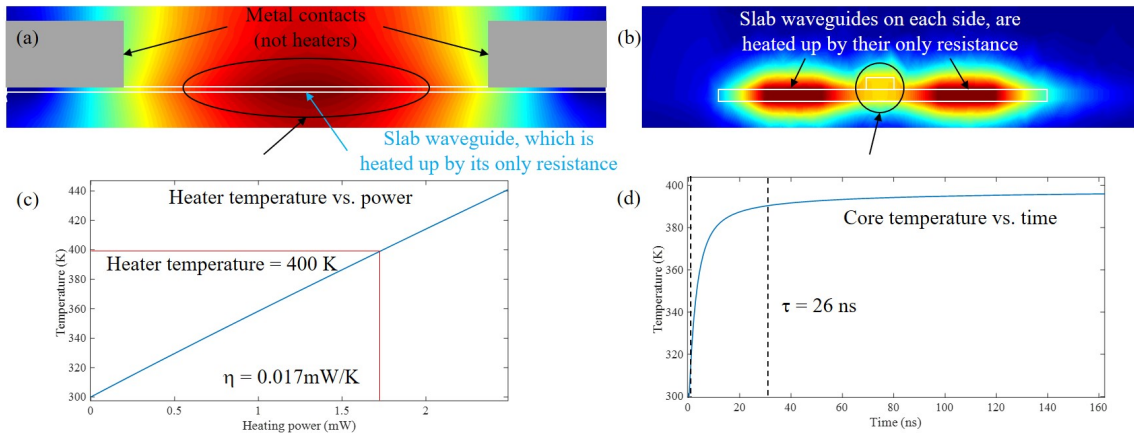


Figure 7.2: Thermal simulations of the in-line heaters: (a) temperature distribution along the length of the slab waveguide, (b) temperature distribution over the waveguide cross section. (c) Plot of the temperature in the silicon waveguide vs. heater power. (d) Rise time response of the in-line heater.

Thus future work could focus on reducing the thermal time constant of thermal tuning. One possible approach is to replace the metal heaters above the silicon waveguide by an in-line heater with doped silicon. As shown in Fig. 7.1(a), the in-

line heater consists of doping two sides of a slab silicon while leaving the rib waveguide core in the middle undoped. Electrodes are connected to the two terminals of the doped region so that the heating current flows along the rib waveguide. The middle undoped region prevents current from flowing across the rib waveguide so that there is no excess loss due to FCA (which is a problem with previous in-line heater designs). To achieve fast tuning, the in-line heaters need to be close to the rib waveguide without interfering with the optical mode propagating in the rib waveguide core. We have simulated the thermal distribution of the in-line heater, which is shown in Fig. 7.2(a) as the temperature distribution along the heater length and in Fig. 7.2(b) as the distribution cross the waveguide. Figs. 7.2(c) and (d) show the thermal tuning efficiency and thermal response time in the waveguide core. We note that both the thermal tuning efficiency and tuning time are significantly improved over metal heaters placed on top of the waveguide. We have also shown in Fig. 7.1(b) a mask layout of a 4th-order Vernier microring add-drop optical filter based on the in-line heater design shown in Fig. 7.1(a). Air trenches are designed between each microrings to prevent thermal crosstalks. Future work will aim to measure and characterize the tuning performance of the device. The new heater design is expected to address the issues of slow tuning speed and high power dissipation of conventional metal heaters. It is also worth noting that the in-line heaters do not need any modification to the silicon photonics fabrication process.

7.2.2 MDM-WDM Hybrid Systems

An extension of the reconfigurable WDM system is to augment it with mode division multiplexing (MDM) to further increase the data bandwidth. Mode-division multiplexing (MDM) offers a new degree of freedom to expand waveguide bandwidth by utilizing the spatial modes of waveguides to carry multiple optical signals simultaneously. In recent years, several promising approaches have been proposed and experimentally demonstrated in mode (de)multiplexing using asymmetric directional

coupling (ADCs) [129], asymmetric Y-junctions [130], and microring based couplers [131], and AWG based WDM-MDM optical filters [132]. However, most of the works so far have only been demonstrated with low-order filters. Therefore, the future work could focus on developing high-order WDM-MDM optical filters with sharp roll-offs and low channel crosstalks which could meet the specifications of practical optical networks.

Bibliography

- [1] D. Nasset, “Pon roadmap,” *J. Opt. Commun. Netw.*, vol. 9, no. 1, A71–A76, 2017.
- [2] K Yamada, Y Urino, T Nakamura, and Y Arakawa, “Integrated silicon-based optical interconnect for fast compact energy-efficient electronic circuit systems,” *NTT Technical Review*, vol. 11, no. 2, 2013.
- [3] W. Bogaerts and L. Chrostowski, “Silicon photonics circuit design: Methods, tools and challenges,” *Laser & Photonics Reviews*, vol. 12, no. 4, p. 1700237, 2018.
- [4] P. Dong, “Silicon photonic integrated circuits for wavelength-division multiplexing applications,” *IEEE Journal of Selected Topics in Quantum Electronics*, vol. 22, no. 6, pp. 370–378, 2016.
- [5] D. Thomson and A. Zilkie, “Roadmap on silicon photonics,” *Journal of Optics*, vol. 18, no. 7, p. 073003, 2016.
- [6] R. H. Khandokar, M. Bakaul, M. Asaduzzaman, A. Nirmalathas, and S. Skafidas, “Performance enhanced butt coupling for effective interconnection between fiber and silicon nanowire,” *IEEE Journal of Quantum Electronics*, vol. 52, no. 9, pp. 1–6, 2016.
- [7] D. Vermeulen, S Selvaraja, P. Verheyen, G Lepage, W Bogaerts, P Absil, D Van Thourhout, and G Roelkens, “High-efficiency fiber-to-chip grating couplers realized using an advanced cmos-compatible silicon-on-insulator platform,” *Optics express*, vol. 18, no. 17, pp. 18278–18283, 2010.
- [8] J. Zhou, J. Wang, L. Zhu, and Q. Zhang, “High baud rate all-silicon photonics carrier depletion modulators,” *Journal of Lightwave Technology*, vol. 38, no. 2, pp. 272–281, 2020.
- [9] S. Zhalehpour, M. Guo, J. Lin, Z. Zhang, H. Sepehrian, Y. Qiao, W. Shi, and L. A. Rusch, “All silicon iq modulator with 1tb/s line rate,” in *2020 Optical Fiber Communications Conference and Exhibition (OFC)*, IEEE, 2020, pp. 1–3.
- [10] L. Zhou, L. Lu, Z. Guo, and J. Chen, “Silicon 16×16 switch matrix based on dual-ring assisted mzi structures with fast and energy efficient switching,” in *2017 IEEE Photonics Society Summer Topical Meeting Series (SUM)*, IEEE, 2017, pp. 35–36.

- [11] T. Zhou, H. Jia, J. Ding, L. Zhang, X. Fu, and L. Yang, “On-chip broadband silicon thermo-optic 2×2 four-mode optical switch for optical space and local mode switching,” *Optics Express*, vol. 26, no. 7, pp. 8375–8384, 2018.
- [12] M Gehl, D Trotter, A Starbuck, A Pomerene, A. Lentine, and C DeRose, “Active phase correction of high resolution silicon photonic arrayed waveguide gratings,” *Optics Express*, vol. 25, no. 6, pp. 6320–6334, 2017.
- [13] J. R. Ong, R. Kumar, and S. Mookherjea, “Ultra-high-contrast and tunable-bandwidth filter using cascaded high-order silicon microring filters,” *IEEE Photonics Technology Letters*, vol. 25, no. 16, pp. 1543–1546, 2013.
- [14] X. Li, Z. Li, X. Xiao, H. Xu, J. Yu, and Y. Yu, “40 gb/s all-silicon photodetector based on microring resonators,” *IEEE Photonics Technology Letters*, vol. 27, no. 7, pp. 729–732, 2015.
- [15] I. Goykhman, B. Desiatov, J. Khurgin, J. Shappir, and U. Levy, “Waveguide based compact silicon schottky photodetector with enhanced responsivity in the telecom spectral band,” *Optics express*, vol. 20, no. 27, pp. 28 594–28 602, 2012.
- [16] J. R. Ong, T. Y. Ang, E. Sahin, B. Pawlina, G. Chen, D. Tan, S. T. Lim, and C. E. Png, “Broadband silicon polarization beam splitter with a high extinction ratio using a triple-bent-waveguide directional coupler,” *Optics Letters*, vol. 42, no. 21, pp. 4450–4453, 2017.
- [17] H. S. Abbas and M. A. Gregory, “The next generation of passive optical networks: A review,” *Journal of Network and Computer Applications*, vol. 67, pp. 53 –74, 2016.
- [18] S. Yoshima, Y. Tanaka, N. Kataoka, N. Wada, J. Nakagawa, and K. Kitayama, “Full-duplex, extended-reach 10g-tdm-ocdm-pon system without en/decoder at onu,” *Journal of Lightwave Technology*, vol. 31, no. 1, pp. 43–49, 2013.
- [19] A. Roshan-Zamir, B. Wang, S. Telaprolu, K. Yu, C. Li, M. A. Seyedi, M. Fiorentino, R. Beausoleil, and S. Palermo, “A 40 gb/s pam4 silicon microring resonator modulator transmitter in 65nm cmos,” in *2016 IEEE Optical Interconnects Conference (OI)*, 2016, pp. 8–9.
- [20] J. Sun, M. Sakib, J. Driscoll, R. Kumar, H. Jayatilleka, Y. Chetrit, and H. Rong, “A 128 gb/s pam4 silicon microring modulator,” in *Optical Fiber Communication Conference Postdeadline Papers*, Optical Society of America, 2018, Th4A.7.
- [21] Y. Ren and V. Van, “Enhanced small-signal responsivity in silicon microring photodetector based on two-photon absorption,” *IEEE Journal of Selected Topics in Quantum Electronics*, vol. 26, no. 2, pp. 1–8, 2020.
- [22] Y. Ren and V. Van, “High-responsivity silicon microring photodetector based on two-photon absorption,” in *2019 24th OptoElectronics and Communications Conference (OECC) and 2019 International Conference on Photonics in Switching and Computing (PSC)*, 2019, pp. 1–3.

- [23] Y. Long and J. Wang, “Ultra-high peak rejection notch microwave photonic filter using a single silicon microring resonator,” *Opt. Express*, vol. 23, no. 14, pp. 17 739–17 750, 2015.
- [24] S. X. Chew, X. Yi, S. Song, L. Li, P. Bian, L. Nguyen, and R. A. Minasian, “Silicon-on-insulator dual-ring notch filter for optical sideband suppression and spectral characterization,” *Journal of Lightwave Technology*, vol. 34, no. 20, pp. 4705–4714, 2016.
- [25] J. Dong, L. Liu, D. Gao, Y. Yu, A. Zheng, T. Yang, and X. Zhang, “Compact notch microwave photonic filters using on-chip integrated microring resonators,” *IEEE Photonics Journal*, vol. 5, no. 2, pp. 5 500 307–5 500 307, 2013.
- [26] L. Xu, W. Zhang, Q. Li, J. Chan, H. L. R. Lira, M. Lipson, and K. Bergman, “40-gb/s dpsk data transmission through a silicon microring switch,” *IEEE Photonics Technology Letters*, vol. 24, no. 6, pp. 473–475, 2012.
- [27] J. Wu, P. Cao, T. Pan, Y. Yang, C. Qiu, C. Tremblay, and Y. Su, “Compact on-chip 1×2 wavelength selective switch based on silicon microring resonator with nested pairs of subrings,” *Photon. Res.*, vol. 3, no. 1, pp. 9–14, 2015.
- [28] O. Tsilipakos, E. E. Kriezis, and S. I. Bozhevolnyi, “Thermo-optic microring resonator switching elements made of dielectric-loaded plasmonic waveguides,” *Journal of Applied Physics*, vol. 109, no. 7, p. 073 111, 2011.
- [29] J. S. Pelc, K. Rivoire, S. Vo, C. Santori, D. A. Fattal, and R. G. Beausoleil, “Picosecond all-optical switching in hydrogenated amorphous silicon microring resonators,” *Opt. Express*, vol. 22, no. 4, pp. 3797–3810, 2014.
- [30] C. Li, J. H. Song, J. Zhang, H. Zhang, S. Chen, M. Yu, and G. Q. Lo, “Silicon polarization independent microring resonator-based optical tunable filter circuit with fiber assembly,” *Opt. Express*, vol. 19, no. 16, pp. 15 429–15 437, 2011.
- [31] M. S. Dahlem, C. W. Holzwarth, A. Khilo, F. X. Kärtner, H. I. Smith, and E. P. Ippen, “Reconfigurable multi-channel second-order silicon microring-resonator filterbanks for on-chip wdm systems,” *Opt. Express*, vol. 19, no. 1, pp. 306–316, 2011.
- [32] R Grover, V Van, T. Ibrahim, P. Absil, L. Calhoun, F. Johnson, J. Hryniewicz, and P.-T. Ho, “Parallel-cascaded semiconductor microring resonators for high-order and wide-fsr filters,” *Journal of Lightwave Technology*, vol. 20, no. 5, p. 872, 2002.
- [33] H. L. Liew and V. Van, “Exact realization of optical transfer functions with symmetric transmission zeros using the double-microring ladder architecture,” *Journal of lightwave technology*, vol. 26, no. 14, pp. 2323–2331, 2008.
- [34] V. Van, “Synthesis of elliptic optical filters using mutually coupled microring resonators,” *Journal of lightwave technology*, vol. 25, no. 2, pp. 584–590, 2007.

- [35] V. Van, “Canonic design of parallel cascades of symmetric two-port microring networks,” *Journal of lightwave technology*, vol. 27, no. 21, pp. 4870–4877, 2009.
- [36] V. Van, *Optical Microring Resonators Theory, Techniques, and Applications*, ser. Series in optics and optoelectronics. CRC Press, 2016, ISBN: 9781466551244.
- [37] B. E. Little, S. T. Chu, H. A. Haus, J. Foresi, and J. Laine, “Microring resonator channel dropping filters,” *Journal of Lightwave Technology*, vol. 15, no. 6, pp. 998–1005, 1997.
- [38] V. Van, “Circuit-based method for synthesizing serially coupled microring filters,” *Journal of Lightwave Technology*, vol. 24, no. 7, pp. 2912–2919, 2006.
- [39] H. Shen, M. H. Khan, L. Fan, L. Zhao, Y. Xuan, J. Ouyang, L. T. Varghese, and M. Qi, “Eight-channel reconfigurable microring filters with tunable frequency, extinction ratio and bandwidth,” *Opt. Express*, vol. 18, no. 17, pp. 18 067–18 076, 2010.
- [40] D. Dai, L. Yu, S. Chen, and H. Wu, “Utilization of thermal effects for silicon photonics,” in *2015 International Conference on Optical Instruments and Technology: Micro/Nano Photonics and Fabrication*, Z. Zhou, C. Zhou, and P. Cheben, Eds., International Society for Optics and Photonics, vol. 9624, SPIE, pp. 1–13.
- [41] C. L. Manganelli, P. Pintus, F. Gambini, D. Fowler, M. Fournier, S. Faralli, C. Kopp, and C. J. Oton, “Large-fsr thermally tunable double-ring filters for wdm applications in silicon photonics,” *IEEE Photonics Journal*, vol. 9, no. 1, pp. 1–10, 2017.
- [42] S. J. Spector, M. E. Grein, R. T. Schulein, M. W. Geis, J. U. Yoon, D. M. Lennon, F. Gan, F. X. Kärtner, and T. M. Lyszczarz, “Compact carrier injection based mach-zehnder modulator in silicon,” in *Integrated Photonics and Nanophotonics Research and Applications / Slow and Fast Light*, Optical Society of America, 2007, ITuE5.
- [43] M. R. Watts, W. A. Zortman, D. C. Trotter, R. W. Young, and A. L. Lentine, “Low-voltage, compact, depletion-mode, silicon mach-zehnder modulator,” *IEEE Journal of Selected Topics in Quantum Electronics*, vol. 16, no. 1, pp. 159–164, 2010.
- [44] T. Tanabe, K. Nishiguchi, E. Kuramochi, and M. Notomi, “Low power and fast electro-optic silicon modulator with lateral p-i-n embedded photonic crystal nanocavity,” *Opt. Express*, vol. 17, no. 25, pp. 22 505–22 513, 2009.
- [45] A. Brimont, D. J. Thomson, P. Sanchis, J. Herrera, F. Gardes, J. M. Fedeli, G. T. Reed, and J. Martí, “High speed silicon electro-optical modulators enhanced via slow light propagation,” *Opt. Express*, vol. 19, no. 21, pp. 20 876–20 885, 2011.

- [46] D. Patel, A. Samani, V. Veerasubramanian, S. Ghosh, and D. V. Plant, "Silicon photonic segmented modulator-based electro-optic dac for 100 gb/s pam-4 generation," *IEEE Photonics Technology Letters*, vol. 27, no. 23, pp. 2433–2436, 2015.
- [47] G. Cocorullo, F. G. Della Corte, and I. Rendina, "Temperature dependence of the thermo-optic coefficient in crystalline silicon between room temperature and 550 k at the wavelength of 1523 nm," *Applied Physics Letters*, vol. 74, no. 22, pp. 3338–3340, 1999.
- [48] D. Wu, Y. Wu, Y. Wang, J. An, and X. Hu, "Reconfigurable optical add-drop multiplexer based on thermally tunable micro-ring resonators," *Optics Communications*, vol. 367, pp. 44–49, 2016, ISSN: 0030-4018. DOI: <https://doi.org/10.1016/j.optcom.2016.01.018>. [Online]. Available: <http://www.sciencedirect.com/science/article/pii/S0030401816300189>.
- [49] X. Wang, A. Lentine, C. DeRose, A. L. Starbuck, D. Trotter, A. Pomerene, and S. Mookherjea, "Wide-range and fast thermally-tunable silicon photonic microring resonators using the junction field effect," *Opt. Express*, vol. 24, no. 20, pp. 23 081–23 093, 2016.
- [50] S. N. Zheng, J. Zou, H. Cai, J. F. Song, L. K. Chin, P. Y. Liu, Z. P. Lin, D. L. Kwong, and A. Q. Liu, "Microring resonator-assisted fourier transform spectrometer with enhanced resolution and large bandwidth in single chip solution," *Nat. Commun.*, vol. 10, no. 2349, 2019.
- [51] H. Jayatilleka, H. Shoman, L. Chrostowski, and S. Shekhar, "Photoconductive heaters enable control of large-scale silicon photonic ring resonator circuits," *Optica*, vol. 6, no. 1, pp. 84–91, 2019.
- [52] G. T. Reed and C. J. Png], "Silicon optical modulators," *Materials Today*, vol. 8, no. 1, pp. 40–50, 2005.
- [53] R. Soref and B. Bennett, "Electrooptical effects in silicon," *IEEE Journal of Quantum Electronics*, vol. 23, no. 1, pp. 123–129, 1987.
- [54] G. T. Reed, G. Z. Mashanovich, F. Y. Gardes, M. Nedeljkovic, Y. Hu, D. J. Thomson, K. Li, P. R. Wilson, S.-W. Chen, and S. S. Hsu, "Recent breakthroughs in carrier depletion based silicon optical modulators," *Nanophotonics*, vol. 3, no. 4-5, pp. 229–245, 2014.
- [55] Y. Ren, Z. Jiang, and V. Van, "A fast silicon wavelength selector for optical transceiver," in *Asia Communications and Photonics Conference (ACPC) 2019*, Optical Society of America, 2019, T2D.5.
- [56] M. Soltani and R. Soref, "Free-carrier electrorefraction and electroabsorption in wurtzite gan," *Opt. Express*, vol. 23, no. 19, pp. 24 984–24 990, 2015.
- [57] B. Chmielak, M. Waldow, C. Matheisen, C. Ripperda, J. Bolten, T. Wahlbrink, M. Nagel, F. Merget, and H. Kurz, "Pockels effect based fully integrated, strained silicon electro-optic modulator," *Opt. Express*, vol. 19, no. 18, pp. 17 212–17 219, 2011.

- [58] T. Hu, W. Wang, C. Qiu, P. Yu, H. Qiu, Y. Zhao, X. Jiang, and J. Yang, “Thermally tunable filters based on third-order microring resonators for wdm applications,” *IEEE Photonics Technology Letters*, vol. 24, no. 6, pp. 524–526, 2012.
- [59] R. Amatya, C. W. Holzwarth, H. I. Smith, and R. J. Ram, “Precision tunable silicon compatible microring filters,” *IEEE Photonics Technology Letters*, vol. 20, no. 20, pp. 1739–1741, 2008, ISSN: 1941-0174.
- [60] F. Gan, T. Barwicz, M. A. Popovic, M. S. Dahlem, C. W. Holzwarth, P. T. Rakich, H. I. Smith, E. P. Ippen, and F. X. Kärtner, “Maximizing the thermo-optic tuning range of silicon photonic structures,” in *2007 Photonics in Switching*, 2007, pp. 67–68.
- [61] Y. Ren, D. Perron, F. Aurangozeb, Z. Jiang, M. Hossain, and V. Van, “A continuously tunable silicon double-microring filter with precise temperature tracking,” *IEEE Photonics Journal*, vol. 10, no. 6, pp. 1–10, 2018.
- [62] S. B. Villers, D. Hould, and W. Shi, “Ultra-compact dwdm filter tunable across the c-band,” in *2019 Optical Fiber Communications Conference and Exhibition (OFC)*, 2019, pp. 1–3.
- [63] H. Jayatilleka, R. Boeck, K. Murray, J. Flueckiger, L. Chrostowski, N. A. F. Jaeger, and S. Shekhar, “Automatic wavelength tuning of series-coupled vernier racetrack resonators on soi,” in *2016 Optical Fiber Communications Conference and Exhibition (OFC)*, 2016, pp. 1–3.
- [64] H. Jayatilleka, R. Boeck, M. AlTaha, J. Flueckiger, N. A. F. Jaeger, S. Shekhar, and L. Chrostowski, “Automatic tuning and temperature stabilization of high-order silicon vernier microring filters,” in *2017 Optical Fiber Communications Conference and Exhibition (OFC)*, 2017, pp. 1–3.
- [65] J. C. C. Mak, W. D. Sacher, T. Xue, J. C. Mikkelsen, Z. Yong, and J. K. S. Poon, “Automatic resonance alignment of high-order microring filters,” *IEEE Journal of Quantum Electronics*, vol. 51, no. 11, pp. 1–11, 2015.
- [66] R. Gatdula, K. Kim, A. Melikyan, Y.-K. Chen, and P. Dong, “Simultaneous four-channel thermal adaptation of polarization insensitive silicon photonics wdm receiver,” *Opt. Express*, vol. 25, no. 22, pp. 27 119–27 126, 2017.
- [67] P. Dong, R. Gatdula, K. Kim, J. H. Sinsky, A. Melikyan, Y.-K. Chen, G. de Valicourt, and J. Lee, “Simultaneous wavelength locking of microring modulator array with a single monitoring signal,” *Opt. Express*, vol. 25, no. 14, pp. 16 040–16 046, 2017.
- [68] A. N. Inc., *Nanosoi fabrication process*, 2020. [Online]. Available: <https://www.appliednt.com/nanosoi/>.
- [69] M. S. Dahlem, C. W. Holzwarth, A. Khilo, F. X. Kärtner, H. I. Smith, and E. P. Ippen, “Reconfigurable multi-channel second-order silicon microring-resonator filterbanks for on-chip wdm systems,” in *2010 Photonics Global Conference*, 2010, pp. 1–3.

- [70] L. Santec Company, *Santec company, ltd.* 2020. [Online]. Available: <http://www.santec.com/jp/wp-content/uploads/WSS-1000-C-E-v1.01402.pdf/>.
- [71] S. Han, T. J. Seok, K. Yu, N. Quack, R. S. Muller, and M. C. Wu, “Large-scale polarization-insensitive silicon photonic mems switches,” *Journal of Lightwave Technology*, vol. 36, no. 10, pp. 1824–1830, 2018.
- [72] C. Kachris and I. Tomkos, “A survey on optical interconnects for data centers,” *IEEE Communications Surveys Tutorials*, vol. 14, no. 4, pp. 1021–1036, 2012.
- [73] Y. Li, H. Liu, W. Yang, D. Hu, and W. Xu, “Inter-data-center network traffic prediction with elephant flows,” in *NOMS 2016 - 2016 IEEE/IFIP Network Operations and Management Symposium*, 2016, pp. 206–213.
- [74] Z. Cao, M. Kodialam, and T. V. Lakshman, “Joint static and dynamic traffic scheduling in data center networks,” *IEEE/ACM Transactions on Networking*, vol. 24, no. 3, pp. 1908–1918, 2016.
- [75] S. T. Girisankar, T. Truong-Huu, and M. Gurusamy, “Sdn-based dynamic flow scheduling in optical data centers,” in *2017 9th International Conference on Communication Systems and Networks (COMSNETS)*, 2017, pp. 190–197.
- [76] Z. Guo and Y. Yang, “Low-latency multicast scheduling in all-optical interconnects,” *IEEE Transactions on Communications*, vol. 62, no. 4, pp. 1310–1323, 2014.
- [77] C. Kachris, K. Kanonakis, and I. Tomkos, “Optical interconnection networks in data centers: Recent trends and future challenges,” *IEEE Communications Magazine*, vol. 51, no. 9, pp. 39–45, 2013.
- [78] K. Shi, S. Lange, I. Haller, D. Cletheroe, R. Behrendt, B. Thomsen, F. Karinou, K. Jozwik, P. Costa, and H. Ballani, “System demonstration of nanosecond wavelength switching with burst-mode pam4 transceiver,” in *The 45th European Conference on Optical Communication (ECOC Post-deadline Paper)*, 2019.
- [79] T. Aalto, M. Harjanne, M. Kapulainen, S. Ylinen, and L. Mörl, “Fast 100-channel wavelength selectors integrated on silicon,” in *Silicon Photonics VI*, J. A. Kubby and G. T. Reed, Eds., International Society for Optics and Photonics, vol. 7943, SPIE, pp. 216–224.
- [80] T. Matsumoto, T. Kurahashi, R. Konoike, K. Tanizawa, K. Suzuki, A. Uetake, K. Takabayashi, K. Ikeda, H. Kawashima, S. Akiyama, and S. Sekiguchi, “In-line optical amplification for silicon photonics platform by flip-chip bonded inpsas,” in *Optical Fiber Communication Conference*, Optical Society of America, 2018, Tu2A.4.
- [81] L. Lu, L. Zhou, X. Li, and J. Chen, “Silicon photonic vernier cascaded microring filter for broadband tunability,” *Opt. Lett.*, vol. 39, no. 6, pp. 1633–1636, 2014.

- [82] Y. Ren, F. Aurangozeb, D. Perron, Z. Jiang, M. Hossain, and V. Van, “Silicon photonic vernier cascaded microring filter for broadband tunability,” *IEEE Photonics Technology Letters*, vol. 31, no. 18, pp. 1503–1506, 2019.
- [83] W. M. J. Green, M. J. Rooks, L. Sekaric, and Y. A. Vlasov, “Ultra-compact, low rf power, 10 gb/s silicon mach-zehnder modulator,” *Opt. Express*, vol. 15, no. 25, pp. 17 106–17 113, 2007.
- [84] L. Yang, H. Chen, and J. Ding, “12.5 gb/s carrier-injection silicon mach-zehnder optical modulator with high optical bandwidth,” in *The 9th International Conference on Group IV Photonics (GFP)*, 2012, pp. 129–131.
- [85] G. T. Reed, D. J. Thomson, F. Y. Gardes, Y. Hu, J.-M. Fedeli, and G. Z. Mashanovich, “High-speed carrier-depletion silicon mach-zehnder optical modulators with lateral pn junctions,” *Frontiers in Physics*, vol. 2, p. 77, 2014.
- [86] H. Sepehrian, J. Lin, L. A. Rusch, and W. Shi, “Silicon photonic iq modulators for 400 gb/s and beyond,” *Journal of Lightwave Technology*, vol. 37, no. 13, pp. 3078–3086, 2019.
- [87] L. Advanced Micro Foundry Company, *Advanced micro foundry company, ltd.* 2020. [Online]. Available: <http://www.advmf.com/>.
- [88] Y. Ren, D. Perron, F. Aurangozeb, Z. Jiang, M. Hossain, and V. Van, “A continuously tunable soi microring filter with temperature tracking,” in *2018 IEEE Photonics Conference (IPC)*, 2018, pp. 1–2.
- [89] Y. Ren, D. Perron, F. Aurangozeb, Z. Jiang, M. Hossain, and V. Van, “A continuously tunable silicon double-microring filter with precise temperature tracking,” *IEEE Photonics Journal*, vol. 10, no. 6, pp. 1–10, 2018.
- [90] Y. Ren, D. Perron, F. Aurangozeb, Z. Jiang, M. Hossain, and V. Van, “Broadband-tunable cascaded vernier silicon photonic microring filter with temperature tracking,” in *2019 Optical Fiber Communications Conference and Exhibition (OFC)*, 2019, pp. 1–3.
- [91] M. Fiorani, S. Aleksic, M. Casoni, L. Wosinska, and J. Chen, “Energy-efficient elastic optical interconnect architecture for data centers,” *IEEE Communications Letters*, vol. 18, no. 9, pp. 1531–1534, 2014.
- [92] H. Bai and Y. Wang, “Tunable wavelength converters based switching structure for wdm-tdm hybrid pon,” *Optik - International Journal for Light and Electron Optics*, vol. 124, no. 22, pp. 5388–5390, 2013, ISSN: 0030-4026. DOI: 10.1016/j.ijleo.2013.03.130.
- [93] A. S. Thyagaturu, A. Mercian, M. P. McGarry, M. Reisslein, and W. Kellerer, “Software defined optical networks (sdons): A comprehensive survey,” *IEEE Communications Surveys Tutorials*, vol. 18, no. 4, pp. 2738–2786, 2016.
- [94] B. C. Chatterjee, N. Sarma, and E. Oki, “Routing and spectrum allocation in elastic optical networks: A tutorial,” *IEEE Communications Surveys Tutorials*, vol. 17, no. 3, pp. 1776–1800, 2015.

- [95] Y. Ding, M. Pu, L. Liu, J. Xu, C. Peucheret, X. Zhang, D. Huang, and H. Ou, “Bandwidth and wavelength-tunable optical bandpass filter based on silicon microring-mzi structure,” *Opt. Express*, vol. 19, no. 7, pp. 6462–6470, 2011.
- [96] T. Dai, A. Shen, G. Wang, Y. Wang, Y. Li, X. Jiang, and J. Yang, “Bandwidth and wavelength tunable optical passband filter based on silicon multiple microring resonators,” *Opt. Lett.*, vol. 41, no. 20, pp. 4807–4810, 2016.
- [97] L. Chen, N. Sherwood-Droz, and M. Lipson, “Compact bandwidth-tunable microring resonators,” *Opt. Lett.*, vol. 32, no. 22, pp. 3361–3363, 2007.
- [98] G. Pouloupoulos, G. Kanakis, P. Toumasis, G. Giannoulis, D. Kalavrouziotis, D. Apostolopoulos, and H. Avramopoulos, “Air trenches-assisted highly selective, fully flexible soi filtering element,” in *Optical Fiber Communication Conference (OFC) 2019*, Optical Society of America, 2019, W2A.6.
- [99] P. Alipour, A. A. Eftekhar, A. H. Atabaki, Q. Li, S. Yegnanarayanan, C. K. Madsen, and A. Adibi, “Fully reconfigurable compact rf photonic filters using high-q silicon microdisk resonators,” in *2010 23rd Annual Meeting of the IEEE Photonics Society*, 2010, pp. 236–237.
- [100] L. Zhuang, W. Beeker, A. Leinse, R. Heideman, P. van Dijk, and C. Roeloffzen, “Novel wideband microwave polarization network using a fully-reconfigurable photonic waveguide interleaver with a two-ring resonator-assisted asymmetric mach-zehnder structure,” *Opt. Express*, vol. 21, no. 3, pp. 3114–3124, 2013.
- [101] J. S. Fandiño, P. Muñoz, D. Doménech, and J. Capmany, “A monolithic integrated photonic microwave filter,” *Nature Photon*, vol. 11, no. 3, pp. 124–129, 2017.
- [102] K. Jinguji, “Synthesis of coherent two-port optical delay-line circuit with ring waveguides,” *Journal of Lightwave Technology*, vol. 14, no. 8, pp. 1882–1898, 1996.
- [103] Y. Zhang, Y. He, J. Wu, X. Jiang, R. Liu, C. Qiu, X. Jiang, J. Yang, C. Tremblay, and Y. Su, “High-extinction-ratio silicon polarization beam splitter with tolerance to waveguide width and coupling length variations,” *Opt. Express*, vol. 24, no. 6, pp. 6586–6593, 2016.
- [104] S. Nakamura, S. Takahashi, M. Sakauchi, T. Hino, Ming-Bin Yu, and Guo-Qiang Lo, “Wavelength selective switching with one-chip silicon photonic circuit including 8×8 matrix switch,” in *2011 Optical Fiber Communication Conference and Exposition and the National Fiber Optic Engineers Conference*, 2011, pp. 1–3.
- [105] Z. Guo, L. Lu, L. Zhou, L. Shen, and J. Chen, “ 16×16 silicon optical switch based on dual-ring-assisted mach-zehnder interferometers,” *Journal of Lightwave Technology*, vol. 36, no. 2, pp. 225–232, 2018.
- [106] Z. Dong, F. N. Khan, Q. Sui, K. Zhong, C. Lu, and A. P. T. Lau, “Optical performance monitoring: A review of current and future technologies,” *Journal of Lightwave Technology*, vol. 34, no. 2, pp. 525–543, 2016.

- [107] L. Vivien, A. Polzer, D. Marris-Morini, J. Osmond, J. M. Hartmann, P. Crozat, E. Cassan, C. Kopp, H. Zimmermann, and J. M. Fédéli, “Zero-bias 40gbit/s germanium waveguide photodetector on silicon,” *Opt. Express*, vol. 20, no. 2, pp. 1096–1101, 2012.
- [108] A. K. Sood, J. W. Zeller, R. A. Richwine, Y. R. Puri, H. Efstathiadis, P. Haldar, N. K. Dhar, and D. L. Polla, *SiGe based visible-NIR photodetector technology for optoelectronic applications*. 2015.
- [109] Y. Wan, Z. Zhang, R. Chao, J. Norman, D. Jung, C. Shang, Q. Li, M. Kennedy, D. Liang, C. Zhang, *et al.*, “Monolithically integrated inas/ingaas quantum dot photodetectors on silicon substrates,” *Optics express*, vol. 25, no. 22, pp. 27 715–27 723, 2017.
- [110] L. Menon, H. Yang, S. J. Cho, S. Mikael, Z. Ma, C. Reuterskiold-Hedlund, M. Hammar, and W. Zhou, “Heterogeneously integrated ingaas and si membrane four-color photodetector arrays,” *IEEE Photonics Journal*, vol. 8, no. 2, pp. 1–7, 2016.
- [111] Y. Ma, Y. Zhang, Y. Gu, Y. Shi, X. Chen, W. Ji, B. Du, X. Shao, and J. Fang, “Electron-initiated low noise 1064 nm ingaasp/inalas avalanche photodetectors,” *Optics express*, vol. 26, no. 2, pp. 1028–1037, 2018.
- [112] S. Xi, Y. Gu, Y. Zhang, X. Chen, Y. Ma, L. Zhou, B. Du, X. Shao, and J. Fang, “Ingaasp/inp photodetectors targeting on 1.06 μm wavelength detection,” *Infrared Physics & Technology*, vol. 75, pp. 65–69, 2016.
- [113] T. K. Liang, H. K. Tsang, I. E. Day, J. Drake, A. P. Knights, and M. Asghari, “Silicon waveguide two-photon absorption detector at 1.5 μm wavelength for autocorrelation measurements,” *Applied Physics Letters*, vol. 81, no. 7, pp. 1323–1325, 2002.
- [114] H. Chen and A. W. Poon, “Two-photon absorption photocurrent in p-i-n diode embedded silicon microdisk resonators,” *Applied Physics Letters*, vol. 96, no. 19, p. 191 106, 2010.
- [115] H. Chen, X. Luo, and A. W. Poon, “Cavity-enhanced photocurrent generation by 1.55 μm wavelengths linear absorption in a p-i-n diode embedded silicon microring resonator,” *Applied Physics Letters*, vol. 95, no. 17, p. 171 111, 2009.
- [116] D. Feng, S. Liao, P. Dong, N.-N. Feng, H. Liang, D. Zheng, C.-C. Kung, J. Fong, R. Shafiha, J. Cunningham, A. V. Krishnamoorthy, and M. Asghari, “High-speed ge photodetector monolithically integrated with large cross-section silicon-on-insulator waveguide,” *Applied Physics Letters*, vol. 95, no. 26, p. 261 105, 2009.
- [117] H. M. Gibbs, “Chapter 2 - steady-state model of optical bistability,” in *Optical Bistability: Controlling Light with Light*, H. M. Gibbs, Ed., Academic Press, 1985, pp. 19–92.

- [118] Q. Lin, O. J. Painter, and G. P. Agrawal, “Nonlinear optical phenomena in silicon waveguides: Modeling and applications,” *Opt. Express*, vol. 15, no. 25, pp. 16 604–16 644, 2007.
- [119] A. D. Bristow, N. Rotenberg, and H. M. van Driel, “Two-photon absorption and kerr coefficients of silicon for 850–2200nm,” *Applied Physics Letters*, vol. 90, no. 19, p. 191 104, 2007.
- [120] H. Zhu, L. Zhou, R. Yang, X. Li, and J. Chen, “Enhanced near-infrared photodetection with avalanche gain in silicon microdisk resonators integrated with pn diodes,” *Optics letters*, vol. 39, no. 15, pp. 4525–4528, 2014.
- [121] B. Desiatov, I. Goykhman, J. Shappir, and U. Levy, “Defect-assisted sub-bandgap avalanche photodetection in interleaved carrier-depletion silicon waveguide for telecom band,” *Applied Physics Letters*, vol. 104, no. 9, p. 091 105, 2014.
- [122] Y. Li, S. Feng, Y. Zhang, and A. W. Poon, “Sub-bandgap linear-absorption-based photodetectors in avalanche mode in pn-diode-integrated silicon microring resonators,” *Optics letters*, vol. 38, no. 23, pp. 5200–5203, 2013.
- [123] J. Kou, K. Tian, C. Chu, Y. Zhang, X. Zhou, Z. Feng, and Z.-H. Zhang, “Optimization strategy of 4h-sic separated absorption charge and multiplication avalanche photodiode structure for high ultraviolet detection efficiency,” *Nanoscale Research Letters*, vol. 14, no. 1, p. 396, 2019.
- [124] S. Miller, “Avalanche breakdown in germanium,” *Physical review*, vol. 99, no. 4, p. 1234, 1955.
- [125] L. Zhang, Y. Fei, Y. Cao, X. Lei, and S. Chen, “Experimental observations of thermo-optical bistability and self-pulsation in silicon microring resonators,” *J. Opt. Soc. Am. B*, vol. 31, no. 2, pp. 201–206, 2014.
- [126] Q. Xu and M. Lipson, “Carrier-induced optical bistability in silicon ring resonators,” *Optics letters*, vol. 31, no. 3, pp. 341–343, 2006.
- [127] S. Chiangga, S. Pitakwongsaporn, T. D. Frank, and P. P. Yupapin, “Optical bistability investigation in a nonlinear silicon microring circuit,” *Journal of Lightwave Technology*, vol. 31, no. 7, pp. 1101–1105, 2013.
- [128] Z. Lu, D. Celo, H. Mehrvar, E. Bernier, and L. Chrostowski, “High-performance silicon photonic tri-state switch based on balanced nested mach-zehnder interferometer,” *Scientific Reports*, vol. 7, 2017, ISSN: 2045-2322.
- [129] Y. Ding, J. Xu, F. D. Ros, B. Huang, H. Ou, and C. Peucheret, “On-chip two-mode division multiplexing using tapered directional coupler-based mode multiplexer and demultiplexer,” *Opt. Express*, vol. 21, no. 8, pp. 10 376–10 382, 2013.
- [130] J. B. Driscoll, C. P. Chen, R. R. Grote, B. Souhan, J. I. Dadap, A. Stein, M. Lu, K. Bergman, and R. M. Osgood, “A 60 gb/s mdm-wdm si photonic link with $\lt; 0.7$ db power penalty per channel,” *Opt. Express*, vol. 22, no. 15, pp. 18 543–18 555, 2014.

- [131] B. A. Dorin and W. N. Ye, “Two-mode division multiplexing in a silicon-on-insulator ring resonator,” *Opt. Express*, vol. 22, no. 4, pp. 4547–4558, 2014.
- [132] D. Dai, J. Wang, S. Chen, S. Wang, and S. He, “Monolithically integrated 64-channel silicon hybrid demultiplexer enabling simultaneous wavelength- and mode-division-multiplexing,” *Laser & Photonics Review*, vol. 9, no. 3, 339–344, 2015.

Appendix A: Appendix

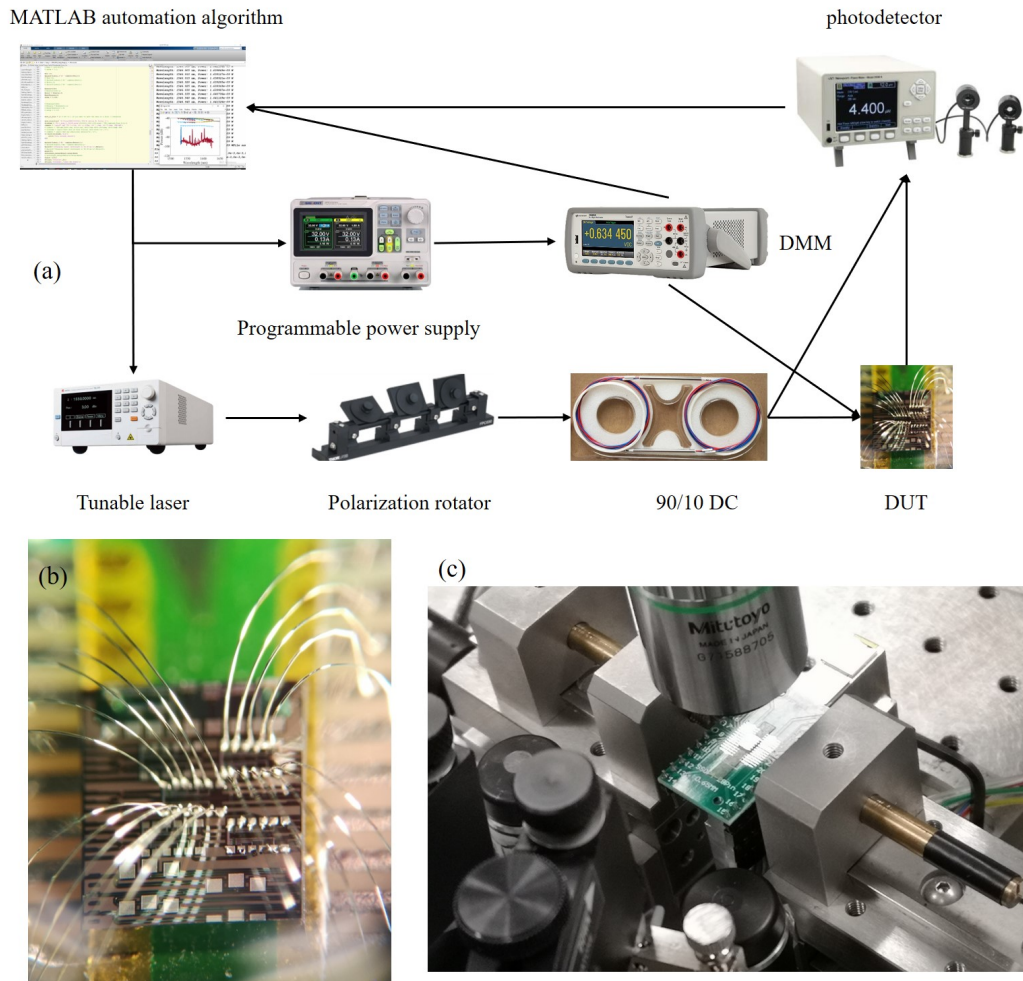


Figure A.1: (a) Schematic diagram of the filter optimization and tuning measurement setup. (b) The close look of the wire-bonded chip. (c) The image of the settled chip and lensed fibers.

The general filter optimization and tuning measurement set up is shown in Fig. A.1(a). The direction of arrows represents the direction of the output of the devices. The MATLAB algorithm is developed to automate the optimization and tuning process. A 90/10 power splitting direction coupler is deployed to monitor the optical power stability. In order to build the measurement setup that is scalable for multi-channel chip performance assessment, we wire-bonded the device as shown in Fig.

A.1(b). To couple the light onto the chip, lensed fibers are placed on two sides of the wire-bonded chip. Each fiber is clipped by a 3-axis controller for fiber-chip alignment. The snap of the lensed fibers and chip is shown in Fig. A.1(c).

In order to make the measurement setup scalable for multi-channel and chip-level performance testing, we developed the 8-channel programmable power supply based on Arduino Due board which are all accessible from MATLAB algorithm. The Arduino based microcontroller unit is shown in Fig.A.2. The Arduino board is connected to a PC running MATLAB script, which establishes a serial connection to the board. The PC sends the 12-bit input and clock sequence from the Arduino to a 1-to-8 I2C MUX. The TCA9548A 1-to-8 I2C MUX is used to expand the control output from single to 8. In every clock cycle, the MUX will update the value to each digital-analog converter (DAC) on sequence. The DAC, which has a 12-bit resolution, will output a voltage at the pin with a resolution of $5.5\text{V}/4096 = 1.3\text{ mV}$ for the 5.5V external voltage supply, which is enough for the filter spectral optimization within $\pm 10\text{ pm}$. The 12-bit input is received via an I2C connection from the Arduino microcontroller. This

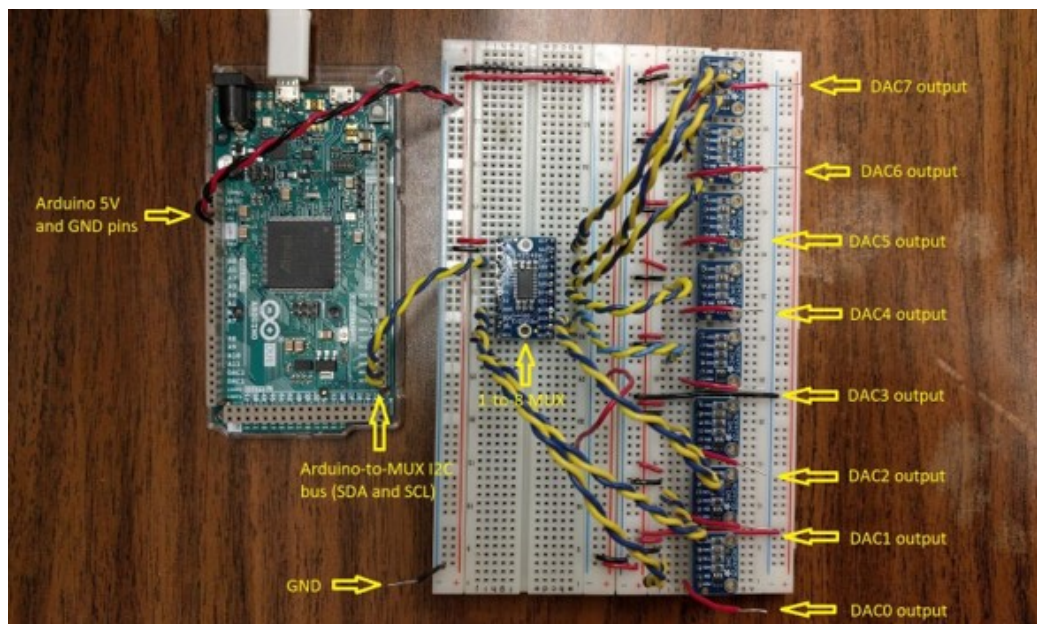


Figure A.2: A Arduino based current control until for optimization and tuning in filters and wavelength selectors.

design offers excellent potential for scalability to accommodate an arbitrarily large number of heaters. We can select between two different addresses for each MCP4725 using the A0 pin. This means that two DACs can be connected to one I2C bus on the MUX, for a total of 16 DACs per I2C bus on the Arduino board; in particular, the Arduino Due has two I2C buses, and could therefore support as many as 32 heaters.

Below in Fig. A.3 - A.7, we demonstrate the thermal tuning process in details. For a 4th order CMR filter, we sweep the heater's current from within a specific range. The algorithm will record the current value and apply the optimized current to the heater after the sweep is finished. Then we repeat the process for the rest of the heaters. Again, each heater's current will be recorded and set before the algorithm move to the next heater.

Fig. A.7 shows the summary of the optical power at the drop port of the filter after each optimization iteration. The total time is recorded as 296 seconds for a 4th-order CMR filter with a 5-iteration spectral optimization algorithm.

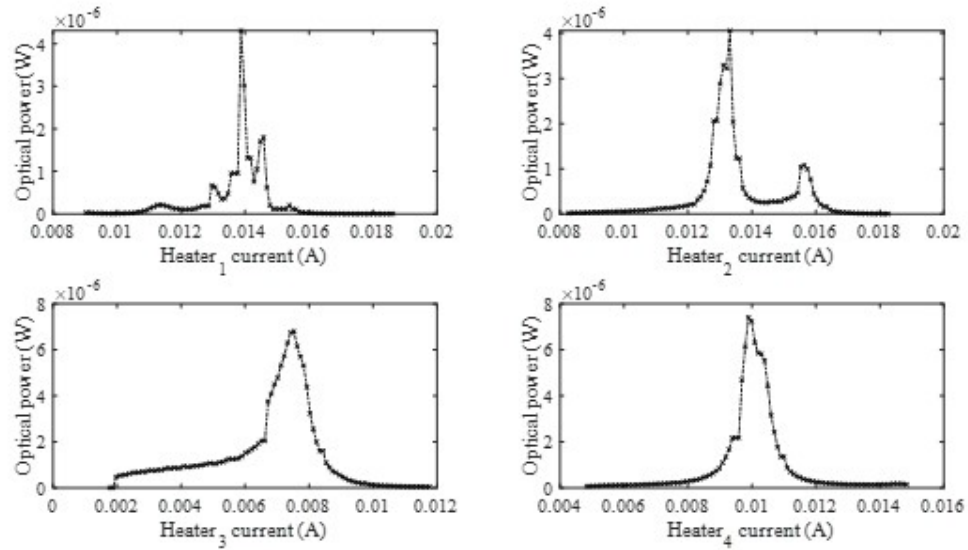


Figure A.3: The current sweep of each heater in the spectral optimization process to search the peak optical power output, in optimization iteration #1.

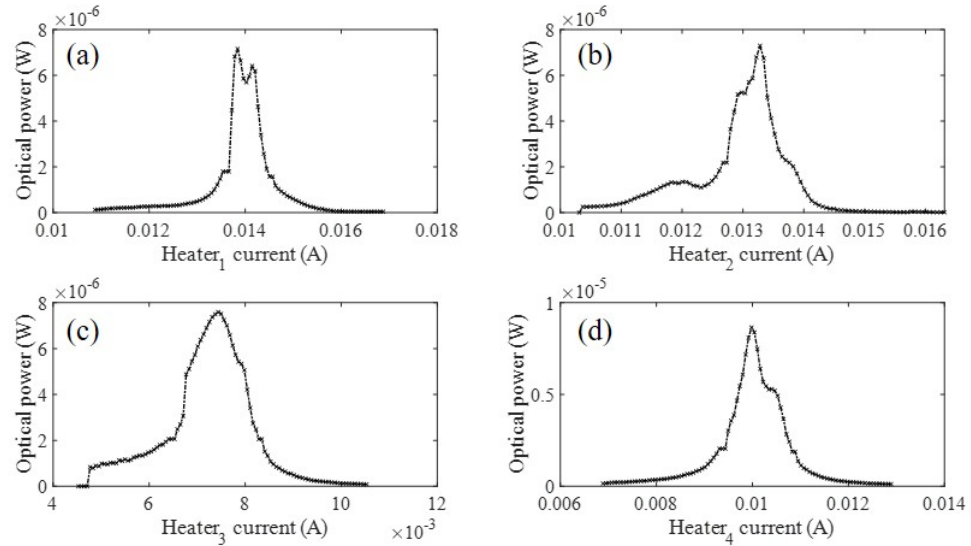


Figure A.4: The current sweep of each heater in the spectral optimization process to search the peak optical power output, in optimization iteration #2.

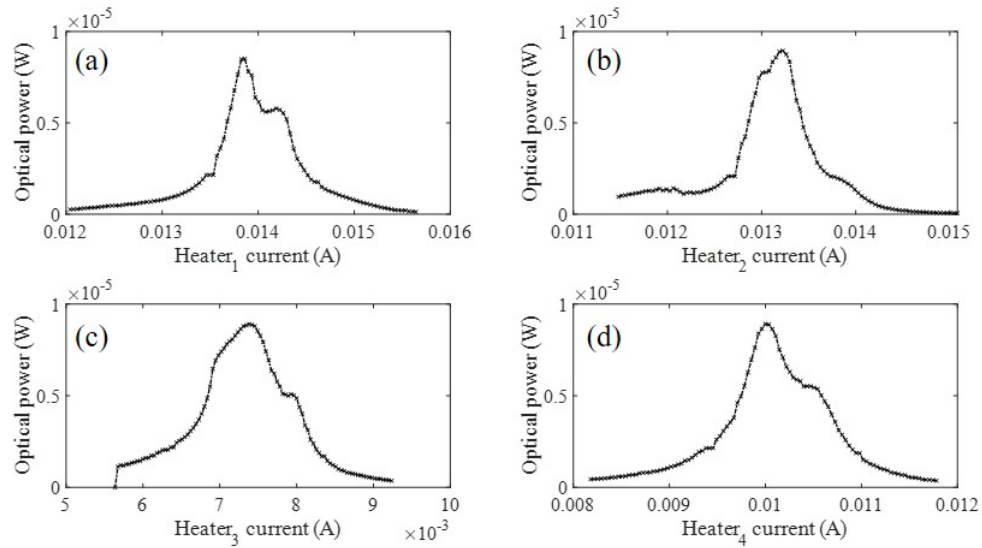


Figure A.5: The current sweep of each heater in the spectral optimization process to search the peak optical power output, in optimization iteration #3.

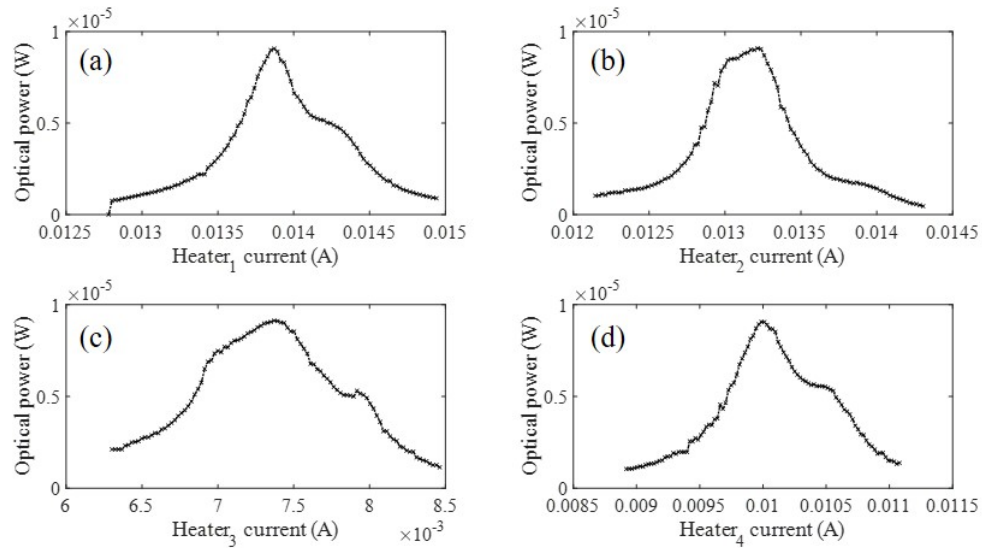


Figure A.6: The current sweep of each heater in the spectral optimization process to search the peak optical power output, in optimization iteration #4.

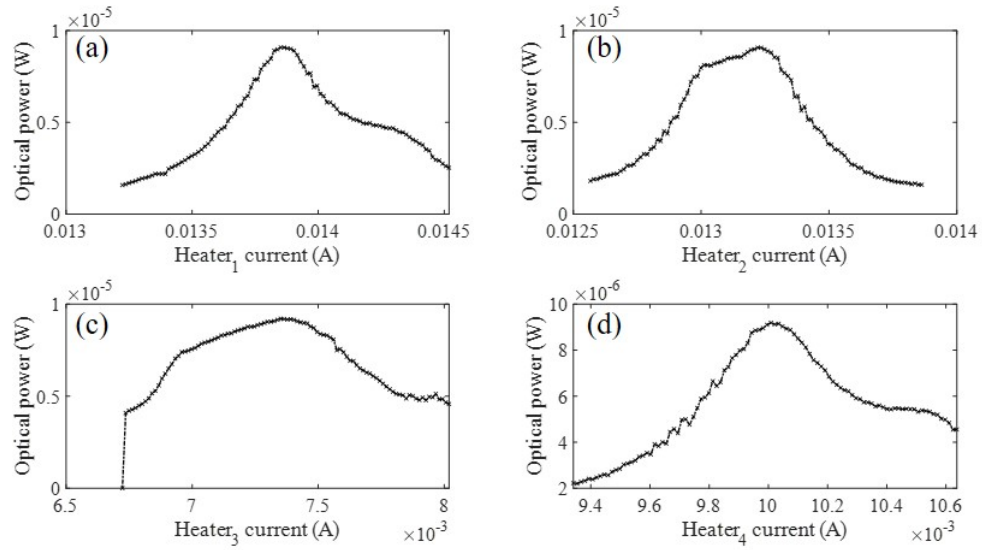


Figure A.7: The current sweep of each heater in the spectral optimization process to search the peak optical power output, in optimization iteration #5.

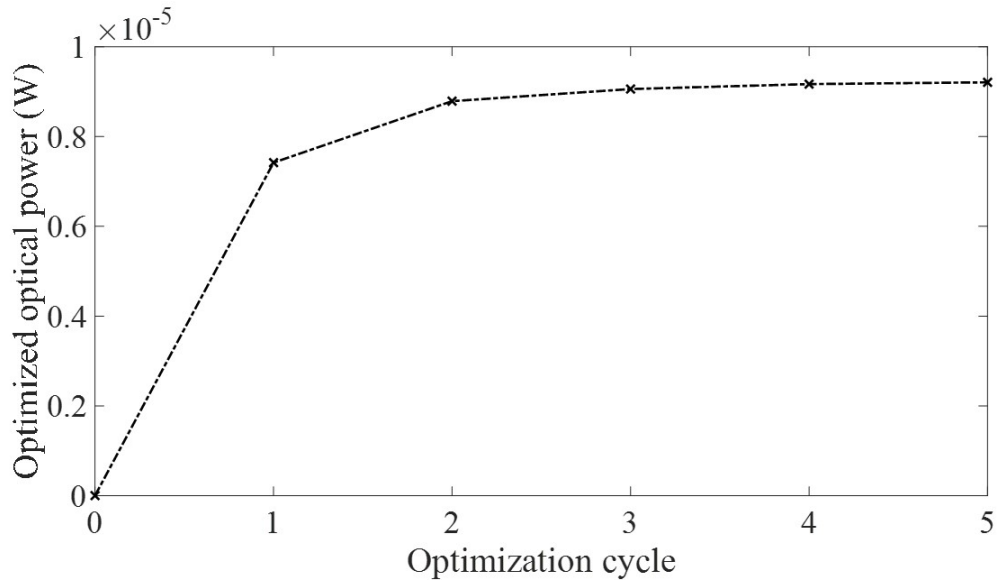


Figure A.8: The summary of a 5-iteration optimization. The optical power at output port gradually increases and gets to the peak at the 5th iteration.